arXiv:hep-ph/0008127v1 14 Aug 2000

# Higgs Particles in the Standard Model and Supersymmetric Theories

Dissertation

zur Erlangung des Doktorgrades

des Fachbereichs Physik

der Universität Hamburg

vorgelegt von

Milada Margarete Mühlleitner

aus Aalen

Hamburg

2000

Gutachter der Dissertation: Prof. Dr. P.M. Zerwas
Prof. Dr. B.A. Kniehl

Gutachter der Disputation: Prof. Dr. P.M. Zerwas
Prof. Dr. J. Bartels

Datum der Disputation: 13. Juli 2000

Dekan des Fachbereichs Physik
und Vorsitzender des
Promotionsausschusses: Prof. Dr. F.–W. Büßer

Für meinen Vater

# ABSTRACT

This thesis presents a theoretical analysis of the properties of the Higgs bosons in the Standard Model (SM) and the minimal supersymmetric extension (MSSM), which can be investigated at the LHC and $e^+e^-$ linear colliders. The final goal is the reconstruction of the Higgs potential and thus the verification of the Higgs mechanism. MSSM Higgs boson production processes at future $\gamma\gamma$ colliders are calculated in several decay channels. Heavy scalar and pseudoscalar Higgs bosons can be discovered in the $b\bar{b}$ final state in the investigated mass range 200 to 800 GeV for moderate and large values of $\tan\beta$. The $\tau^+\tau^-$ channel provides a heavy Higgs boson discovery potential for large values of $\tan\beta$. Several mechanisms that can be exploited at $e^+e^-$ linear colliders for the measurement of the lifetime of a SM Higgs boson in the intermediate mass range are analysed. In the $WW$ mode, the lifetime of Higgs scalars with masses below $\sim 160$ GeV can be determined with an error less than 10%. The reconstruction of the Higgs potential requires the measurement of the Higgs self-couplings. The SM and MSSM trilinear Higgs self-couplings are accessible in double and triple Higgs production. A theoretical analysis is presented in the relevant channels at the LHC and $e^+e^-$ linear colliders. For high luminosities, the SM trilinear Higgs self-coupling can be measured with an accuracy of 20% at a 500 GeV $e^+e^-$ linear collider. The MSSM coupling among three light Higgs bosons has to be extracted from continuum production. The other trilinear Higgs couplings are measurable in a restricted range of the MSSM parameter space. At the LHC, the $Hhh$ coupling can be probed in resonant decays.

# ZUSAMMENFASSUNG

Diese Doktorarbeit präsentiert eine theoretische Analyse der Eigenschaften von Higgsteilchen im Standard Modell (SM) und der minimalen supersymmetrischen Erweiterung (MSSM), die am LHC und $e^+e^-$ Linearcollidern untersucht werden können. Das Ziel ist, das Higgspotential zu rekonstruieren und dadurch den Higgsmechanismus zu überprüfen. Für die MSSM Higgs-Boson Produktion an zukünftigen $\gamma\gamma$-Beschleunigern werden Prozesse in verschiedenen Zerfallskanälen berechnet. Schwere skalare und pseudoskalare Higgs-Bosonen können im $b\bar{b}$ Endzustand im gesamten untersuchten Massenbereich von 200 bis 800 GeV für mittlere und große Werte von $\tan\beta$ entdeckt werden. Der $\tau^+\tau^-$ Kanal erlaubt die Entdeckung von schweren Higgs-Bosonen für große Werte von $\tan\beta$. Es werden mehrere Mechanismen untersucht, die an $e^+e^-$ Linearbeschleunigern für die Lebensdauerbestimmung eines Higgs-Bosons im intermediären Massenbereich verwendet werden können. Im $WW$-Kanal kann die Lebensdauer von Higgs-Skalaren, die leichter als $\sim 160$ GeV sind, mit einem Fehler von weniger als 10% bestimmt werden. Die Rekonstruktion des Higgspotentials erfordert die Messung der Higgs-Selbstkopplungen. Die trilinearen Higgs-Kopplungen des SM und des MSSM sind in der Produktion von zwei und drei Higgsteilchen zugänglich. Es wird eine theoretische Analyse in den am LHC und an $e^+e^-$ Linearbeschleunigern relevanten Kanälen durchgeführt. Bei hohen Luminositäten kann die trilineare Higgs-Selbstkopplung des SM mit einer Genauigkeit von 20% an einem 500 GeV $e^+e^-$ Linearbeschleuniger gemessen werden. Die MSSM Kopplung zwischen drei leichten Higgs-Bosonen muß in der Kontinuumsproduktion ermittelt werden. Die übrigen trilinearen Kopplungen sind in einem eingeschränkten Parameterbereich des MSSM-Parameterraumes meßbar. Am LHC kann die $Hhh$-Kopplung in resonanten Zerfällen untersucht werden.

# Contents

**1 Introduction** **1**

**2 The SM and the MSSM Higgs sector** **5**
- 2.1 The Higgs particle of the Standard Model . . . . . 5
- 2.2 Supersymmetry . . . . . 7
  - 2.2.1 The Minimal Supersymmetric Standard Model . . . . . 7
  - 2.2.2 The MSSM Higgs sector . . . . . 10
  - 2.2.3 The Higgs-Yukawa and the Higgs-gauge couplings . . . . . 13

**3 Higgs boson search** **17**
- 3.1 Higgs boson search at $pp$ colliders . . . . . 18
  - 3.1.1 Standard Model Higgs boson . . . . . 18
  - 3.1.2 Supersymmetric extension . . . . . 21
- 3.2 Higgs boson search at $e^+e^-$ colliders . . . . . 22
  - 3.2.1 Standard Model . . . . . 22
  - 3.2.2 SUSY Higgs particles . . . . . 24
- 3.3 Heavy MSSM Higgs production in $\gamma\gamma$ collisions . . . . . 25
  - 3.3.1 The quark final states . . . . . 28
  - 3.3.2 The $\tau^+\tau^-$ channel . . . . . 37
  - 3.3.3 Chargino and neutralino production . . . . . 37
  - 3.3.4 Results . . . . . 38
  - 3.3.5 Discovery reach . . . . . 44

**4 The Lifetime of Higgs particles** **45**
- 4.1 The SM Higgs boson decays . . . . . 45
- 4.2 Decay modes of the MSSM Higgs particles . . . . . 47
  - 4.2.1 The total decay widths and branching ratios of non-SUSY decays . . 47
  - 4.2.2 Decays into SUSY particles . . . . . 48
- 4.3 Determination of the lifetime of Higgs bosons . . . . . 50
  - 4.3.1 The total width of the SM Higgs boson . . . . . 50
  - 4.3.2 Total widths of the MSSM Higgs particles . . . . . 52

**5 SM and MSSM Higgs self-couplings** **55**
- 5.1 Higgs self-couplings at $e^+e^-$ linear colliders . . . . . 55
  - 5.1.1 SM double-Higgs production in $e^+e^-$ collisions . . . . . 61
  - 5.1.2 SM $WW$ double-Higgs fusion . . . . . 64
  - 5.1.3 Double and triple Higgs production in the MSSM . . . . . 67

5.1.4 MSSM double Higgs-strahlung . . . . . . . . . . . . . . . . . . . . . . 68
5.1.5 Triple Higgs production . . . . . . . . . . . . . . . . . . . . . . . . 69
5.1.6 MSSM $WW$ double Higgs fusion . . . . . . . . . . . . . . . . . . . 72
5.1.7 Sensitivity areas . . . . . . . . . . . . . . . . . . . . . . . . . . . . 74
5.2 Higgs pair production at the LHC . . . . . . . . . . . . . . . . . . . . . . 78
5.2.1 SM double Higgs production . . . . . . . . . . . . . . . . . . . . . . 78
5.2.2 Higgs pairs in the MSSM . . . . . . . . . . . . . . . . . . . . . . . . 80
5.2.3 Extraction of the signal . . . . . . . . . . . . . . . . . . . . . . . . 84

**6 Conclusions** **87**

**Appendix** **89**

**A Scalar integrals** **89**

**B Double Higgs-strahlung processes** **91**
B.1 $e^+e^- \to ZH_iH_j$ . . . . . . . . . . . . . . . . . . . . . . . . . . . . 91
B.2 $e^+e^- \to ZAA$ . . . . . . . . . . . . . . . . . . . . . . . . . . . . . 92

**C Triple Higgs boson production** **93**
C.1 $e^+e^- \to AH_iH_j$ . . . . . . . . . . . . . . . . . . . . . . . . . . . . 93

**D Heavy Higgs production in $W_LW_L$ fusion** **95**
D.1 $W_LW_L \to H_iH_j$ . . . . . . . . . . . . . . . . . . . . . . . . . . . . 95
D.2 $W_LW_L \to AA$ . . . . . . . . . . . . . . . . . . . . . . . . . . . . . 96
D.3 Asymptotic energies . . . . . . . . . . . . . . . . . . . . . . . . . . . . 97

**Bibliography** **99**

# Chapter 1

# Introduction

The Standard Model of particle physics (SM) combines the electroweak and strong interactions based on the local $SU(3) \times SU(2)_L \times U(1)_Y$ gauge group. The electroweak gauge fields $W^{\pm}$, $Z$ and the photon field $A$ correspond to the four generators of the non-abelian $SU(2)_L \times U(1)_Y$ gauge group whereas the eight generators of the colour group $SU(3)$ are associated with the equivalent number of gluons. The interaction between matter and gauge fields is incorporated in the theory by minimal substitution which replaces the partial derivatives in the Lagrangean with the covariant ones including the couplings related to the various gauge groups. At this stage matter and gauge fields are still massless in contradiction to the experimental observation. Introducing explicit mass terms, however, would violate the gauge invariance and lead to a non-renormalizable theory with an infinite number of parameters to be adjusted by the experiment. Another difficulty arises due to the violation of the unitarity bounds at high energies by the scattering amplitudes of the massive $W^{\pm}/Z$ bosons and fermions.

A way out is provided by introducing an additional weak isodoublet scalar field [1–4]. One of the four degrees of freedom corresponds to a physical particle, the so-called Higgs boson. The self-interaction of the scalar field leads to an infinite number of degenerate ground states with non-zero vacuum expectation value (VEV) $v = (\sqrt{2}G_F)^{-1/2} \approx 246$ GeV. By choosing one of them as physical ground state, the $SU(2)_L \times U(1)_Y$ symmetry is hidden with the $U(1)_{em}$ symmetry left over. The Higgs couplings to other particles are defined by the constraint set by unitarity. Through the interaction with the scalar field in the ground state, the electroweak gauge bosons and the fundamental matter particles acquire their masses. The non-vanishing field strength, essential for the non-zero particle masses, is induced by the typical minimax form of the Higgs potential. After the "spontaneous symmetry breaking" the three Goldstone bosons among the four degrees of freedom of the Higgs doublet are absorbed to provide the longitudinal modes for the massive $Z$ and $W^{\pm}$ gauge bosons. Since all the Higgs couplings are predetermined, the parameters describing the Higgs particle are entirely fixed by its mass. This is the only unknown parameter in the SM Higgs sector [3, 4].

The Standard Model is in very good agreement with electroweak precision tests at LEP, SLC, Tevatron and HERA. In some cases it has been tested to an accuracy better than 0.1%. Up to now, the only deviation from the Standard Model has been the experimental indication of massive neutrinos, which can be embedded in the SM by introducing a mass term for neutrinos in the Yukawa Lagrangean. This strongly limits possible forms of new physics. Models that preserve the SM structure (extended by the neutrino mass term) are to be favoured. In this respect a promising candidate for possible extensions is supersymmetry [3, 5, 6].

In view of the impressing success of the SM one may ask of course why to consider extensions to new physics. The reason is that the SM implies many unanswered questions. The extrapolation of the model to high energies indicates a unification of all three gauge couplings at mass scales of the order of $M_{GUT} \sim 10^{14} - 10^{16}$ GeV [7] (Grand Unified Theories GUT's). If one assumes new physics to set in at the GUT scale, the SM will be valid in a mass range between the relative small weak scale of the order of $(\sqrt{2}G_F)^{-1/2} \approx 246$ GeV set by the Higgs mechanism and $M_{GUT}$ given by the grand unification scale. Quantum fluctuations, however, lead to large corrections of the Higgs mass at high scales. In order to keep the Higgs mass stable in the presence of the large GUT scale, the considerable corrections have to be absorbed in the mass counterterms leading to a finetuning of the Higgs parameters.

A stabilization of the separation between the electroweak and the GUT scale is provided by the introduction of supersymmetry (SUSY) which incorporates the most general symmetry of the $S$-matrix. Within the framework of supersymmetry the masses of the scalar particles remain moderate even in the presence of high energy scales. This is due to supersymmetry representing a connection between fermionic and bosonic degrees of freedom so that quantum corrections arising from the two particle types cancel each other. Even in softly broken supersymmetry the leading quadratic singularities vanish and are replaced by logarithmic divergences. Furthermore, SUSY GUT's lead to a prediction of the electroweak mixing angle [8] that is in very good agreement with present high-precision measurements of $\sin^2\theta_W$. A minimal realization of supersymmetry is given by the Minimal Supersymmetric extension of the Standard Model, the MSSM [3, 5, 6].

The Higgs mechanism described above is a basic ingredient of the electroweak sector both of the Standard Model and the MSSM. So far, however, it has not been verified experimentally. In order to establish this most important aspect for the consistent formulation of an electroweak theory experimentally, three steps have to be performed.

1. First of all the Higgs particle(s) must be discovered.
2. In a second step, the Higgs couplings to the fermions and gauge particles have to be determined via the partial decay widths and the Higgs production cross sections.
3. In order to finally reconstruct the Higgs potential, the trilinear and quadrilinear Higgs self-couplings have to be measured.

The discovery of a scalar particle alone will not reveal the mechanism by which the fundamental particle masses are generated. Only the knowledge of the Higgs self-interaction will allow for the determination of the explicit form of the Higgs potential.

In this work the procedure for the experimental verification of the Higgs sector will be analysed. For this task the picture of the Higgs particle will be evolved in the three steps described in the previous paragraph. For reasons resumed above not only the SM but also a supersymmetric extension, the MSSM which involves five physical Higgs particles [3, 5, 6], will be considered. The theoretical foundations will be developed and the experimental implications at the Large Hadron Collider [9], which is constructed for a c.m. energy of 14 TeV, and at high energy $e^+e^-$ linear colliders [10] will be discussed. The total integrated luminosity for the LHC is $\int \mathcal{L} = 100$ fb$^{-1}$ after 3 years. $e^+e^-$ linear colliders are planned to run in the energy range between 500 GeV and 1 TeV, possibly extending later up to 5 TeV. For the TESLA design this corresponds to an integrated luminosity of $\int \mathcal{L} = 300$ fb$^{-1}$ per year at 500 GeV and of 500 fb$^{-1}$ for a c.m. energy of 800 GeV [10].

The structure of the thesis which reflects the experimental scheme to be pursued is as follows. Chapter 2 will start with the setting of the scene by describing the SM Higgs couplings and the MSSM Higgs sector from the theoretical point of view.

The third Chapter will be devoted to the Higgs boson search at $pp$ colliders and in $e^+e^-$ collisions. First, the production mechanisms will be reviewed before turning on to the perspectives for the Higgs discovery in the diverse decay channels at the two collider types. The final picture will display a parameter region in which the discovery of the heavy MSSM Higgs bosons will be difficult if not impossible. Therefore the production and discovery potential in the $\gamma\gamma$ mode at $e^+e^-$ linear colliders will be analysed. Using Weizsäcker-Williams photons for the production of Higgs bosons provides too small a number of events. The rate is sufficiently large, however, if the photons are produced through the backscattering of laser light from high-energy electron/positron beams. This mechanism [11] allows for the production of real photons with high energy, luminosity [12] and monochromaticity and a high degree of polarization of the scattered photons. Several decay channels will be examined with regard to a sufficiently large signal to background ratio. Next-to-leading order corrections will be included and where necessary the resummation of large logarithms will thoroughly be taken into account.

Once the Higgs boson will be discovered and its mass will be determined, the next step is the measurement of the Higgs couplings to the gauge and matter particles via the Higgs decays. Chapter 4 will present the branching ratios for the various decay channels of the SM Higgs scalar and the MSSM Higgs bosons. The knowledge of the branching ratios and the decay widths allows for the extraction of the lifetime of the Higgs bosons, which together with the mass forms the basic characteristics of particles. Therefore, Chapter 4 will continue with evolving the theoretical set-up for the determination of the SM and MSSM Higgs lifetimes in a model-independent way. Some representative examples at $e^+e^-$ colliders will be given.

The first Chapters describe the determination of the necessary ingredients, *i.e.* the mass and lifetime of the Higgs states and the Yukawa and gauge-Higgs boson couplings, from a theoretical and experimental point of view, enabling finally the measurement of the Higgs self-couplings. Chapter 5 deals with this task which is essential in order to establish experimentally the Higgs sector harboring the mechanism for the generation of particle masses. Special emphasis will hence be on this part of the thesis. The plethora of mechanisms which allow the access to the trilinear Higgs self-couplings in $pp$ and $e^+e^-$ collisions will be described. The final picture unveils a theoretically conclusive way of determining all possible trilinear Higgs self-couplings in the SM and the MSSM. The size of the cross sections for these processes will be discussed including a short sideview on the ones involving self-couplings among four Higgs particles. The phenomenological implications, in particular the perspectives for the measurement of the trilinear Higgs self-couplings will be examined by reviewing existing background studies.

The thesis will be concluded with a summary of the salient features of the investigation of the Higgs sector in the SM and the MSSM.

# Chapter 2

# The SM and the MSSM Higgs sector

## 2.1 The Higgs particle of the Standard Model

The dynamics of the $SU(2)_L$ Higgs doublet field $\Phi$, introduced in order to ensure unitarity and to provide a mechanism for the generation of masses without violating gauge principles, is described by the Lagrangean

$$\mathcal{L}_\Phi = (D_\mu \Phi)^\dagger (D^\mu \Phi) - V(\Phi) \tag{2.1}$$

where $V$ denotes the Higgs self-interaction potential

$$V = \lambda \left[ \Phi^\dagger \Phi - \frac{1}{2} v^2 \right]^2 \tag{2.2}$$

with a minimum at $\langle \Phi \rangle_0 = (0, v/\sqrt{2})$. By introducing the Higgs field in the unitary gauge

$$\Phi = \frac{1}{\sqrt{2}} \left( \begin{array}{c} 0 \\ v + H \end{array} \right) \tag{2.3}$$

the potential Eq. (2.2) can be cast into the form

$$V_H = \frac{1}{2}(2\lambda v^2) H^2 + \lambda v H^3 + \frac{\lambda}{4} H^4 \tag{2.4}$$

where the Higgs mass $M_H$ and the Higgs self-interactions can be read off directly. Apparently, the Higgs mass

$$M_H = \sqrt{2\lambda} v \tag{2.5}$$

is related to the quadrilinear coupling $\lambda$. The trilinear Higgs self-coupling can be expressed as

$$\lambda_{HHH} = 3 M_H^2 / M_Z^2 \tag{2.6}$$

in units of $\lambda_0 = M_Z^2/v$ and the self-coupling among four Higgs bosons in units of $\lambda_0^2$ is given by

$$\lambda_{HHHH} = 3 M_H^2 / M_Z^4 \tag{2.7}$$

where $\lambda_0 = 33.8$ GeV, numerically. For a typical energy scale $M_Z$ and a Higgs mass $M_H = 110$ GeV, the trilinear Higgs self-coupling equals to $\lambda_{HHH} \lambda_0 / M_Z = 1.6$. In contrast, the quadrilinear coupling $\lambda_{HHHH}\lambda_0^2 = 0.6$ is suppressed compared to the trilinear coupling by a factor of about the weak gauge coupling. Evidently, in the SM the Higgs self-couplings are uniquely defined by the mass of the Higgs boson.

The covariant derivative in (2.1) is given by

$$D_\mu = i\partial_\mu + gT_aW_\mu^a - g'\frac{Y}{2}B_\mu \tag{2.8}$$

and $(D_\mu\Phi)^\dagger(D^\mu\Phi)$ hence describes the kinetic Higgs term and the interaction between Higgs and gauge bosons. $T_a$ $(a = 1, 2, 3)$ denote the isospin-generators of the $SU(2)_L$ gauge group and $Y$ corresponds to the $U(1)_Y$ hypercharge-generator. $g$ and $g'$ are the electroweak couplings and $W_\mu^a$ and $B_\mu$ are the gauge fields associated with the two symmetry groups, respectively. After introducing the physical Higgs field (2.3) and transforming the electroweak eigenstates $W_\mu^a$, $B_\mu$ to the mass eigenstates, the kinetic term in Eq. (2.1) yields the mass terms for the electroweak gauge bosons $W^\pm$, $Z$ and the photon field $A$

$$M_W = \frac{1}{2}gv, \quad M_Z = \frac{1}{2}\sqrt{g^2+g'^2}v, \quad M_A = 0 \tag{2.9}$$

as well as the Higgs-gauge boson interaction strengths

$$\lambda_{HVV} = 2(\sqrt{2}G_F)^{1/2}M_V^2\ , \qquad \lambda_{HHVV} = 2(\sqrt{2}G_F)M_V^2\ , \qquad [V = W, Z] \tag{2.10}$$

The interaction between the Higgs boson and fermions must respect the $SU(2)_L \times U(1)_Y$ gauge symmetry and maintain the renormalizability of the theory. The operators which fulfill these conditions are combined in the Yukawa Lagrangean

$$\mathcal{L}_{yuk} = -\bar{E}_R C_E \Phi^\dagger L_L + \bar{U}_R C_U \Phi_i^T \epsilon_{ij} Q'_{Lj} - \bar{D}'_R C_D \Phi^\dagger Q'_L \tag{2.11}$$

with

$$E = (e, \mu, \tau)^T, \qquad U = (u, c, t)^T, \qquad D' = (d', s', b')^T \tag{2.12}$$

and

$$Q'_L = \left(\begin{array}{c} U \\ D' \end{array}\right)_L, \qquad L_L = \left(\begin{array}{c} N \\ E \end{array}\right)_L, \quad \text{where} \quad N_L = (\nu_{eL}, \nu_{\mu L}, \nu_{\tau L})^T \tag{2.13}$$

The right-handed fermions denoted by the index $R$ behave as singlets under $SU(2)_L$-transformations whereas the left-handed fermions denoted by the index $L$ are combined in isospin-doublets. The prime indicates that the corresponding quarks are given in the electroweak basis which is connected to the basis of the mass eigenstates via the unitary Cabibbo-Kobayashi-Maskawa matrix $V$ [13], $D' = VD$. The $3 \times 3$ matrices $C_E, C_U, C_D$ are unitary. By appropriate change of the basis $(E, U, D')$ with a constant $U(3)$-matrix and making use of the unitarity of the matrices $C_i$, Eq. (2.11) provides the fermion mass terms $m_f$ after expanding $\Phi$ around the VEV, cf. Eq. (2.3). They are related to the Higgs fermion interaction coefficient via

$$\lambda_{Hff} = (\sqrt{2}G_F)^{1/2}m_f \tag{2.14}$$

Taking into account the recent indication of massive neutrinos one possibility to include them in the theory is the addition of an operator containing right-handed Dirac neutrinos to the Yukawa Lagrangean:

$$\bar{N}_R C_N \Phi_i^T \epsilon_{ij} L'_{Lj} \tag{2.15}$$

and changing the mass eigenstates $E$ to electroweak eigenstates $E'$,

$$E \rightarrow E' \tag{2.16}$$

This Yukawa Lagrangean leads then to a Dirac mass term for neutrinos and furthermore encounters a "Cabibbo-Kobayashi-Maskawa" matrix $V_E$ for charged leptons transforming the electroweak eigenstates $E'$ to mass eigenstates $E$:

$$E' = V_E E \tag{2.17}$$

There are also other possibilities of implementing massive neutrinos in the theory.

## 2.2 Supersymmetry

### 2.2.1 The Minimal Supersymmetric Standard Model

In the minimal realization of a supersymmetric theory, the MSSM, a minimal number of supersymmetric particles is introduced as partners to the SM particles. The scalar partners of quarks and leptons are called squarks and sleptons with the degrees of freedom corresponding to the degrees of freedom of the SM states. The fermions and their supersymmetric partners are combined in chiral superfields. For reasons described below, the MSSM which includes the same $SU(3) \times SU(2)_L \times U(1)_Y$ gauge symmetry as the SM contains two $SU(2)_L$ Higgs doublets. They are associated with $SU(2)_L$ doublets of Majorana fermion fields, the higgsinos. The electroweak gauge bosons and the gluons also acquire SUSY partners with spin 1/2, which are called gauginos and gluinos, respectively. Charginos and neutralinos are the physical mass eigenstates of the higgsinos and gauginos and are given by linear combinations of these fields. Gauge bosons and their supersymmetric partners are described by vector superfields. The particles in a superfield differ only by spin 1/2. Since supersymmetry relates fermions and bosons, the particles in a supermultiplet have equal masses and residual quantum numbers in an unbroken supersymmetric theory.

The superfields are introduced in order to build up the supersymmetric Lagrangean, and the space-time integral over the Lagrange density is extended to a superspace integral which involves two more dimensions. They correspond to two-component Grassmann variables, denoted by $\theta$ and $\bar{\theta}$. The superfields can be expanded in terms of these Grassmann variables developing the component fields of the supermultiplets as coefficients in these finite series. The so-called $F$ term is the one proportional to $\theta\theta$ in the expansion of the chiral superfield. The $D$ term represents the contribution proportional $\theta^2\bar{\theta}^2$ in the vector superfield expansion [5]. Starting with a theory without gauge fields, the supermultiplets can be described using chiral superfields $\Phi_i$ only. Since a renormalizable theory must not contain higher orders than three in $\Phi_i$, the Lagrangean for chiral superfields is given by

$$\mathcal{L} = \sum_i (\bar{\Phi}_i \Phi_i)_D + (\mathcal{W} + \bar{\mathcal{W}})_F \tag{2.18}$$

with the superpotential

$$\mathcal{W} = \sum_{ijk} (m_{ij}\Phi_i\Phi_j + \lambda_{ijk}\Phi_i\Phi_j\Phi_k) \tag{2.19}$$

The products $\Phi^2$ and $\Phi^3$ are chiral again and the real product $\bar{\Phi}\Phi$ forms a vector field. The subscripts $D$ and $F$ denote the prescriptions for taking the $D$ and $F$ terms in the expansion of the superfield products, respectively. The analytical superpotential $\mathcal{W}$ must not contain complex conjugate superfields. Neither will the scalar potential contain complex conjugate component Higgs fields. As anticipated, two Higgs doublets are required in order to give masses to both the up- and down-type quarks. Integrating out the Grassmann variables and using the Euler-Lagrange equations

$$F_i = -\frac{\partial \bar{\mathcal{W}}(\bar{A})}{\partial \bar{A}_i} \tag{2.20}$$

the scalar potential is given by

$$\mathcal{V} = \sum_i |F_i|^2 \tag{2.21}$$

where the Yukawa terms included in $\mathcal{W}$ have been dropped. $A$ is a complex scalar component field in the expansion of the scalar superfield.

Including a non-abelian gauge sector the Lagrangean for a minimal supersymmetric gauge theory in the Wess-Zumino gauge reads [14]

$$\begin{aligned} \mathcal{L} &= \sum_{ij} \left[ \bar{\Phi}_i \left( e^{2gV^aT^a} \right)_{ij} \Phi_j \right]_D \\ &+ \left[ \tfrac{1}{4C(R)} Tr(W^\alpha W_\alpha) + \mathcal{W}(\Phi_i) \right]_F + h.c. \end{aligned} \tag{2.22}$$

The non-abelian field strength superfield $W_\alpha$ is given by

$$W_\alpha = -\frac{1}{8g} \bar{D}^2 e^{-2gV} \left( D_\alpha e^{2gV} \right) \tag{2.23}$$

$D_\alpha$ is the covariant derivative acting on superspace. $g$ denotes the non-abelian gauge coupling and $V$ reads

$$V = V^a T^a \tag{2.24}$$

where $V^a$ denotes a vector supermultiplet and $T^a$ are the generators of the Lie-Algebra. They are normalized to

$$Tr[T^a T^b] = C(R)\delta^{ab} \tag{2.25}$$

The factor $C$ depends on the representation $R$. Integrating out the Grassmann fields the scalar potential for a non-abelian gauge theory can be read off from (2.22):

$$\mathcal{V} = \sum_i |F_i|^2 + \frac{1}{2}\sum_a (D^a)^2 \tag{2.26}$$

The auxiliary fields $F_i$ and $D^a$ are given by the Euler-Lagrange equations,

$$\begin{aligned} F_i &= -\frac{\partial \bar{\mathcal{W}}(\bar{A})}{\partial \bar{A}_i} \\ D^a &= -\sum_{ij} g \bar{A}_i (T^a)_{ij} A_j \end{aligned} \tag{2.27}$$

$A_i$ are scalar fields that belong to the the fundamental representation of a general non-abelian $SU(N)$ gauge group. A $U(1)$ gauge multiplet can be included in the scalar potential by adding

$$\frac{1}{2}(D')^2 \tag{2.28}$$

to Eq. (2.26). $D'$ is defined by

$$D' = \sum_i g' \frac{Y}{2} \bar{A}_i A_i + \xi \tag{2.29}$$

$g'$ denotes the $U(1)$ gauge coupling and $Y$ the generator of the abelian group. The constant Fayet-Iliopoulos term $\xi$ [15] can in many models argued to be small [16] and will be set equal to zero in the following.

The superpotential as given in (2.19) implies lepton and baryon number violating interactions which may lead to proton decay at tree level by exchanging a s-down-quark. In the SM, no such problem occurs since the corresponding interactions do not arise due to gauge invariance unless the dimension of the operators is larger than six. In order to avoid the problem in the MSSM, the corresponding couplings must either be suppressed or the interactions must be forbidden by a symmetry. The $\mathbb{Z}_2$ symmetry under which the Grassmann variables in the Lagrangean change sign fulfills this condition. The symmetry is called $R$ parity and characterized by a multiplicative quantum number which can be defined as

$$R = (-1)^{(3B+L+2S)} \tag{2.30}$$

where $B$ is the baryon number, $L$ the lepton number and $S$ the spin of the particle. The SM particles have $R$ parity $+1$ whereas their SUSY partners have $R$ parity $-1$. From the phenomenological point of view, the assumption of $R$ parity conservation implies that SUSY partners can only be pair produced in collisions of SM particles. Furthermore, a theory with $R$ parity conservation contains a lightest SUSY particle (LSP) which is stable.

So far no SUSY particle with the same mass as its corresponding SM partner has been observed. In order to explain the experiments the SUSY particles must be assumed to be heavier than their SM counterparts. Hence supersymmetry has to be broken. For the time being, supersymmetry is usually broken by introducing explicit soft mass terms [17] and regarding the MSSM as an effective low energy theory [18]. The mass terms are called soft because they are chosen such that they do not develop quadratic divergences again. The form of the soft-breaking terms is restricted by the requirement of gauge invariance as well as weak-scale $R$ parity invariance and stable scalar masses. A further constraint is set by the experimental bounds. In generic notation they are given by

- $-m_{ij}^2 S_i^* S_j$

  where $S_i$ denote scalar component fields and $m_{ij}^2$, $i, j = 1, ..., n$, scalar mass matrices for squarks and sleptons with $n$ generations. There are two masses for the Higgs scalars and a complex mass term mixing the scalar components of the two Higgs doublets:

  $\tilde{m}_1^2 |H_1|^2 + \tilde{m}_2^2 |H_2|^2 - [B\mu H_1 H_2 + h.c.]$

  The Higgs fields $H_1$ and $H_2$ are contracted using $\epsilon_{ij}$ ($\epsilon_{12} = 1$) and $\mu$ is called mixing parameter.

- $-\frac{1}{2}[m_i'\lambda_i\lambda_i + h.c.]$
  for Majorana fermions $\lambda_i$ with three real gaugino masses $m_i'$, $i = 1, 2, 3$.
- $-[A_{ijk}C_iC_jC_k + h.c.]$
  which involves scalar fields $C_i$. $A_{ijk}$ $[i, j, k = 1, 2, 3]$ are complex trilinear couplings respecting $R$ parity. Non-zero trilinear couplings $A_{ijk}$ lead to a mixing of the left- and right-handed sfermions.

### 2.2.2 The MSSM Higgs sector

The MSSM Higgs potential can be derived using Eqs. (2.26)–(2.29) [3, 5, 6]. The contribution $V_D$ due to the $D$ term

$$V_D = \frac{1}{2}\sum_a (D^a)^2 + \frac{1}{2}(D')^2 \tag{2.31}$$

for two Higgs doublets $H_1$, $H_2$ with hypercharges $Y = -1$ and $Y + 1$, respectively, is given by

$$D_{U(1)_Y} = -\frac{g'}{2}\left(|H_2|^2 - |H_1|^2\right) \tag{2.32}$$

$$D^a_{SU(2)_L} = -\frac{g}{2}\left(H_1^{i*}\sigma^a_{ij}H_1^j + H_2^{i*}\sigma^a_{ij}H_2^j\right) \tag{2.33}$$

where $T^a = \sigma^a/2$ and $\sigma^a$ $(a = 1, 2, 3)$ are the Pauli matrices. The second contribution to the potential arises from the derivative of the superpotential with respect to the chiral superfields. The superpotential $\mathcal{W}$ conserving baryon and lepton number and respecting the $SU(3) \times SU(2)_L \times U(1)_Y$ symmetry is given by

$$\mathcal{W} = -\epsilon_{ij}\mu\hat{H}_1^i\hat{H}_2^j + \epsilon_{ij}[\lambda_L\hat{H}_1^i\hat{L}_L^j\hat{\bar{E}}_R + \lambda_D\hat{H}_1^i\hat{Q}_L^j\hat{\bar{D}}_R + \lambda_U\hat{H}_2^j\hat{Q}_L^i\hat{\bar{U}}_R] \tag{2.34}$$

$\hat{H}_k$ $(k = 1, 2)$ are the superfields containing the Higgs fields $H_k$ and their SUSY partners. The $SU(2)_L$ doublet superfield $\hat{L}_L$ includes the left-handed electron and neutrino and the corresponding scalar particles. The superfield $\hat{\bar{E}}_R$ contains the right-handed anti-electron and its scalar partner. $\hat{Q}_L$ includes an $SU(2)_L$ doublet of quarks and the associated SUSY partners. $\hat{\bar{U}}_R$ $(\hat{\bar{D}}_R)$ consists of the right-handed up- (down-) antiquark and its supersymmetric counterpart. For the sake of simplicity the superpotential is given only for the first generation. The supersymmetric potential can then be cast into the form

$$V = |\mu|^2\left(|H_1|^2 + |H_2|^2\right) + \frac{g^2 + g'^2}{8}\left(|H_1|^2 - |H_2|^2\right)^2 + \frac{g^2}{2}|H_1^*H_2|^2 \tag{2.35}$$

The minimum of the potential is given by $\langle H_1^0\rangle = \langle H_2^0\rangle = 0$ with $V = 0$. So far no violation of supersymmetry has been applied. Including the possible soft SUSY breaking terms, the potential is given by

$$\begin{aligned} V_H &= m_{11}^2|H_1|^2 + m_{22}^2|H_2|^2 - m_{12}^2\epsilon_{ij}\left(H_1^iH_2^j + h.c.\right) + \frac{g^2 + g'^2}{8}\left(|H_1|^2 - |H_2|^2\right)^2 \\ &\quad + \frac{g^2}{2}|H_1^*H_2|^2 \end{aligned} \tag{2.36}$$

where the squared masses are

$$\begin{aligned} m_{11}^2 &= |\mu|^2 + \tilde{m}_1^2 \\ m_{22}^2 &= |\mu|^2 + \tilde{m}_2^2 \\ m_{12}^2 &= \mu B \end{aligned} \tag{2.37}$$

with $\tilde{m}_1^2$, $\tilde{m}_2^2$ and $\mu B$ being the soft SUSY breaking mass parameters. $V_H$ manifestly conserves CP invariance as any complex phase in $\mu B$ can be absorbed by redefining the Higgs fields. The electroweak symmetry is broken for non-vanishing vacuum expectation values of the neutral components of the Higgs doublets,

$$\langle H_1 \rangle = \begin{pmatrix} \frac{v_1}{\sqrt{2}} \\ 0 \end{pmatrix} \quad , \qquad \langle H_2 \rangle = \begin{pmatrix} 0 \\ \frac{v_2}{\sqrt{2}} \end{pmatrix} \tag{2.38}$$

By appropriate choice of the phases of the Higgs fields, $v_1$ and $v_2$ can always be adjusted real and positive. The relation of the VEVs $v_1$ and $v_2$ defines the angle $\beta$,

$$\tan\beta = \frac{v_2}{v_1} \tag{2.39}$$

For positive $v_1$, $v_2$, $0 \le \beta \le \pi/2$. The potential acquires a stable minimum if the following conditions are fulfilled:

$$\begin{aligned} m_{11}^2 + m_{22}^2 &> 2\,|m_{12}^2| \\ m_{11}^2 m_{22}^2 &< |m_{12}^2|^2 \end{aligned} \tag{2.40}$$

The MSSM Higgs potential may be compared to a general self-interaction potential of two Higgs doublets $\varphi_i$ in a CP-conserving theory

$$\begin{aligned} V^{2HDM}[\varphi_1, \varphi_2] &= m_{11}^2 \varphi_1^\dagger \varphi_1 + m_{22}^2 \varphi_2^\dagger \varphi_2 - [m_{12}^2 \varphi_1^\dagger \varphi_2 + \text{h.c.}] \\ &+ \tfrac{1}{2}\lambda_1 (\varphi_1^\dagger \varphi_1)^2 + \tfrac{1}{2}\lambda_2 (\varphi_2^\dagger \varphi_2)^2 + \lambda_3 (\varphi_1^\dagger \varphi_1)(\varphi_2^\dagger \varphi_2) + \lambda_4 (\varphi_1^\dagger \varphi_2)(\varphi_2^\dagger \varphi_1) \\ &+ \left\{ \tfrac{1}{2}\lambda_5 (\varphi_1^\dagger \varphi_2)^2 + [\lambda_6 (\varphi_1^\dagger \varphi_1) + \lambda_7 (\varphi_2^\dagger \varphi_2)] \varphi_1^\dagger \varphi_2 + \text{h.c.} \right\} \end{aligned} \tag{2.41}$$

The seven couplings $\lambda_i$ and the three mass parameters $m_{11}^2$, $m_{22}^2$, $m_{12}^2$ are real. By applying the relations between the fields $\varphi_i$ and the Higgs doublets $H_1$ and $H_2$ with opposite hypercharge [6]

$$(\varphi_1)^j = \epsilon_{ij} H_1^{i*} \,, \qquad (\varphi_2)^j = H_2^j \tag{2.42}$$

one will find that in the MSSM the $\lambda$ parameters at tree level are uniquely defined in terms of the electroweak gauge couplings [3, 5, 6, 19]

$$\begin{aligned} \lambda_1 &= \lambda_2 = \tfrac{1}{4}(g^2 + g'^2) \\ \lambda_3 &= \tfrac{1}{4}(g^2 - g'^2) \\ \lambda_4 &= -\tfrac{1}{2} g^2 \\ \lambda_5 &= \lambda_6 = \lambda_7 = 0 \end{aligned} \tag{2.43}$$

The two complex $SU(2)_L$ Higgs doublets have eight degrees of freedom. After the electroweak symmetry breaking three of them will be absorbed to provide longitudinal degrees of freedom to the electroweak gauge bosons. The remaining five degrees of freedom correspond to the equivalent number of physical Higgs states, two charged Higgs bosons $H^\pm$, a CP-odd neutral Higgs boson $A$ and two CP-even neutral Higgs bosons $h$ and $H$ [3, 5, 6]. Expanding the Higgs doublets $H_i$ around their vacuum expectation values leads to the mass matrix $M^2_{ij}$ for the component fields $\eta_i$ of the Higgs doublets

$$M^2_{ij} = \left.\frac{\partial^2 V_H}{\partial\eta_i \partial\eta_j}\right|_{min} \tag{2.44}$$

with the minimum given by $\langle 0|\eta_i|0\rangle = 0$. Diagonalizing the mass matrix (2.44) the masses for the physical Higgs states are obtained in terms of the parameters in the Higgs potential $V_H$. The parameters change when top and stop-loop radiative corrections are included. In the one-loop leading $m_t^4$ approximation, where $m_t$ denotes the top mass, they can be approximated by

$$\epsilon \approx \frac{3G_F m_t^4}{\sqrt{2}\pi^2 \sin^2\beta} \ln \frac{\tilde{M}^2}{m_t^2} \tag{2.45}$$

with the common squark-mass value $\tilde{M}$ setting the scale of supersymmetry breaking. Provided that stop mixing effects are moderate at the SUSY scale, they can be implemented by shifting $\tilde{M}^2$ in $\epsilon$

$$\begin{aligned} \tilde{M}^2 \to \tilde{M}^2 + \Delta\tilde{M}^2 \quad : \quad \Delta\tilde{M}^2 &= \hat{A}^2[1 - \hat{A}^2/(12\tilde{M}^2)] \\ \hat{A} &= A - \mu\cot\beta \end{aligned} \tag{2.46}$$

where $A$ and $\mu$ correspond to the trilinear coupling in the top sector and the higgsino mass parameter in the superpotential, respectively. Using the mass $M_A$ and $\tan\beta$ as input parameters the charged Higgs mass and the masses for the neutral CP-even Higgs bosons as well as the mixing angle $\alpha$ in the neutral sector are given by

$$\begin{aligned} M^2_{H^\pm} &= M_A^2 + M_W^2 \\ M^2_{h,H} &= \tfrac{1}{2}\left[M_A^2 + M_Z^2 + \epsilon \mp \sqrt{(M_A^2 + M_Z^2 + \epsilon)^2 - 4M_A^2 M_Z^2 \cos^2 2\beta - 4\epsilon(M_A^2 \sin^2\beta + M_Z^2\cos^2\beta)}\right] \\ \tan 2\alpha &= \tan 2\beta \frac{M_A^2 + M_Z^2}{M_A^2 - M_Z^2 + \epsilon/\cos 2\beta} \qquad \text{with} \qquad -\frac{\pi}{2} \leq \alpha \leq 0 \end{aligned} \tag{2.47}$$

in the $\epsilon$ approximation. Evidently, at tree level, where $\epsilon = 0$, the parameters of the Higgs potential can be expressed by the electroweak and two additional parameters which are usually chosen as $M_A$ and $\tan\beta$. [The mass $M_A$ is related to $m_{12}$ via $M_A^2 = m_{12}^2/\sin\beta\cos\beta$. The masses $m_{11}, m_{22}$ can be eliminated by minimizing the potential.] The Born masses fulfill the following conditions

$$\begin{aligned} M_H &> M_A, M_Z > M_h \\ M_{H^\pm} &> M_A, M_W \\ M_h &< M_Z|\cos 2\beta| \end{aligned} \tag{2.48}$$

When radiative corrections are taken into account the upper bound of the light neutral Higgs mass $M_h$ will extend to about 130 GeV [20, 21]. In contrast, the masses of the heavy CP-even and CP-odd neutral Higgs bosons $H$, $A$, and the charged Higgs particles $H^\pm$ may vary in the mass range from the order of the electroweak symmetry scale $v$ up to about 1 TeV.

After introducing the physical Higgs states the self-couplings among the Higgs bosons can be derived from (2.36). Respecting CP-invariance there are six trilinear couplings among the neutral Higgs bosons $h$ and $H$. In units of $\lambda_0 = M_Z^2/v$, $v = \sqrt{v_1^2 + v_2^2}$, they may be written as [20, 22, 23]

$$\begin{aligned}
\lambda_{hhh} &= 3\cos 2\alpha \sin(\beta+\alpha) + 3\frac{\epsilon}{M_Z^2}\frac{\cos\alpha}{\sin\beta}\cos^2\alpha \\
\lambda_{Hhh} &= 2\sin 2\alpha \sin(\beta+\alpha) - \cos 2\alpha \cos(\beta+\alpha) + 3\frac{\epsilon}{M_Z^2}\frac{\sin\alpha}{\sin\beta}\cos^2\alpha \\
\lambda_{HHh} &= -2\sin 2\alpha \cos(\beta+\alpha) - \cos 2\alpha \sin(\beta+\alpha) + 3\frac{\epsilon}{M_Z^2}\frac{\cos\alpha}{\sin\beta}\sin^2\alpha \\
\lambda_{HHH} &= 3\cos 2\alpha \cos(\beta+\alpha) + 3\frac{\epsilon}{M_Z^2}\frac{\sin\alpha}{\sin\beta}\sin^2\alpha \\
\lambda_{hAA} &= \cos 2\beta \sin(\beta+\alpha) + \frac{\epsilon}{M_Z^2}\frac{\cos\alpha}{\sin\beta}\cos^2\beta \\
\lambda_{HAA} &= -\cos 2\beta \cos(\beta+\alpha) + \frac{\epsilon}{M_Z^2}\frac{\sin\alpha}{\sin\beta}\cos^2\beta \qquad (2.49)
\end{aligned}$$

In the decoupling limit $M_A^2 \sim M_H^2 \sim M_{H^\pm}^2 \gg v^2/2$,

$$\sin(\beta-\alpha) \to 1 \qquad (2.50)$$

$$\cos(\beta-\alpha) \to 0 \qquad (2.51)$$

and the trilinear Higgs couplings approach the values

$$\begin{aligned}
\lambda_{hhh} &\longrightarrow 3M_h^2/M_Z^2 \\
\lambda_{Hhh} &\longrightarrow -3\sqrt{\left(\frac{M_h^2}{M_Z^2} - \frac{\epsilon}{M_Z^2}\sin^2\beta\right)\left(1 - \frac{M_h^2}{M_Z^2} + \frac{\epsilon}{M_Z^2}\sin^2\beta\right)} - \frac{3\epsilon}{M_Z^2}\sin\beta\cos\beta \\
\lambda_{HHh} &\longrightarrow 2 - \frac{3M_h^2}{M_Z^2} + \frac{3\epsilon}{M_Z^2} \\
\lambda_{HHH} &\longrightarrow 3\sqrt{\left(\frac{M_h^2}{M_Z^2} - \frac{\epsilon}{M_Z^2}\sin^2\beta\right)\left(1 - \frac{M_h^2}{M_Z^2} + \frac{\epsilon}{M_Z^2}\sin^2\beta\right)} - \frac{3\epsilon}{M_Z^2}\frac{\cos^3\beta}{\sin\beta} \\
\lambda_{hAA} &\longrightarrow -\frac{M_h^2}{M_Z^2} + \frac{\epsilon}{M_Z^2} \\
\lambda_{HAA} &\longrightarrow \sqrt{\left(\frac{M_h^2}{M_Z^2} - \frac{\epsilon}{M_Z^2}\sin^2\beta\right)\left(1 - \frac{M_h^2}{M_Z^2} + \frac{\epsilon}{M_Z^2}\sin^2\beta\right)} - \frac{\epsilon}{M_Z^2}\frac{\cos^3\beta}{\sin\beta} \qquad (2.52)
\end{aligned}$$

with $M_h^2 = M_Z^2\cos^2 2\beta + \epsilon\sin^2\beta$. Evidently, the self-coupling of the light CP-even neutral Higgs boson $h$ reaches the SM value in the decoupling limit.

### 2.2.3 The Higgs-Yukawa and the Higgs-gauge couplings

The couplings of the MSSM Higgs particles to the fermions and gauge bosons can be derived in the framework of the superspace formalism from the Yukawa Lagrangean and the kinetic term for the two Higgs doublets, respectively [3, 5, 6]. The procedure is analogous to the SM bearing in mind that two $SU(2)_L$ complex scalar doublets are involved in the MSSM. Expanding around the VEVs and transforming to the Higgs mass eigenstates, the couplings given in Table 2.1 will be found normalized to the SM [3, 5, 6]. They depend on the ratio of the vacuum expectation values, $\tan\beta$, and the mixing angle $\alpha$ which was introduced in

| $\Phi$ | | $g_{\Phi\bar{u}u}$ | $g_{\Phi\bar{d}d}$ | $g_{\Phi VV}$ |
|---|---|---|---|---|
| $SM$ | $H$ | $1$ | $1$ | $1$ |
| $MSSM$ | $h$ | $\cos\alpha/\sin\beta$ | $-\sin\alpha/\cos\beta$ | $\sin(\beta-\alpha)$ |
| | $H$ | $\sin\alpha/\sin\beta$ | $\cos\alpha/\cos\beta$ | $\cos(\beta-\alpha)$ |
| | $A$ | $1/\tan\beta$ | $\tan\beta$ | $0$ |

Table 2.1: Yukawa and gauge boson $[V = W, Z]$ Higgs couplings in the MSSM normalized to the SM couplings.

order to diagonalize the mass matrix in the neutral CP-even Higgs sector.

The Higgs gauge couplings $g_{hVV}$ and $g_{HVV}$ are suppressed with respect to the corresponding SM couplings by the factors $\sin(\beta-\alpha)$ and $\cos(\beta-\alpha)$, respectively. Only in the decoupling limit the light CP-even Higgs boson gauge coupling approaches the SM value whereas the coupling for $H$ becomes zero. For the pseudoscalar Higgs particle $A$ there exists no coupling to the gauge bosons at tree level due to CP-invariance.

The Yukawa gauge couplings of the CP-even neutral MSSM Higgs bosons to up- (down-) type quarks are inversely proportional to $\sin\beta$ ($\cos\beta$). Their variation with $M_A$ is shown for two values of $\tan\beta = 3, 50$ in Fig. 2.1. Evidently, for large values of $M_A$, *i.e.* in the decoupling limit, the couplings involving $h$ approach the SM values whereas for small values of $M_A$ this rôle is taken over by the heavy CP-even Higgs boson $H$. The Yukawa couplings of the CP-odd Higgs boson $A$ to up- (down-)type quarks are suppressed (enhanced) for large values of $\tan\beta$.

The couplings in Table 2.1 determine the decay modes of the MSSM Higgs bosons and therefore their experimental signatures. Thus it will be difficult in the decoupling limit to distinguish the light scalar MSSM Higgs boson from the SM Higgs particle.

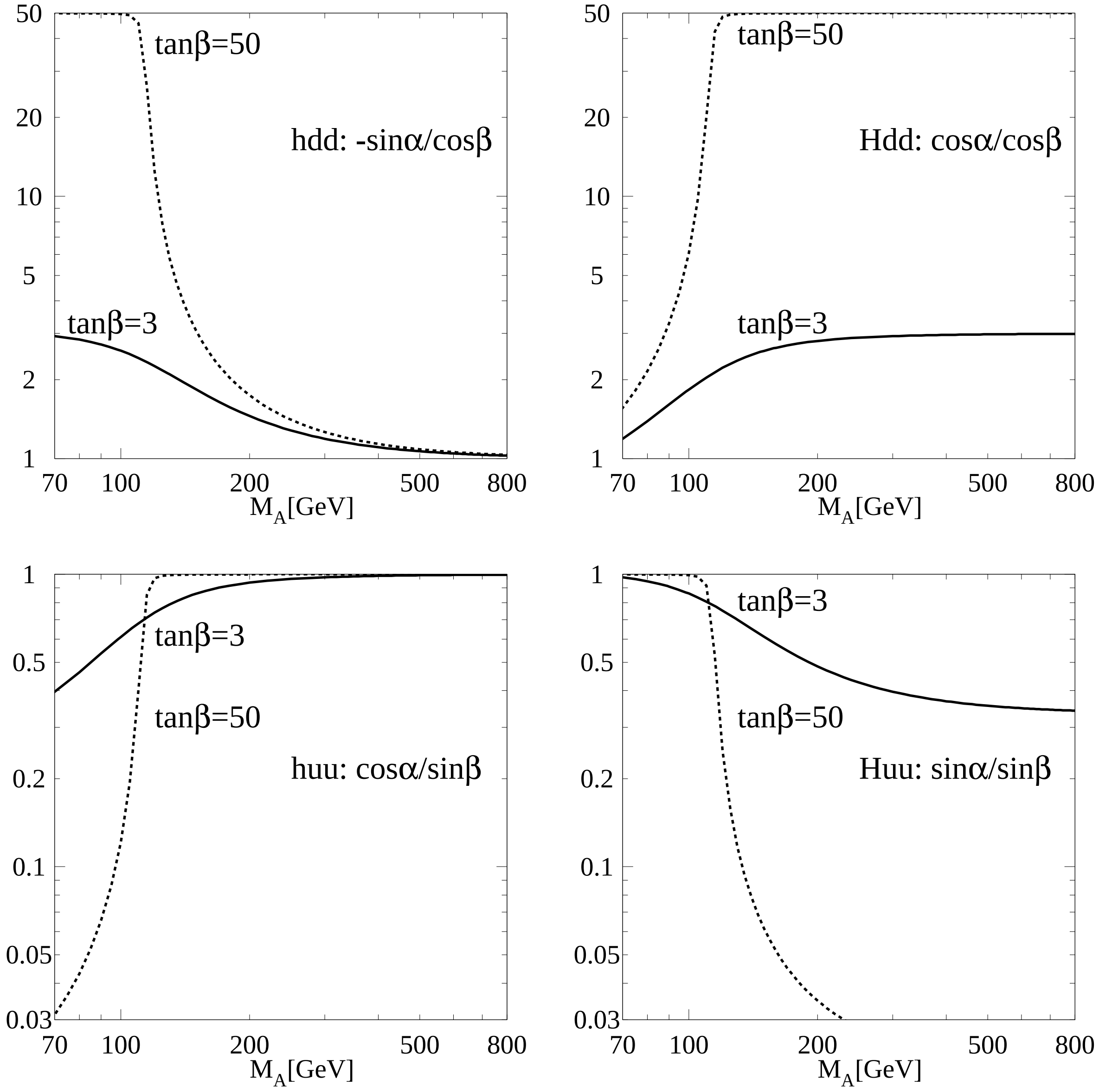

Figure 2.1: *The Yukawa couplings of the neutral CP-even Higgs bosons to up- and down-type quarks, respectively, in units of the SM couplings as a function of* $M_A$ *for two values of* $\tan\beta = 3, 50$ *and vanishing mixing.*

# Chapter 3

# Higgs boson search

The mass of the Higgs boson cannot be predicted within the framework of the SM. Its value can be constrained, however, by the assumption that the model is valid up to an energy scale $\Lambda$. Demanding that the SM remains perturbative up to the GUT scale $\mathcal{O}(10^{16}$ GeV), an upper bound of the Higgs mass is given by $\sim 200$ GeV. For $\Lambda \sim 1$ TeV and the constraint $M_H \leq \Lambda$ lattice simulations [24] and renormalization group analyses [25, 26] predict an upper bound of $\sim 700$ GeV.

A lower bound on the Higgs mass is given by the requirement of vacuum stability. The quantum corrections to the quartic self-coupling $\lambda$ due to the Higgs self-interaction are positive whereas those from the top-Yukawa coupling are negative. Depending on the value of $\lambda$ at the scale of the Higgs mass the quartic coupling increases with the energy or is driven to negative values so that the vacuum becomes unstable depending on the top-quark mass. Since the strength of the Higgs self-interaction is determined by the Higgs mass at the scale $M_H$ the negative contribution can be compensated if $M_H$ is large enough. Assuming a top mass of 175 GeV the SM remains weakly interacting up to $\sim 1$ TeV if the lower bound of the Higgs mass is given by $\sim 55$ GeV. For $\Lambda \sim M_{\mathrm{GUT}}$ the lower bound increases to 130 GeV. If the vacuum is metastable with a lifetime exceeding the age of the universe, the lower Higgs mass bound decreases. While the bound changes only slightly for $\Lambda \sim M_{\mathrm{GUT}}$, the effect is significant for $\Lambda \sim 1$ TeV [25].

The direct Higgs boson search in the Higgs-strahlung process at LEP2 , finally, constrains the Higgs mass from below [27]. The search will possibly be extended up to Higgs masses of $\sim 115$ GeV.

In the MSSM, the Higgs sector at tree level is completely described by the electroweak parameters and two additional parameters $M_A$ and $\tan\beta$, so that an upper bound for the light scalar Higgs mass can be derived, cf. (2.48).

The crucial test for the existence of the Higgs particles will be their experimental discovery. In this chapter an overview will be presented over the SM and the MSSM Higgs boson search strategies at $pp$ colliders and at $e^+e^-$ linear colliders. Subsequently, the heavy MSSM Higgs particle production in the Compton mode of an $e^+e^-$ linear collider will be examined in detail taking into account the background reactions and interference effects. These processes are important for the search of heavy MSSM Higgs particles in parameter regions that are difficult to exploit at the LHC and in $e^+e^-$ collisions.

## 3.1 Higgs boson search at $pp$ colliders

### 3.1.1 Standard Model Higgs boson

A primary goal of the Large Hadron Collider LHC will be the search for Higgs particles. The main production mechanisms for the SM Higgs boson are [3, 28, 29]

$$\begin{array}{lll} \text{gluon fusion} & : & pp \to gg \to H \\ \text{vector-boson fusion} & : & qq \to qqV^*V^* \to qqH \\ \text{Higgs-strahlung} & : & q\bar{q} \to V^* \to VH \\ \text{associated production with } t\bar{t}/b\bar{b} & : & q\bar{q}, gg \to Ht\bar{t}/b\bar{b} \end{array} \qquad (3.1)$$

where $V = W, Z$. The cross sections are shown in Fig. 3.1 for a center of mass energy of $\sqrt{s} = 14$ TeV. Evidently, the gluon fusion process is the dominant process in the entire mass range up to 1 TeV apart from vector boson fusion which is of the same order of magnitude above 800 GeV. For Higgs masses less than about 100 GeV Higgs-strahlung and associated production with $t\bar{t}$ become competitive with vector boson fusion and provide additional production mechanisms for the Higgs boson.

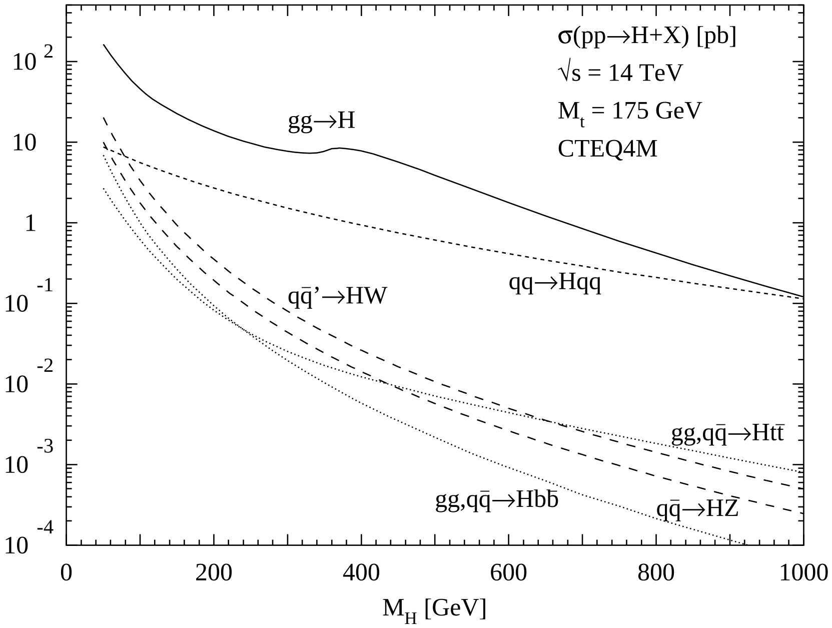

Figure 3.1: *Higgs production cross sections at the LHC for $\sqrt{s} = 14$ TeV as a function of the Higgs mass. The full QCD corrections have been included apart from the processes $Hb\bar{b}$, $Ht\bar{t}$ where the QCD-corrected results are unknown [29].*

The Higgs search strategies will depend on the mass of the Higgs boson. Figs. 3.2 and 3.3 show the significances in the various search channels of the SM Higgs boson in the ATLAS and the CMS experiment, respectively, as a function of the Higgs mass [9, 30]. Evidently, at the LHC several channels are available for the detection of a Higgs boson with a mass between 95 GeV and 1 TeV.

For masses below $\sim 110$ GeV the Higgs boson produced in association with a $t\bar{t}$ pair may be detected in its $b\bar{b}$ decay channel. Since the process is faced with a huge QCD background,

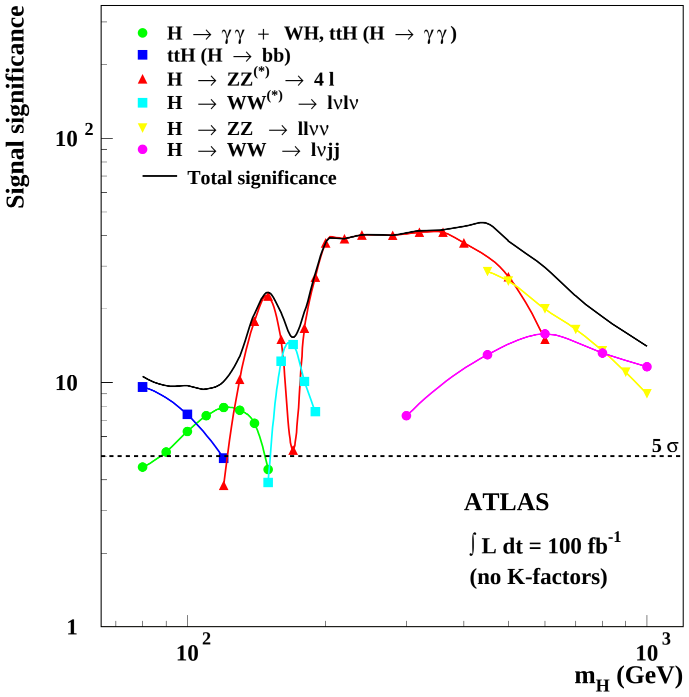

Figure 3.2: *Expected significances in the various SM Higgs search channels at ATLAS as a function of the Higgs mass for an integrated luminosity of 100 fb*$^{-1}$ *[9].*

however, the most promising channel in the mass region $80 \lesssim M_H \lesssim 140$ GeV is the rare decay $H \to \gamma\gamma$ with a branching ratio of $\mathcal{O}(10^{-3})$. The Higgs boson is dominantly produced in gluon fusion. Additional production mechanisms are provided by Higgs radiation off a $W$ boson and associated production of a Higgs boson with $t\bar{t}$.

In the mass range $120 \lesssim M_H \lesssim 800$ GeV, the 'gold-plated' channel $H \to ZZ \to 4l$ is considered to be the most reliable channel for the SM Higgs boson discovery at the LHC. For masses $160 \lesssim M_H \lesssim 180$ GeV where the $ZZ$ branching ratio is only about $\sim 2\%$ the Higgs boson search can be supplemented by the dominant decay $H \to WW$ with $l\nu l\nu$ final states.

If the Higgs mass is large the Higgs boson becomes very broad with a width of up to 600 GeV for $M_H = 1$ TeV. This implies a broad resonance peak in the final state and due to the reduced phase space the event rates decrease for a heavy Higgs boson. Since the channels $H \to ZZ \to l\nu l\nu$ and $H \to WW \to l\nu jj$ involve larger branching ratios than the 'gold-plated' decay they provide a means of detecting the Higgs particle in the range $M_H \gtrsim 800$ GeV.

For an integrated luminosity of 300 fb$^{-1}$, the expected precision for the mass measurement will be 0.1% in the Higgs mass range 80-400 GeV [9, 31].

Fig. 3.4 shows the cross sections for the various Higgs production mechanisms at the Tevatron as a function of the Higgs mass for a c.m. energy of 2 TeV. The most important process for the Higgs search is Higgs-strahlung off $W, Z$ bosons, $q\bar{q} \to W^*/Z^* \to W/Z + H$. Due to the lower luminosity and the large backgrounds at the Tevatron several search channels have to be combined and the statistical power of both experiments CDF and D0 has to be exploited in order to reach significances above three for the detection of the Higgs boson in certain mass windows. For an integrated luminosity of 20 fb$^{-1}$ as might be expected

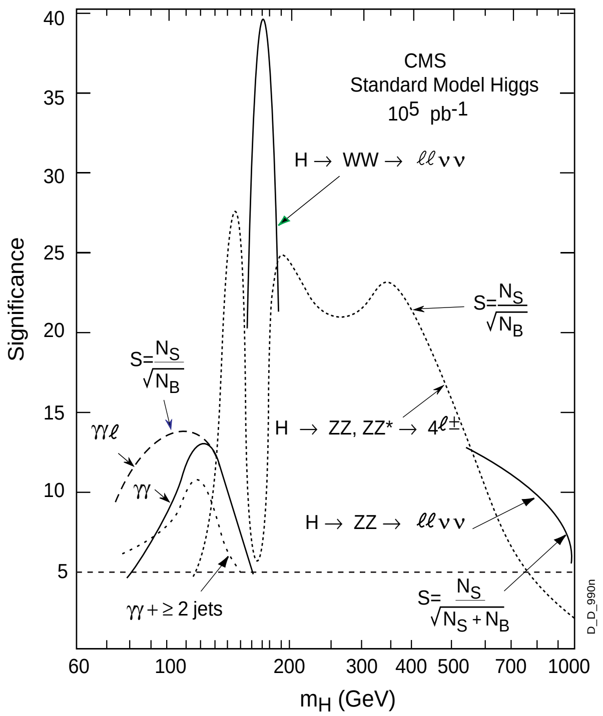

Figure 3.3: *Significances for the SM Higgs boson search as a function of the Higgs mass at CMS for an integrated luminosity of 100 fb*$^{-1}$ *[30].*

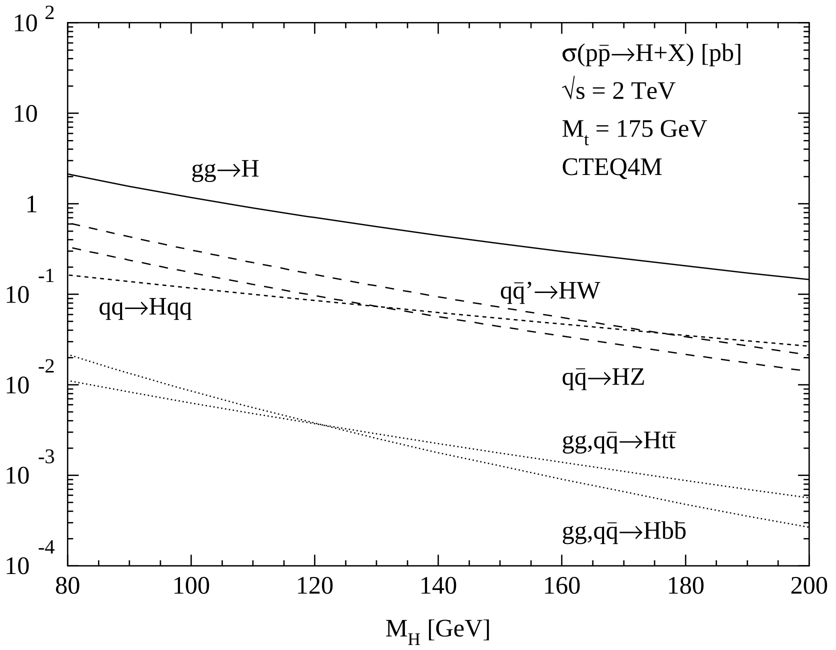

Figure 3.4: *The cross sections of the various Higgs production mechanisms at the Tevatron as a function of the Higgs mass [32]. The plot shows the full QCD corrected results for gluon fusion* $gg \to H$*, vector boson fusion* $qq \to qqVV \to qqH$ *and Higgs-strahlung* $q\bar{q} \to V^* \to VH$*. The QCD corrections to the associated production processes* $gg, q\bar{q} \to Ht\bar{t}, Hb\bar{b}$ *are unknown and therefore not included.*

in RUNIIb a Higgs boson with mass up to $\sim$ 180 GeV can be detected at the $3\sigma$ level using neural network selection for the investigated channels. A $5\sigma$ discovery will only be possible below $\sim$ 120 GeV. The Higgs can be excluded up to $\sim$ 190 GeV with 95% CL [33].

### 3.1.2 Supersymmetric extension

Except for vector boson fusion and Higgs-strahlung the production of the MSSM Higgs bosons proceeds via the same mechanisms as in the SM case taking into account that contributions due to $b$-quarks may also play a rôle for large $\tan\beta$ where the Yukawa couplings to down-type quarks are enhanced, cf. Table 2.1 and Fig. 2.1. The production via vector boson fusion and Higgs-strahlung is only possible for CP-even Higgs bosons since the CP-odd boson $A$ does not interact with the the vector particles at tree level.

In the MSSM the gluon fusion process proceeds dominantly via top- and bottom-quark loops with the $b$-quark contribution becoming of the same size as that due to the top-quark for large $\tan\beta$. Squarks are also involved. However, for large squark masses they decouple. Since the scalar Higgs vector boson couplings are suppressed with $\sin(\beta-\alpha), \cos(\beta-\alpha)$ compared to the corresponding SM couplings the production cross sections for the MSSM scalar Higgs bosons in vector boson fusion are smaller than the SM fusion cross sections. Analogously, the associated production with $W/Z$ is smaller than in the SM case and has only to be considered for the light CP-even Higgs boson and the heavier one provided its mass is small. As can be inferred from Table 2.1 and Fig. 2.1 the MSSM Higgs $t\bar{t}$ couplings are below the SM counterpart for $\tan\beta > 1$ so that associated production with $t\bar{t}$ will always yield smaller cross sections than in the SM. Yet, the same process involving a $b\bar{b}$ pair may become dominant in the large $\tan\beta$ region.

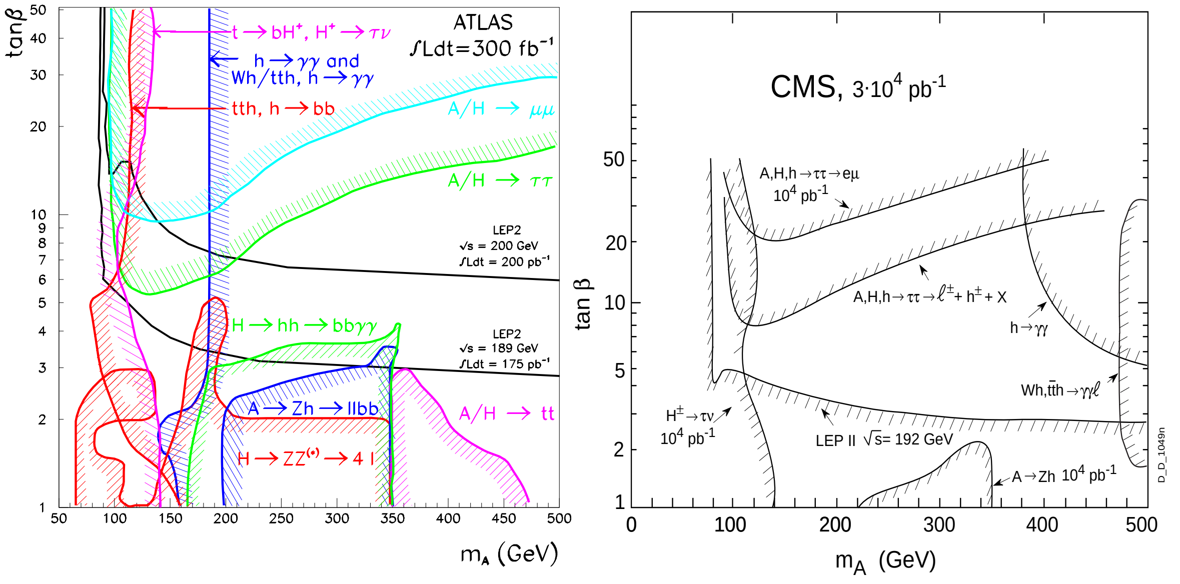

Figure 3.5: *Left: Expected discovery contours for MSSM Higgs bosons at ATLAS with* $\int\mathcal{L} = 300\ fb^{-1}$. *Each curve indicates the sensitivity for different Higgs search modes [9]. Right: CMS 5* $\sigma$ *significance contour plot in the* $M_A - \tan\beta$ *plane [30].*

The search for MSSM Higgs bosons is more complex than in the SM. Fig. 3.5 shows the discovery contours for SUSY Higgs particles at the ATLAS and CMS experiment, respectively. Referring to the ATLAS experiment [the overall picture is essentially the same for the CMS experiment, cf. Fig. 3.5], the basic features can be summarized as follows: Taking into account the exclusion limits set by LEP2 at a c.m. energy of 200 GeV, the light Higgs state $h$ produced in association with $t\bar{t}$ may be found in its $b\bar{b}$ decay channel for pseudoscalar Higgs masses $M_A \gtrsim 110$ GeV. In the mass range $M_A \gtrsim 200$ GeV the CP-even Higgs boson $h$ can be found via the $\gamma\gamma$ decay channel. The heavy Higgs particles $H$ and $A$ can be found in the channel $H/A \to \tau\tau$ for $M_A \gtrsim 100$ GeV and moderate and large values of $\tan\beta$. Since the MSSM Higgs couplings to charged leptons grow with $\tan\beta$, for larger values $\tan\beta \gtrsim 10$ the search channel $H/A \to \mu\mu$ opens in the same $M_A$ region. As the masses for the heavy CP-even and the CP-odd Higgs boson are almost the same in this parameter space it will be very difficult to disentangle the $H$ signal from the pseudoscalar signal. For $M_A \lesssim 140$ GeV, the charged Higgs boson produced in top decays can be searched for in the channel $t \to bH^+$.

The mass of the light CP-even Higgs boson $h$ is expected be determined with a precision of 200 MeV at the LHC [9]. However, the final picture exhibits two difficult regions. For $90 \lesssim M_A \lesssim$ 110 GeV, the light Higgs boson might be seen neither by LEP2 nor by LHC. And for $M_A \gtrsim 200$ GeV and $\tan\beta \gtrsim 6$ up to 15, no heavy neutral Higgs bosons can be discovered so that the distinction between the SM and the MSSM based solely on light scalar Higgs measurements will be difficult. Note also that if neutralinos and charginos are light enough, Higgs decays into these particles are possible and will change the search strategies at the LHC [34].

By appropriate rescaling of the SM results an analysis for the MSSM Higgs boson search has been carried out at the Tevatron [33]. The analysed production channels for the scalar Higgs particles are Higgs-strahlung with subsequent decay into $b\bar{b}$ and associated production with $b\bar{b}$ for all neutral MSSM Higgs particles. The results for the exclusion regions at 95% CL and the $5\sigma$ discovery regions depend on the chosen set of SUSY parameters. For example, in the case of maximal mixing a light scalar Higgs with mass $\lesssim 130$ GeV can be discovered at the $5\sigma$ level in almost the whole $M_A - \tan\beta$ plane if an integrated luminosity of 30 fb$^{-1}$ can be achieved. Difficult regions are the low $M_A$ region for moderate and large values of $\tan\beta$. A detailed prescription of the analysis can be found in [33, 35].

## 3.2 Higgs boson search at $e^+e^-$ colliders

$e^+e^-$ linear colliders operating in the c.m. energy range between 500 GeV and 1 TeV are ideal instruments for the search of Higgs bosons with masses in the intermediate mass range. In this section the Higgs boson search at these future colliders will be reviewed.

### 3.2.1 Standard Model

The main production mechanisms for a SM Higgs boson at an $e^+e^-$ collider in the energy range 500 GeV$\le \sqrt{s} \le 1$ TeV are the processes

$$\begin{array}{ll} \text{Higgs-strahlung:} & e^+e^- \to (Z) \to Z + H \\ \text{WW fusion} \quad : & e^+e^- \to \bar{\nu}\nu(WW) \to \bar{\nu}\nu + H \end{array} \tag{3.2}$$

For moderate values of the Higgs mass and in the low energy range Higgs-strahlung is the main production process [36, 37]. Beyond the threshold region the cross section decreases

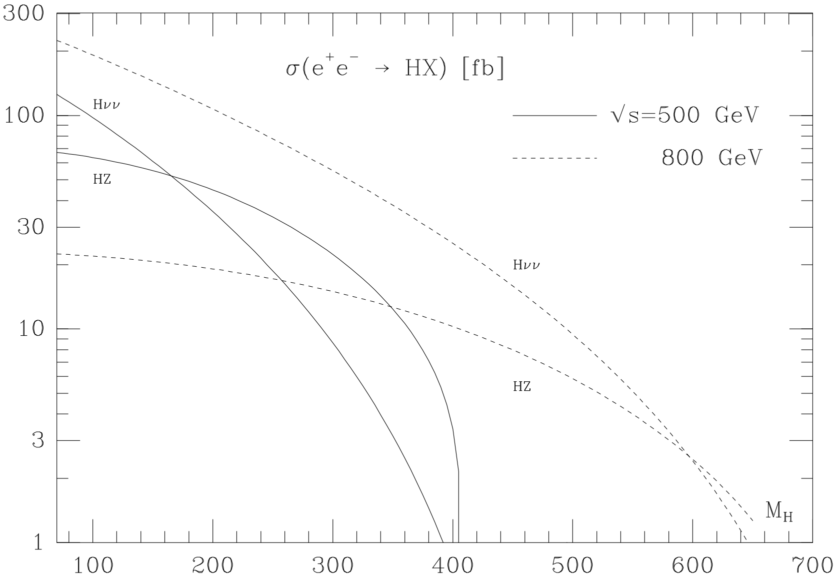

Figure 3.6: *The cross sections of Higgs-strahlung* $e^+e^- \to ZH$ *and* $WW/ZZ$ *fusion* $e^+e^- \to \bar{\nu}\nu/e^+e^-H$ *for two collider energies* $\sqrt{s} = 500$ *GeV (solid) and* $\sqrt{s} = 800$ *GeV (dashed), [10].*

proportional $s^{-1}$ with the maximum being reached rather close to the threshold. For larger energies $WW$ fusion starts playing a rôle [38–41] since in the high-energy limit, $M_H^2/s$ and $M_W^2/s \ll 1$, the cross section increases with $\log s$. Another production mechanism is provided by $ZZ$ fusion. Due to the small $Ze^+e^-$ couplings this process is suppressed by an order of magnitude compared to $WW$ fusion. Yet, the $Z$ decay yields two leptons in the final state so that by reconstructing the recoil mass a sufficiently large signal to background ratio can be achieved.

In Fig. 3.6 the cross sections of $WW$ boson fusion and Higgs-strahlung are shown for two typical collider energies, $\sqrt{s} = 500$ GeV and 800 GeV [10]. Apparently, $WW$ fusion is the dominant process for higher energies. The cross sections are $\mathcal{O}$(1-100) fb yielding up to $10^5$ events in the intermediate mass range for the foreseen integrated luminosity of 500 fb$^{-1}$ in the low-energy phase.

Due to the definite energy $E_Z$ of the recoiling $Z$ boson in the Higgs-strahlung process the Higgs mass can be determined via the relation $M_H^2 = s - 2\sqrt{s}E_Z + M_Z^2$. The Higgs boson search will be independent from the decay channel and the signal will only slightly be modified when detector properties are taken into account [42]. Also in $WW$ fusion it will be no problem to find the Higgs boson since the main background $e^+e^- \to (e^+)\nu_e W^-$ with the positron in the final state escaping detection is small. The mass of the SM Higgs particle can be determined at $e^+e^-$ colliders very precisely by exploiting the kinematic constraints in the leptonic channels of Higgs-strahlung events. For an integrated luminosity of 500 fb$^{-1}$ and a c.m. energy of 350 GeV, a precision of $\sim$ 150 MeV can be reached for Higgs masses between 120 and 160 GeV independent of the Higgs decay mode [43]. The discovery limit is given by $M_H \lesssim 0.7\sqrt{s}$. $e^+e^-$ linear colliders are therefore optimal machines for the detection of Higgs bosons in the intermediate mass range $M_H \lesssim 2M_Z$.

### 3.2.2 SUSY Higgs particles

Higgs-strahlung, Higgs pair production and vector boson fusion are the dominant production mechanisms for neutral MSSM Higgs bosons at $e^+e^-$ colliders [6, 44, 45]:

$$\begin{array}{lll} \text{Higgs-strahlung} & : & e^+e^- \to (Z) \to Z + h/H \\ \text{Pair production} & : & e^+e^- \to (Z) \to A + h/H \\ WW \text{ fusion} & : & e^+e^- \to \bar{\nu}\nu(WW) \to \bar{\nu}\nu + h/H \\ ZZ \text{ fusion} & : & e^+e^- \to e^+e^-(ZZ) \to e^+e^- + h/H \end{array} \tag{3.3}$$

The cross sections for Higgs-strahlung and pair production can be cast into the form

$$\begin{aligned} \sigma(e^+e^- \to Zh/H) &= \sin^2/\cos^2(\beta-\alpha)\sigma_{SM} \\ \sigma(e^+e^- \to Ah/H) &= \cos^2/\sin^2(\beta-\alpha)\sigma_{SM}\bar{\lambda} \end{aligned} \tag{3.4}$$

where $\sigma_{SM}$ denotes the SM cross section for Higgs-strahlung and $\bar{\lambda} \sim \lambda_{Aj}^{3/2}/\lambda_{Zj}^{1/2}$ ($\lambda_{ij}$ is the Källen function for particles with masses $M_i$ and $M_j$) results from the P-wave suppression near the threshold.

The cross sections for $h, H$ production via Higgs-strahlung and pair production are among themselves and mutually complementary to each other being proportional either to $\sin^2(\beta-\alpha)$ or $\cos^2(\beta-\alpha)$. Since $\sigma_{SM}$ is large, at least the light CP-even Higgs boson should be found: If $\sin^2(\beta-\alpha)$ is small, also $M_A$ is small, and $h$ can then be detected in associated production with a light $A$.

The upper plot in Fig. 3.7 shows representative examples of the cross sections for the production of neutral Higgs bosons as a function of the Higgs masses for $\tan\beta = 3$ and 30. In the decoupling limit where $\sin(\beta-\alpha) \to 1$ the $hZ$ cross section becomes maximal being of $\mathcal{O}(60\text{ fb})$. In contrast, the $HZ$ cross section is large at the lower end of the mass range. The signal signature, also for $HZ$ in most of the parameter space, involves a $Z$ boson and a $b\bar{b}$ or $\tau^+\tau^-$ pair. Since the process $Ah$ grows with $\cos^2(\beta-\alpha)$ it increases towards lower $M_h$ masses where $\cos(\beta-\alpha)$ approaches its maximum absolute value. The complementary process $AH$ is preferred for large $M_H$. The signature will in both cases include four $b$ quarks in most of the parameter space so that a good $b$-tagging performance will be required in order to separate the signal from the background due to QCD jets and $Z$ boson pair production.

For small Higgs masses (below $\sim$ 160 GeV for $\sqrt{s} = 500$ GeV) $WW$ fusion dominates over Higgs-strahlung [28]. Yet, it involves neutrinos in the final state thus rendering the extraction of the signal more difficult. On the other hand the leptonic final states of $ZZ$ fusion allow for the full signal reconstruction although it is an order of magnitude smaller than the $WW$ fusion process.

The lower plot in Fig. 3.7 shows the production cross sections for charged Higgs bosons as a function of the Higgs mass for $\tan\beta = 3$ and 30. If kinematically allowed they are produced via top-decays, $t \to b + H^+$. For $\tan\beta > 1$, charged Higgs bosons decay into $\tau\nu_\tau$ so that lepton universality will be broken in the final state, since $\tau$ states dominate over $e, \mu$ final states in $t$ decays. For large masses $M_{H^\pm}$ the bosons have to be pair-produced in $e^+e^-$ collisions, $e^+e^- \to H^+H^-$. The cross section which only depends on $M_{H^\pm}$ decreases fast due to $P$-wave suppression $\sim \beta^3$ near the threshold. $\gamma\gamma$ collisions, however, yield larger cross sections.

The preceding discussion has shown that the light CP-even Higgs boson will not escape detection at linear colliders. Its mass may be determined with an accuracy of 50 MeV [46].

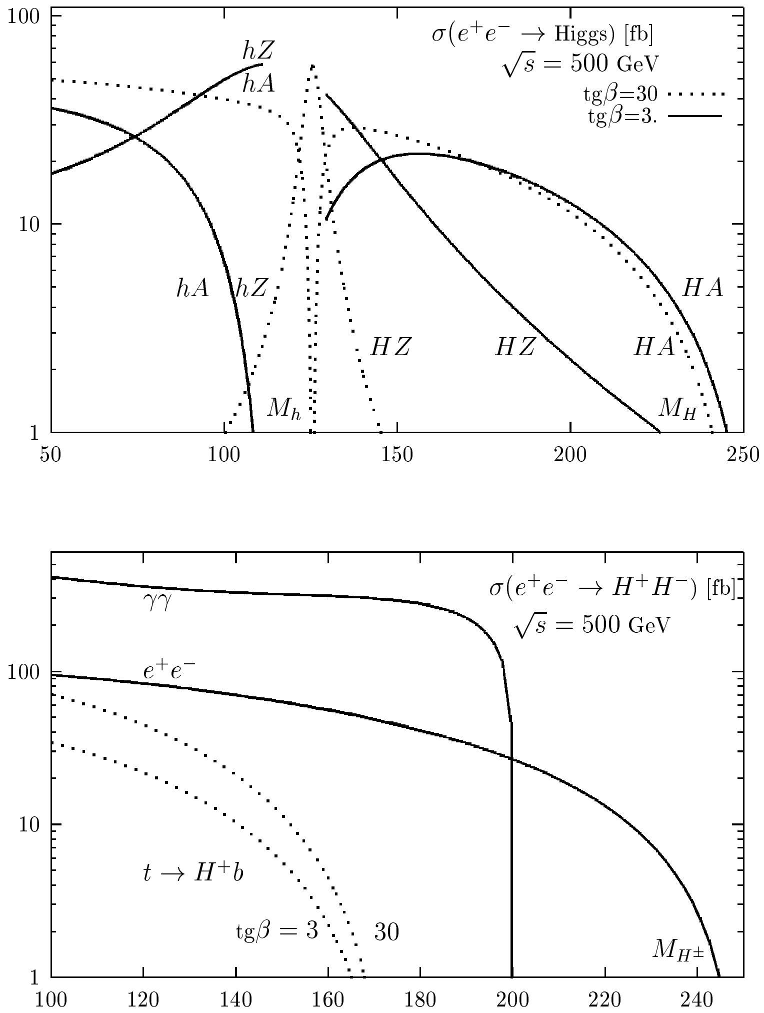

Figure 3.7: *Upper plot: Production cross sections of MSSM Higgs bosons at* $\sqrt{s} = 500$ *GeV. Lower plot: Charged Higgs boson production for* $\sqrt{s} = 500$ *GeV – courtesy of A. Djouadi.*

Furthermore, all MSSM Higgs particles can be discovered in the mass range $M_H, M_A \lesssim 1/2\sqrt{s}$, independent of the value of $\tan\beta$ [10].

## 3.3 Heavy MSSM Higgs production in $\gamma\gamma$ collisions

According to the present analyses neutral heavy MSSM Higgs bosons, $A$ and $H$, with masses $M_{A/H} \gtrsim 200$ GeV may escape detection at the LHC for moderate values of $\tan\beta$. In addition, in $e^+e^-$ collisions at linear colliders the discovery of all MSSM Higgs particles with mass $M$ independently of $\tan\beta$ requires a c.m. energy $\sqrt{s} \gtrsim 2M$ [10], hence $\sqrt{s} \gtrsim 1.6$ TeV for $M_{A/H} = 800$ GeV. Since the photons produced from Compton scattered laser light off energetic electron/positron beams have approximately the same energy as the initial beams and high luminosity [12], Higgs production in $\gamma\gamma$ collisions provides an additional powerful mechanism that can be used for the Higgs boson search.

In this section the heavy MSSM Higgs production via $\gamma\gamma$ fusion at a high-luminosity $e^+e^-$ linear collider will be analysed. The branching ratios of the $A$ and $H$ decay modes that will be exploited for this task are illustrated in Fig. 3.8 as a function of the corresponding Higgs

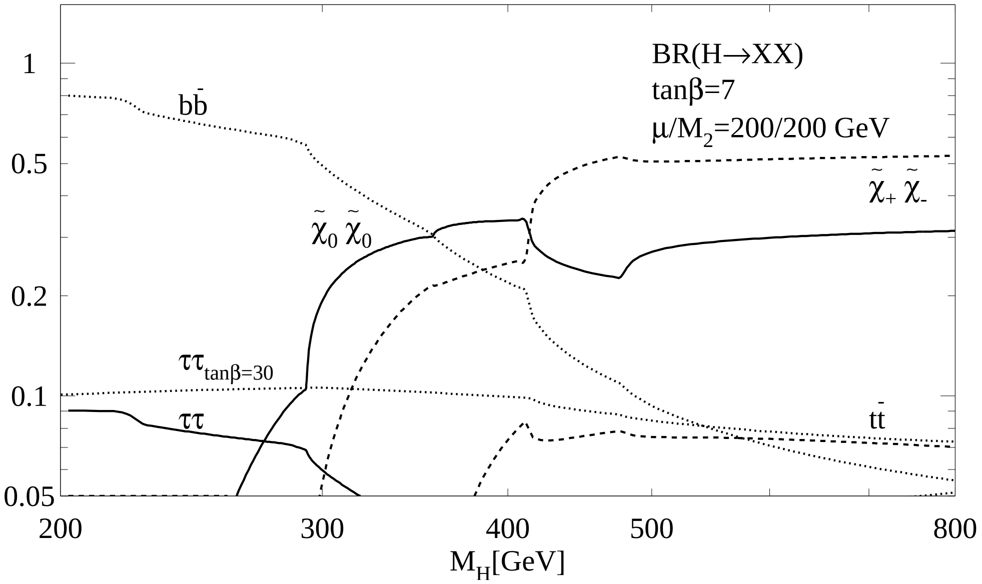

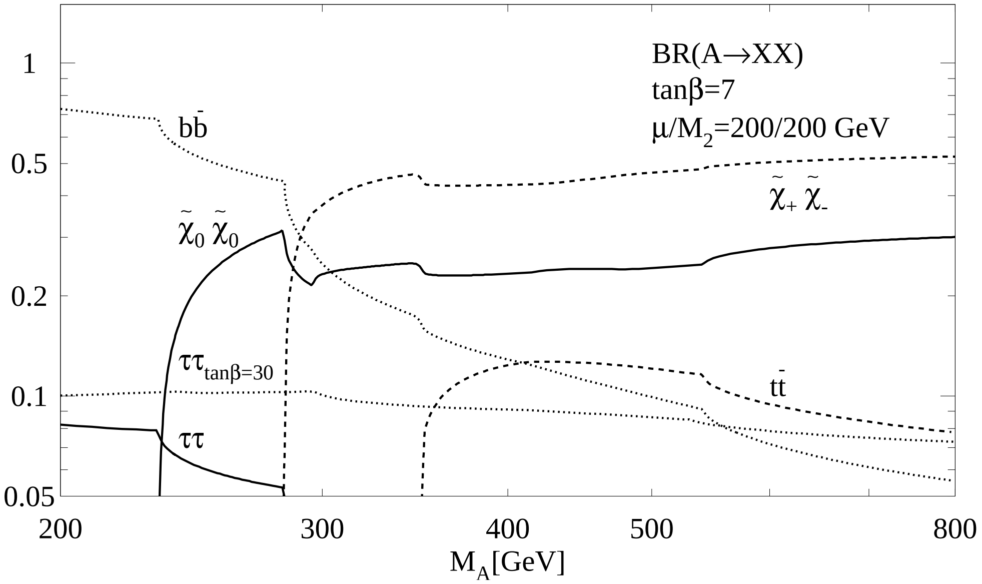

Figure 3.8: *The branching ratios of the heavy MSSM Higgs bosons $H$ and $A$ into charginos and neutralinos, bottom and top quarks and $\tau^+\tau^-$. The visible SUSY final states have been summed up, i.e. $\tilde{\chi}^+\tilde{\chi}^- = \sum_{i,j=1,2}\tilde{\chi}_i^+\tilde{\chi}_j^-$ and $\tilde{\chi}^0\tilde{\chi}^0 = \sum_{i,j=1..4}\tilde{\chi}_i^0\tilde{\chi}_j^0 - \tilde{\chi}_1^0\tilde{\chi}_1^0$, assuming that the lightest neutralino $\tilde{\chi}_1^0$ is the LSP which cannot be observed. The SUSY parameters $\mu$ and $M_2$ have been chosen equal to 200 GeV and* $\tan\beta = 7$. *(The branching fraction $BR(H/A \to \tau^+\tau^-)$ is also shown for* $\tan\beta = 30$.*) The SUSY breaking squark and slepton masses have been set equal to 1 TeV and the SUSY breaking trilinear couplings are zero.*

mass in the range 200...800 GeV. The higgsino mixing parameter is chosen $\mu = 200$ GeV, the universal gaugino mass parameter $M_2 = 200$ GeV and $\tan\beta = 7$. The SUSY breaking sfermion masses are chosen as 1 TeV and the SUSY breaking trilinear couplings are set equal to 0. This will be the SUSY parameter set used in the following if not stated otherwise. In the lower mass range $H$ and $A$ preferentially decay into $b\bar{b}$ whereas in the upper mass range, beyond the corresponding kinematic thresholds, the chargino decays dominate followed by the neutralino channels. Above the $t\bar{t}$ threshold the branching ratio into top quarks amounts up to $\sim 13\%$. At the lower end of the mass range the $\tau^+\tau^-$ branching ratio may reach $\sim 10\%$.

**$b\bar{b}$ production**

The signal process $\gamma\gamma \to$ Higgs $\to b\bar{b}$ is confronted with the background reaction $\gamma\gamma \to b\bar{b}$. In order to suppress the background with respect to the signal it is helpful to use polarized photons. The spin-0 Higgs particles are only produced from an initial state with the third component of the angular momentum $J_z = 0$. The $J_z = 0$ background process, however, is suppressed by $m_b^2/s$ in leading order [47–52]. The channel $\gamma\gamma \to b\bar{b}$ hence provides an outstanding signature for the heavy MSSM Higgs boson search. The signal process proceeding via massive $s$-channel Higgs bosons dominantly develops a 2–jet topology in the final state whereas the next-to-leading order (NLO) background process favours the 3-jet topology due to the leading order (LO) suppression $m_b^2/s$ for $J_z = 0$. In the case of the light $b$-quarks the subsequent analysis will therefore investigate the two-jet final state. Next-to-leading order calculations have shown that the $m_b^2/s$ suppression is removed by gluon brems-strahlung [48–52]. The significance of the 2-jet signal topology can therefore be spoiled by the radiatively corrected background process if partons are collinear or one of the partons is rather soft thus faking a 2-jet final state. This background has to be suppressed by applying stringent cuts. The two-jet configuration due to soft or collinear partons involves large double logarithms [49–52]. In order to properly take into account higher order corrections the logarithms have to be resummed leading to the well-known Sudakov form factor [53] denoted by $\mathcal{F}_g$ which corresponds to the emission of soft real and the exchange of soft virtual gluons and a non-Sudakov form factor $\mathcal{F}_q$ related to soft virtual quark contributions [51, 52].

The subsequent analysis will investigate heavy MSSM Higgs production in

$$e^+e^- \to \gamma\gamma \to A/H \to b\bar{b} \tag{3.5}$$

for polarized electron/positron and photon beams. The discovery reach in the Higgs mass range $M_{A/H} = 200...800$ GeV for moderate $\tan\beta = 7$ is analysed by including the background and the interference process in the two-jet topology. Radiative corrections are thoroughly incorporated considering the QCD corrections to signal [54–59], background [49, 50] and also to the interference process, calculated in this thesis for the first time. The leading higher-order QCD corrections which are sizeable in the two-jet configuration are considered through the resummation of the Sudakov and non-Sudakov double logarithms [51, 52].

**The $t\bar{t}$ and $\tau^+\tau^-$ channel**

As further options Higgs detection in

$$e^+e^- \to \gamma\gamma \to A/H \to t\bar{t} \quad \text{and} \quad \tau^+\tau^- \tag{3.6}$$

is investigated. In contrast to the top-quark final state the $\tau^+\tau^-$ production does not acquire final state QCD corrections. The $\tau^+\tau^-$ process will be analysed for the two $\tan\beta$ values 7 and 30. Since the Yukawa couplings of $A$ and $H$ to $\tau^+\tau^-$ increase with rising $\tan\beta$, thus enhancing the corresponding branching fractions, the signal cross section will grow with $\tan\beta$ while the background process is independent of $\tan\beta$.

**Chargino and neutralino production**
Since the branching ratios of the chargino and neutralino channels are rather large the processes

$$\begin{array}{lcll} e^+e^- \to \gamma\gamma & \to & A/H \to \tilde{\chi}_i^+\tilde{\chi}_j^- \ , & (i,j=1,2) \\ e^+e^- \to \gamma\gamma & \to & A/H \to \tilde{\chi}_i^0\tilde{\chi}_j^0 \ , & (i,j=1,...,4;\ \text{not}\ i=j=1) \end{array} \tag{3.7}$$

may provide additional interesting detection channels. The SUSY particle pair production cross sections are summed over all possible final states excluding however the production of $\tilde{\chi}_1^0\tilde{\chi}_1^0$ where $\tilde{\chi}_1^0$ denotes the lightest neutralino. This is due to the assumption that $\tilde{\chi}_1^0$ is the lightest supersymmetric particle (LSP). Because of R-parity conservation it cannot decay and the $\tilde{\chi}_1^0\tilde{\chi}_1^0$ state will escape detection. As in the case of lepton production the SUSY processes do not involve final state QCD corrections.

### 3.3.1 The quark final states

**1.) Signal process**
The signal process $\gamma\gamma \to q\bar{q}$ proceeds via the MSSM Higgs bosons $h, H$ and $A$. Fig. 3.9 shows the generic diagrams contributing to the process at LO and at NLO. The two photons are coupled to the Higgs bosons through triangle loops including heavy charged fermions, charginos and in the case of CP-even Higgs bosons also $W$ bosons and charged Higgs bosons as well as sfermions. $A$ does neither couple to gauge bosons at tree level, cf. Tab. 2.1, nor to charged Higgs particles, cf. Tab. 3.1. Furthermore $A$ flips the sfermion helicity whereas it is conserved in the coupling to the photon so that sfermion loops do not contribute to the $\gamma\gamma A$ coupling. The effective $\gamma\gamma h/H$ coupling for incoming photons $k_1^\mu$, $k_2^\nu$ is given by [60, 61]

$$\frac{i\alpha\sqrt{\sqrt{2}G_F}}{2\pi}\mathcal{M}_\varphi[k_1^\nu k_2^\mu - k_1k_2g_{\mu\nu}]\ , \quad \varphi = h, H \tag{3.8}$$

with the form factor [29]

$$\begin{aligned} \mathcal{M}_\varphi &= \sum_f N_c^f Q_f^2 g_{\varphi ff} A_f^\varphi(\tau_f) + g_{\varphi WW} A_W^\varphi(\tau_W) + g_{\varphi H^+H^-} A_{H^\pm}^\varphi(\tau_{H^\pm}) \\ &+ \sum_{\tilde{\chi}^\pm} \frac{2M_W}{M_{\tilde{\chi}_i^\pm}} g_{\varphi\tilde{\chi}_i^+\tilde{\chi}_i^-} A_{\tilde{\chi}^\pm}^\varphi(\tau_{\tilde{\chi}^\pm}) + \sum_{\tilde{f}} N_c^f Q_{\tilde{f}}^2 g_{\varphi\tilde{f}\tilde{f}} A_{\tilde{f}}^\varphi(\tau_{\tilde{f}}) \end{aligned} \tag{3.9}$$

and

$$\begin{aligned} A_{f/\tilde{\chi}^\pm}^\varphi(\tau) &= 2\tau[1+(1-\tau)f(\tau)] \\ A_{H^\pm/\tilde{f}}^\varphi(\tau) &= -\tau[1-\tau f(\tau)] \\ A_W^\varphi(\tau) &= -[2+3\tau+3\tau(2-\tau)f(\tau)] \end{aligned} \tag{3.10}$$

The parameter $\tau_x$ is defined as $\tau_x = 4M_x^2/M^2$ and the function $f(\tau)$ is given by

$$f(\tau) = \begin{cases} \arcsin^2 \frac{1}{\sqrt{\tau}} & \tau \geq 1 \\ -\frac{1}{4}\left[\log\frac{1+\sqrt{1-\tau}}{1-\sqrt{1-\tau}} - i\pi\right]^2 & \tau < 1 \end{cases} \tag{3.11}$$

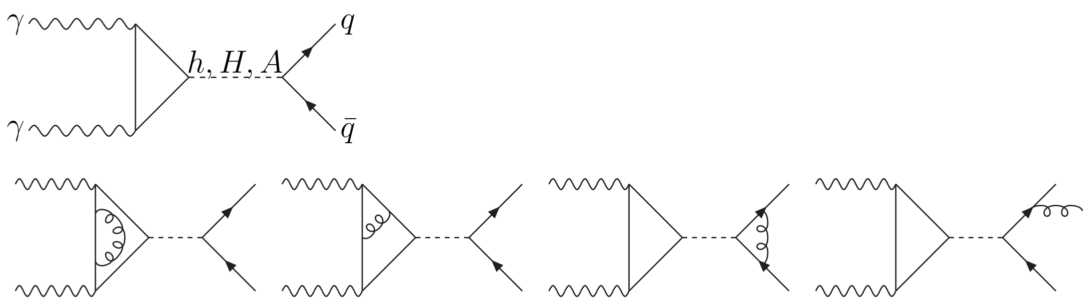

Figure 3.9: *Generic diagrams contributing to the signal process $\gamma\gamma \to h, H, A \to q\bar{q}$ at leading and next-to-leading order.*

In the cross sections given below, $M^2$ in the parameter $\tau$ is equal to the c.m. energy of the process. The couplings $g_{\varphi xx}$ are given in Tabs. 2.1 and 3.1. $N_c^f$ denotes the colour factor of the corresponding fermion $f$ and $Q_{f(\tilde{f})}$ the electric fermion (sfermion) charges in units of the positron charge. The effective coupling $\gamma\gamma A$ can be cast into the form [60, 61]

$$\frac{i\alpha\sqrt{\sqrt{2}G_F}}{2\pi}\mathcal{M}_A\epsilon_{\mu\nu\alpha\beta}k_1^\alpha k_2^\beta \tag{3.12}$$

where the form factor $\mathcal{M}_A$ is given by [29]

$$\mathcal{M}_A = \sum_f N_c^f Q_f^2 g_{Aff} A_f^A(\tau_f) + \sum_{\tilde{\chi}^\pm} \frac{2M_W}{M_{\tilde{\chi}_i^\pm}} g_{A\tilde{\chi}_i^+\tilde{\chi}_i^-} A_{\tilde{\chi}^\pm}^A(\tau_{\tilde{\chi}^\pm}) \tag{3.13}$$

with

$$A^A_{f/\tilde{\chi}^\pm}(\tau) \;=\; 2\tau f(\tau) \tag{3.14}$$

After integration over $|\cos\theta| < c$, where $\theta$ denotes the scattering angle between the quark and the direction of the incoming photons in the c.m. frame, the polarized LO signal cross sections, labeled by the index $S$, are given by

$$\begin{aligned}
\sigma_{S,q\bar{q}}^{++/--} &= \frac{N_c G_F^2 \alpha^2 \beta m_q^2 c}{64\pi^3} \\
&\times \left[g_{hqq}^2\beta^2|\mathcal{G}_h|^2 + g_{Hqq}^2\beta^2|\mathcal{G}_H|^2 + g_{Aqq}^2|\mathcal{G}_A|^2 + 2g_{hqq}g_{Hqq}\beta^2\mathrm{Re}(\mathcal{G}_h\mathcal{G}_H^*)\right] \\
\sigma_{S,q\bar{q}}^{+-/-+} &= 0
\end{aligned} \tag{3.15}$$

The generalized form factor $\mathcal{G}_\Phi$ ($\Phi = h, H, A$) is defined as

$$\mathcal{G}_\Phi \equiv \frac{\mathcal{M}_\Phi}{1 - \mu_\Phi + i\gamma_\Phi} \tag{3.16}$$

with the reduced mass $\mu_\Phi = M_\Phi^2/s$ and the reduced width $\gamma_\Phi = [M_\Phi\Gamma_\Phi]/s$ where $\Gamma_\Phi$ denotes the total width. The velocity $\beta$ is given by $\beta = (1 - 4m_q^2/s)^{1/2}$. Obviously, since the Higgs bosons carry spin 0, the $J_z = \pm 2$ cross sections vanish.

The generic diagrams contributing to the NLO processes, cf. Fig. 3.9, involve the QCD corrections to the quark and squark loops in the $\gamma\gamma\Phi$ form factor due to virtual gluon exchange. For the $t$ and $b$ loops the QCD corrections are known for finite quark and Higgs masses [55, 56] whereas for squark loops they have only been calculated in the large squark

| $\Phi$ | | $g_{\Phi H^+ H^-}$ | $g_{\Phi \tilde{\chi}_i^+ \tilde{\chi}_j^-}$ |
|---|---|---|---|
| $SM$ | $H$ | $0$ | $0$ |
| $MSSM$ | $h$ | $\frac{M_W^2}{M_{H^\pm}^2}\left[\sin(\beta-\alpha)+\frac{\cos 2\beta \sin(\beta+\alpha)}{2\cos^2\theta_W}\right]$ | $S_{ij}\cos\alpha - Q_{ij}\sin\alpha$ |
| | $H$ | $\frac{M_W^2}{M_{H^\pm}^2}\left[\cos(\beta-\alpha)-\frac{\cos 2\beta \cos(\beta+\alpha)}{2\cos^2\theta_W}\right]$ | $S_{ij}\sin\alpha + Q_{ij}\cos\alpha$ |
| | $A$ | $0$ | $-S_{ij}\cos\beta - Q_{ij}\sin\beta$ |

| $\Phi$ | | $g_{\Phi \tilde{f}_{L/R} \tilde{f}_{L/R}}$ | $g_{\Phi \tilde{\chi}_i^0 \tilde{\chi}_j^0}$ |
|---|---|---|---|
| $SM$ | $H$ | $0$ | $0$ |
| $MSSM$ | $h$ | $\frac{M_f^2}{M_{\tilde{f}}^2} g_{hff} \mp \frac{M_Z^2}{M_{\tilde{f}}^2}(I_3^f - Q_f \sin^2\theta_W)\sin(\beta+\alpha)$ | $-Q''_{ij}\sin\alpha - S''_{ij}\cos\alpha$ |
| | $H$ | $\frac{M_f^2}{M_{\tilde{f}}^2} g_{Hff} \pm \frac{M_Z^2}{M_{\tilde{f}}^2}(I_3^f - Q_f \sin^2\theta_W)\cos(\beta+\alpha)$ | $Q''_{ij}\cos\alpha - S''_{ij}\sin\alpha$ |
| | $A$ | $0$ | $-Q''_{ij}\sin\beta + S''_{ij}\cos\beta$ |

Table 3.1: *MSSM Higgs boson couplings to charged Higgs bosons, charginos, sfermions and neutralinos.* $Q_{ij}$ *and* $S_{ij}$ $(i/j = 1, 2)$ *are related to the mixing angles in the chargino sector,* $Q''_{ij}$ *and* $S''_{ij}$ $(i/j = 1, .., 4)$ *to those in the neutralino sector, cf. Refs. [3, 5, 6].* $I_3^f$ *denotes the third isospin component.*

mass limit [57]. In order to improve the perturbative behaviour of the quark loop contributions, the QCD corrections are expressed in terms of the running on-shell masses $m_{on}(\mu)$. The scale $\mu$ has been identified with $\mu = \sqrt{s}/2$. The running mass is normalized to the pole mass $m_q$ via

$$m_{on}(\mu = m_q) = m_q \tag{3.17}$$

This definition of the running mass allows to properly take into account threshold effects at $\sqrt{s} = 2m_q$. In contrast, the definition of the running $\overline{\mathrm{MS}}$ mass

$$m_q = \overline{m}_q(\mu)\left[1 + \frac{\alpha_s}{\pi}\left(\frac{4}{3} + \ln\frac{\mu^2}{m_q^2}\right)\right] \tag{3.18}$$

leads to an artificial displacement between the running mass and the pole mass at $\mu = m_q$:

$$m_{on}(\mu) = \overline{m}_q(\mu)\left[1 + \frac{4}{3}\frac{\alpha_s(m_q)}{\pi}\right] \tag{3.19}$$

The QCD corrections to the Higgs decay into $q\bar{q}$ involving virtual gluon exchange and real gluon radiation have been calculated, too, [58, 59]. The arising large logarithmic contributions are absorbed in the running $\overline{\mathrm{MS}}$ mass $\overline{m}_q(\mu)$ at the scale $\mu = \sqrt{s}$. The full MSSM electroweak and SUSY-QCD corrections are known [62]. Since they are moderate they have not been implemented. Only the gluino corrections can become large if tan $\beta$ and the higgsino mixing parameter $\mu$ are large [62].

**2.) Background process**

The generic diagrams contributing to the background process $\gamma\gamma \to q\bar{q}$ at Born level and

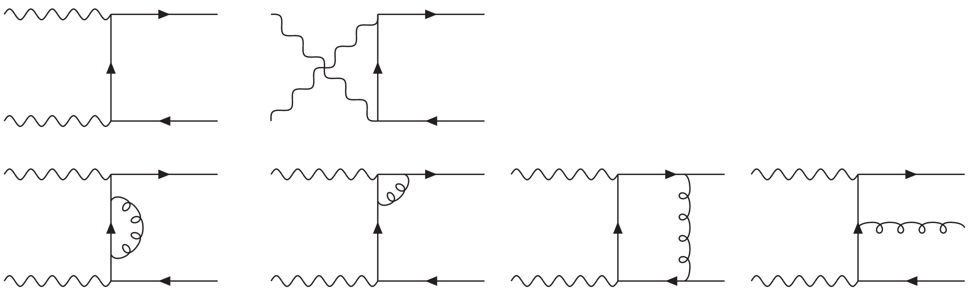

Figure 3.10: *Generic Diagrams contributing to the background process $\gamma\gamma \to q\bar{q}$ at leading and next-to-leading order.*

next-to-leading order are depicted in Fig. 3.10. At leading order the polarized background cross sections after integration over $|\cos\theta| < c$ read

$$\begin{aligned}
\sigma_{B,q\bar{q}}^{++/--} &= \frac{N_c\alpha^2 Q_q^4 2\pi}{s(1-c^2\beta^2)}(1-\beta^4)\left[2\beta c + (1-c^2\beta^2)\ln\frac{1+\beta c}{1-\beta c}\right] && (3.20)\\
\sigma_{B,q\bar{q}}^{+-/-+} &= \frac{N_c\alpha^2 Q_q^4 2\pi}{s(1-c^2\beta^2)}\left[-2c\beta^5 + 8c\beta^3 + 4c^3\beta^3 - 10\beta c + (5-\beta^4)(1-c^2\beta^2)\ln\frac{1+\beta c}{1-\beta c}\right]
\end{aligned}$$

$Q_q$ denotes the electric charge of the quark in units of the positron charge and $\alpha$ the electromagnetic coupling. The NLO 2+3-jet cross section is built up by the virtual corrections involving self-energy contributions, vertex corrections and box diagrams and by the brems-strahlung processes, cf. Fig. 3.10. The virtual cross sections involve UV and IR divergences. The UV singularities are absorbed by the renormalization of the quark mass and the $\gamma q\bar{q}$ vertex. The brems-strahlung process encounters IR singularities which cancel those arising in the virtual cross section. The results for polarized photons are given in Refs. [49, 50].

**3.) Interference contribution**

The polarized interference cross sections between signal and background process in leading order

$$\gamma(k_1) + \gamma(k_2) \to q(p_1) + \bar{q}(p_2) \tag{3.21}$$

are given by

$$\begin{aligned}
\sigma_{I,q\bar{q}}^{++/--} &= -\frac{N_c G_F \alpha^2 Q_q^2 \beta(1-\beta^2)}{4\sqrt{2}\pi}\ln\frac{1+\beta c}{1-\beta c}\\
&\times \left[g_{hqq}\beta\,\mathrm{Re}\,(\mathcal{G}_h) + g_{Hqq}\beta\,\mathrm{Re}\,(\mathcal{G}_H) - \frac{g_{Aqq}}{\beta}\,\mathrm{Re}\,(\mathcal{G}_A)\right]\\
\sigma_{I,q\bar{q}}^{+-/-+} &= 0 && (3.22)
\end{aligned}$$

after integrating out $\cos\theta$ in the interval $[-c, c]$.

**Virtual corrections**

The virtual interference cross section in next-to-leading order is obtained from the interference of the virtual NLO background and the LO signal diagrams and vice versa. The UV and IR singularities which turn up in the loop integrals are treated in dimensional regularization, *i.e.* all cross sections are calculated in $n = 4 - 2\epsilon$ space-time dimensions. The matrix $\gamma_5$ included in the pseudoscalar Higgs-Yukawa coupling has been treated in the 't Hooft/Veltman prescription [63] in $n$ dimensions. After averaging over the photon spins and evaluating the $n$-dimensional two-particle phase space the unpolarized virtual NLO cross section reads

$$\begin{aligned}\left(s^2\frac{d^2\sigma^{(1)}}{dt_1du_1}\right)^V &= \frac{1}{4(1-\epsilon)^2}\frac{\pi S_\epsilon}{\Gamma(1-\epsilon)}\left(\frac{t_1u_1-sm^2}{\mu^2 s}\right)^{-\epsilon}\delta(s+t_1+u_1)\\ &\quad\sum 2\mathrm{Re}[\mathcal{M}_S^{LO}\mathcal{M}_B^{V*}+\mathcal{M}_S^V\mathcal{M}_B^{LO*}]\end{aligned} \tag{3.23}$$

where

$$\begin{aligned} s &\equiv (k_1+k_2)^2\\ t_1 &\equiv t-m_q^2=(k_1-p_1)^2-m_q^2\\ u_1 &\equiv u-m_q^2=(k_1-p_2)^2-m_q^2\end{aligned} \tag{3.24}$$

and $\mathcal{M}^{LO}$ denotes the Born amplitude, $\mathcal{M}^V$ the virtual amplitude. The number of photon spin degrees of freedom in $n$ dimensions is $n-2$ so that averaging over the spin leads to $(n-2)^{-2}=(1-\epsilon)^{-2}/4$. The mass parameter $\mu$ has been introduced because the coupling constant is not dimensionless any more in $n$ dimensions. The spacial angle constant $S_\epsilon=(4\pi)^{-2+\epsilon}$ and the remaining factors result from the calculation of the $n$-dimensional 2-particle phase space. Since only the initial photon state $J_z=0$ couples to the Higgs boson the polarized interference cross sections for $J_z=\pm 2$ are zero. Due to CP-invariance the polarized $J_z=0$ interference cross section is thus given by the unpolarized result:

$$\sigma_I^{++}=\sigma_I^{--}=2\sigma_I^{unpol} \tag{3.25}$$

It is therefore sufficient to calculate the unpolarized interference cross section in order to get the polarized result. The virtual loop integrals are reduced to scalar integrals by means of the reduction procedure outlined in Ref. [64]. The scalar integrals are listed in the Appendix. The virtual corrections encounter poles $\epsilon^{-1}$ due to UV and IR singularities but no collinear divergences since the quarks are massive. The UV divergences are absorbed by the renormalization of the quark mass, the quark wave function, the Yukawa coupling and the quark-photon coupling. The renormalization conditions for the quark self-energy $\Sigma(p)$ in the on-shell scheme

$$\Sigma_R(\not p=m)=0 \quad \text{and} \quad \left.\frac{\partial\Sigma_R(p)}{\partial\not p}\right|_{\not p=m}=0 \tag{3.26}$$

result in the renormalization constants of the quark mass and the quark field

$$Z_m=Z_2=1-\frac{3}{4}\frac{\alpha_s}{\pi}C_FC_\epsilon\left(\frac{1}{\epsilon}+\frac{4}{3}\right) \tag{3.27}$$

The colour factor is given by $C_F=(N_c^2-1)/(2N_c)$. The constant $C_\epsilon$ summarizes the terms that typically arise in dimensional regularization

$$C_\epsilon=\Gamma(1+\epsilon)\left(\frac{4\pi\mu^2}{m_b^2}\right)^\epsilon \tag{3.28}$$

The Ward identity fixes the renormalization constant for the quark-photon vertex: $Z_1=Z_2$. Since in NLO QCD processes the Higgs fields and the vacuum expectation values are not renormalized the renormalization constant for the scalar Higgs-Yukawa couplings is given by

$$Z_{\varphi f\bar f}=Z_mZ_2\ , \quad \varphi=h,H \tag{3.29}$$

The pseudoscalar Higgs-Yukawa coupling includes the matrix $\gamma_5$. The 't Hooft/Veltman prescription, applied for the treatment of $\gamma_5$ in $n$ dimensions, breaks Lorentz and chiral invariance. This requires the introduction of a counterterm in order to restore the symmetries. The renormalization constant for the A coupling to fermions reads

$$Z_{Af\bar{f}} = Z_m Z_2 Z_5 \tag{3.30}$$

with the constant

$$Z_5 = 1 - 2C_F \frac{\alpha_s}{\pi} \tag{3.31}$$

In order to absorb large logarithms in the QCD corrections the Yukawa coupling is defined in terms of the running $\overline{\text{MS}}$ quark mass. The remaining IR singularities are canceled by the contribution from the soft gluons.

**Gluon brems-strahlung**

The next-to-leading order correction due to gluon brems-strahlung

$$\gamma(k_1) + \gamma(k_2) \to q(p_1) + \bar{q}(p_2) + g(k) \tag{3.32}$$

is built up by the interference of the gluon radiation diagrams of the signal and background process. It encounters IR singularities resulting from soft gluon radiation. For the calculation of the $\mathcal{O}(\alpha_S)$ real correction to the interference part, the cross section $\sigma_I^{(1)R}$ is divided into an IR finite and IR singular part

$$\sigma_I^{(1)R} = [\sigma_I^{(1)R} - \sigma_E] + \sigma_E \tag{3.33}$$

The cross section $\sigma_E$ contains all IR singularities so that the sum in brackets is manifestly IR finite. $\sigma_E$ can be obtained in the Eikonal approximation where the soft gluon momentum is neglected with respect to the quark momenta. In this limit the real singular amplitude factorizes from the Born amplitude,

$$\mathcal{M}^R_{sing} = \mathcal{M}_{LO} T^a_{ij} g_s \left\{ \frac{p_1 \epsilon^*(k)}{p_1 k} - \frac{p_2 \epsilon^*(k)}{p_2 k} \right\} \tag{3.34}$$

$T^a_{ij}$ denote the generators of the colour group $SU(3)$ and $\epsilon(k)$ the gluon polarization vector. Summing over the gluon polarizations the matrix element squared reads

$$\sum |\mathcal{M}^R_{sing}|^2 = 4C_F \pi \alpha_s \left\{ \frac{2p_1 p_2}{(p_1 k)(p_2 k)} - \frac{m_q^2}{(p_1 k)^2} - \frac{m_q^2}{(p_2 k)^2} \right\} \sum |\mathcal{M}_{LO}|^2 \tag{3.35}$$

The differential three particle phase space $dPS_3(P \equiv k_1 + k_2; p_1, p_2, k)$ which turns up in the calculation of the 2 → 3 process (3.32) can be decomposed into two two-particle phase spaces:

$$dPS_3(P; p_1, p_2, k) \;=\; \frac{dQ^2}{2\pi} dPS_2(P; k, Q) dPS_2(Q; p_1, p_2) \tag{3.36}$$

The two differential phase space factors $dPS_2$ correspond to the processes where the two photons with total momentum $P$ decay into the gluon and an intermediate state $X$ with momentum $Q$ which subsequently decays into the quark anti-quark pair. The invariant mass of the state $X$ is given by $Q^2 = zs$ $(4m_q^2/s < z < 1)$. The upper limit of $z$ corresponds to the IR region where the gluon momentum $k$ approaches 0. The lower limit is given by the fact that the invariant mass of $X$ must be large enough to produce two quarks.

In the calculation of $\sigma_E$ the decomposition (3.36) allows to factorize the soft gluon kinematics from the remaining kinematics which become equal to the kinematics of the Born process $\gamma\gamma \to q\bar{q}$ in the IR region. Since the singularities originate only from the soft gluon momentum, the variable $z$ is set equal to 1 in the quark momenta in the IR limit so that the quark velocity is given by $\beta = (1 - 4m_q^2/s)^{1/2}$. The differential Eikonal cross section can then be written as

$$d\sigma_E = C_E d\sigma_{LO} \tag{3.37}$$

where $C_E$ contains the IR singularities

$$C_E = \frac{dQ^2 dPS_2(P;k,Q)}{2\pi} \, 4C_F\pi\alpha_s \left\{ \frac{2p_1p_2}{(p_1k)(p_2k)} - \frac{m_q^2}{(p_1k)^2} - \frac{m_q^2}{(p_2k)^2} \right\} \tag{3.38}$$

and $d\sigma_{LO}$ is the LO cross section of the process $\gamma\gamma \to q\bar{q}$

$$d\sigma_{LO} = \frac{1}{8s(1-\epsilon)^2} dPS_2(P;p_1,p_2) \sum |\mathcal{M}_{LO}|^2 \tag{3.39}$$

The factor $1/[8s(1-\epsilon)^2]$ results from the flux factor and the average over the photon spin degrees of freedom. The differential two particle phase space is given by

$$dPS_2(P;p_1,p_2) = \frac{\beta^{1-2\epsilon}}{32\pi^2} \left( \frac{16\pi\mu^2}{s} \right)^{\epsilon} \frac{(1-\cos^2\theta)^{-\epsilon}}{\Gamma(1-\epsilon)} \, d\cos\theta \, d\phi \, , \quad \beta = \sqrt{1 - 4m_q^2/s} \tag{3.40}$$

The calculation of $dPS_2(P;k,Q)$ in $n$ dimensions leads to

$$\begin{aligned} dPS_2(P;k,Q) &= \frac{dv}{8\pi} \left( \frac{4\pi\mu^2}{s} \right)^{\epsilon} \frac{(1-z)^{1-2\epsilon}}{\Gamma(1-\epsilon)} v^{-\epsilon}(1-v)^{-\epsilon} \\ v &= \frac{1}{2}(1-\cos\theta_0) \, , \quad z = \frac{Q^2}{s} \end{aligned} \tag{3.41}$$

where $\theta_0$ denotes the angle between the gluon and the incoming photons in the c.m. system. With $dQ^2 = sdz$ we have

$$dPS_2(P;k,Q)\frac{dQ^2}{2\pi} = \frac{s(1-z)}{16\pi^2} F_\epsilon \, dz \, dv \tag{3.42}$$

with $F_\epsilon$ containing the $\epsilon$ dependence

$$F_\epsilon = (1-z)^{-2\epsilon} \frac{v^{-\epsilon}(1-v)^{-\epsilon}}{\Gamma(1-\epsilon)} \left( \frac{4\pi\mu^2}{s} \right)^{\epsilon} \tag{3.43}$$

The integration boundaries are given by

$$0 \le v \le 1 \, , \quad \tau_0 \le z \le 1 \, , \quad \tau_0 = 4\frac{m_q^2}{s} \tag{3.44}$$

Keeping in mind that the quark momenta are parameterized according to the Born kinematics the straightforward calculation of the Eikonal factor $C_E$ results in

$$C_E = \bar{C}_\epsilon C_F \frac{\alpha_s}{\pi} \left\{ \frac{1}{\epsilon}[1 - (1+\beta^2)f(\beta)] + (1+\beta^2)g(\beta) + 2f(\beta) \right\} \tag{3.45}$$

where

$$\bar{C}_\epsilon = \Gamma(1+\epsilon)\left(\frac{4\pi\mu^2}{s(1-\tau_0)^2}\right)^\epsilon \tag{3.46}$$

and

$$f(\beta) = \frac{1}{2\beta}\ln\frac{1+\beta}{1-\beta}\,, \quad g(\beta) = \frac{1}{2\beta}\left\{Li_2\left(\frac{-2\beta}{1-\beta}\right) - Li_2\left(\frac{2\beta}{1+\beta}\right)\right\} \tag{3.47}$$

The infrared singularities of $d\sigma_E = C_E d\sigma_{LO}$ cancel those of the virtual corrections. The finite contribution to the interference radiation cross section

$$[d\sigma_I^{(1)R} - d\sigma_E] = \frac{1}{8s} dPS_3(P;k_1,k_2,k)\sum[|\mathcal{M}_I|^2 - |\mathcal{M}_{sing}|^2] \tag{3.48}$$

is calculated numerically in 4 dimensions, *i.e.* $\epsilon = 0$. The momenta in the interference matrix element $\mathcal{M}_I$ are parameterized according to the three jet kinematics where $z \neq 1$. In contrast, in the singular matrix element $\mathcal{M}_{sing}$, calculated from Eq. (3.35), only the gluon momentum is given in the three jet kinematics and the quark momenta are parameterized in the Born kinematics since they have to be treated in the same way as in the integration of $d\sigma_E$.

Adding the $\mathcal{O}(\alpha_s)$ virtual and brems-strahlung contributions provides the NLO interference cross section. The total interference cross section without cuts is also given by the imaginary part of the Higgs-$\gamma\gamma$ form factor via the optical theorem. Since the form factor at NLO can be extracted from the literature [55, 56] it serves as a quantitative cross check for the obtained result.

**4.) Two-jet final state**

For reasons outlined above the photons will be taken polarized and the bottom-quark production will be analysed in the two-jet final state topology. A final state will be regarded as two-jet event if the gluon energy $E_g$ is less than a minimal gluon energy $E_g^{min}$ or if two of the three jets are collinear. In this analysis $E_g^{min}$ will be chosen as

$$E_g^{min} = 0.1\sqrt{s_{\gamma\gamma}} \tag{3.49}$$

where $\sqrt{s_{\gamma\gamma}}$ denotes the c.m. energy in the $\gamma\gamma$ fusion process. Two jets will be combined to a single jet if the angle $\alpha$ between them is less than

$$\alpha_{min} = 10^\circ \tag{3.50}$$

The 2-jet result can be obtained from the NLO result and the 3-jet cross section $\sigma_{3j}(\gamma\gamma \to b\bar{b} + g)$ which has been calculated for polarized photons in the signal, background and interference process. The two-jet cross section is then given by

$$\begin{aligned} \sigma_{2j(\gamma\gamma\to b\bar{b})} &= \sigma_{NLO} \\ &- \int_{E_g^{min}} dE_g \int_{\alpha_{min}} d\alpha(b\bar{b})\, d\alpha(bg)\, d\alpha(\bar{b}g)\, \frac{\partial^4\sigma_{3j}}{\partial E_g\, \partial\alpha(b\bar{b})\, \partial\alpha(bg)\, \partial\alpha(\bar{b}g)} \end{aligned} \tag{3.51}$$

Leading higher order contributions due to large double logarithms, which become important in the 2-jet topology for $J_z = 0$, have been resummed [51, 52]. The resummed cross section is given by

$$\sigma_{resum}^{J_z=0} = \mathcal{F}\,\sigma_{LO}^{J_z=0} \tag{3.52}$$

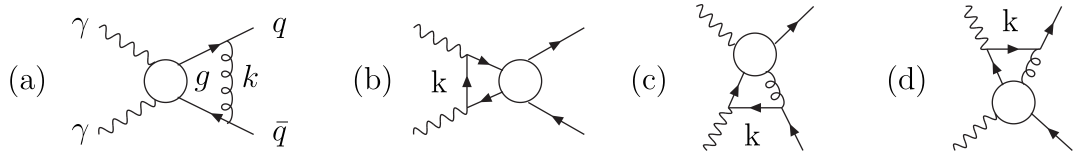

Figure 3.11: *Schematic one-loop topologies contributing to the form factor* $\mathcal{F}_g$ *[diagram (a)] and* $\mathcal{F}_q$ *[diagrams (b)–(d)]. The blob denotes a hard* $2 \to 2$ *subprocess compared to the soft momentum* $k$*.*

For signal (S), background (B) and interference (I) process, respectively, the resummation form factor $\mathcal{F}$ reads

$$\begin{aligned} \mathcal{F}_S &= \mathcal{F}_g \\ \mathcal{F}_B &= \mathcal{F}_g \mathcal{F}_q^2 \\ \mathcal{F}_I &= \mathcal{F}_g \mathcal{F}_q \end{aligned} \tag{3.53}$$

$\mathcal{F}_g$ denotes the Sudakov resummation factor and $\mathcal{F}_q$ the non-Sudakov factor. The dynamical origin of the signal, background and interference form factors is explained in detail in [51]. A brief understanding at $\mathcal{O}(\alpha_s)$ shall be given here. At NLO the Sudakov and non-Sudakov double logarithms in the $J_z = 0$ state arise in four non-overlapping kinematic regions. They are depicted in Fig. 3.11. One is related to the emission of a soft real gluon and the exchange of a soft virtual gluon that connects two helicity conserving vertices. This configuration [diagram (a) in Fig. 3.11] occurs both in the signal and background process. The soft gluon contribution can be factorized from the Born amplitude resulting in the NLO term of the expansion of $\sqrt{\mathcal{F}_g}$. For the background there are three more kinematic regimes [diagrams (b)–(d) in Fig. 3.11]. They involve a soft virtual quark connecting a helicity conserving and a helicity violating vertex. Factorizing these contributions from the Born amplitude one is left with the NLO term in the expansion of the non-Sudakov form factor $\mathcal{F}_q$. Since the Sudakov and non-Sudakov factors factorize at the amplitude level,

$$\begin{aligned} \mathcal{M}_S^{resum} &= \sqrt{\mathcal{F}_g} \mathcal{M}_S^{LO} \\ \mathcal{M}_B^{resum} &= \sqrt{\mathcal{F}_g} \mathcal{F}_q \mathcal{M}_B^{LO} \end{aligned} \tag{3.54}$$

the results of Eq. (3.53) are obtained.

The form factors $\mathcal{F}_g$ and $\mathcal{F}_q$, including the leading and next-to-leading order running coupling $\alpha_s$, are taken from [52]. The cross section for $b\bar{b}$ production with initial state helicity $J_z$ in the 2-jet topology including resummation then reads

$$\sigma^{J_z}(\gamma\gamma \to b\bar{b}) = \sigma_{2j}^{J_z} + \sigma_{LO}^{J_z} \hat{\mathcal{F}}_{resum}^{J_z} \tag{3.55}$$

For $J_z \neq 0$ a resummation of higher orders is not necessary. For $J_z = 0$ $\hat{\mathcal{F}}_{resum}$ reads

$$\hat{\mathcal{F}}_{resum}^{J_z=0} = \mathcal{F} - 1 - \mathcal{F}(\alpha_s) \tag{3.56}$$

$\mathcal{F}(\alpha_s)$ denotes the $\mathcal{O}(\alpha_s)$ contribution of the form factor $\mathcal{F}$, cf. Eqs. (3.52), (3.53). The definition (3.56) takes into account that the LO cross section and the full next-to-leading order result is already included in $\sigma_{2j}^{J_z=0}$. In the notation of [52] the $\mathcal{O}(\alpha_s)$ part of the form factors $\mathcal{F}$ reads

$$\begin{aligned}
\mathcal{F}_S(\alpha_s) &= \frac{\alpha_s C_F}{\pi}\Big(\ln\frac{s}{m_b^2}\left[\frac{1}{2}-\ln\frac{s}{4l_c^2}\right]+\ln\frac{s}{4l_c^2}-1+\frac{\pi^2}{3}\Big)\\
\mathcal{F}_B(\alpha_s) &= 6\tilde{\mathcal{F}}+\mathcal{F}_S(\alpha_s)\\
\mathcal{F}_I(\alpha_s) &= 3\tilde{\mathcal{F}}+\mathcal{F}_S(\alpha_s)
\end{aligned} \tag{3.57}$$

where the one-loop hard form factor $\tilde{\mathcal{F}}$ is given by

$$\tilde{\mathcal{F}} = -C_F\frac{\alpha_s}{4\pi}\ln^2\frac{s}{m_b^2} \tag{3.58}$$

The cut $l_c$ was introduced in the calculation of the resummation factors in order to separate soft gluons from hard gluons. In the soft gluon region the Eikonal-approximation, exploited in the calculation of the resummation factors, is valid. The cut $l_c \leq E_g^{min}$ further subdivides the 2-jet region that is characterized by gluons with energies less than $E_g^{min}$. The dependence on this phase space slicing parameter cancels at one-loop level since the full NLO calculation is included. As suggested as best guess in Ref. [65] the cut $l_c$ will be chosen equal to $E_g^{min}$ in the following. The strong coupling constant $\alpha_s$ is taken at the scale $\sqrt{s}$.

### 3.3.2 The $\tau^+\tau^-$ channel

For the LO process $\gamma\gamma \rightarrow \tau^+\tau^-$ the signal, background and interference cross section can be extracted from the corresponding LO quark cross sections (3.15),(3.20) and (3.22) by replacing the Yukawa coupling in the Higgs decay appropriately, the quark mass and charge with the analogous $\tau$ lepton values and setting the colour factor $N_c = 1$. At NLO there are no QCD corrections in the final state but only in the $\gamma\gamma\Phi$ form factor.

### 3.3.3 Chargino and neutralino production

Likewise the $\tau^+\tau^-$ channel the chargino and neutralino production does not involve final state QCD corrections. Due to the different masses in the final state the expression for chargino production via intermediate Higgs states is more cumbersome than in the case of quark anti-quark production. With the Higgs to chargino couplings listed in Table 3.1 and with the same notation as in subsection 3.3.1 the chargino $\tilde{\chi}_i^+\tilde{\chi}_j^-$ production cross sections for photons with initial polarization $J_z = 0$ after integration over $|\cos\theta| < c$ can be cast into the form

$$\begin{aligned}
\sigma_{S,ij}^{++/--} &= \frac{G_F^2\alpha^2\beta_{ij}M_W^2 c}{32\pi^3}\\
&\times \Bigg\{\sum_{\varphi=h,H}|\mathcal{G}_\varphi|^2\Big[(1-\mu_i-\mu_j)\left(|g_{\varphi\tilde{\chi}_i\tilde{\chi}_j}|^2+|g_{\varphi\tilde{\chi}_j\tilde{\chi}_i}|^2\right)\\
&\quad -\frac{2M_{\tilde{\chi}_i}M_{\tilde{\chi}_j}}{s}(g_{\varphi\tilde{\chi}_i\tilde{\chi}_j}g_{\varphi\tilde{\chi}_j\tilde{\chi}_i}+g^*_{\varphi\tilde{\chi}_i\tilde{\chi}_j}g^*_{\varphi\tilde{\chi}_j\tilde{\chi}_i})\Big]\\
&+ |\mathcal{G}_A|^2\Big[(1-\mu_i-\mu_j)\left(|g_{A\tilde{\chi}_i\tilde{\chi}_j}|^2+|g_{A\tilde{\chi}_j\tilde{\chi}_i}|^2\right)\\
&\quad +\frac{2M_{\tilde{\chi}_i}M_{\tilde{\chi}_j}}{s}(g_{A\tilde{\chi}_i\tilde{\chi}_j}g_{A\tilde{\chi}_j\tilde{\chi}_i}+g^*_{A\tilde{\chi}_i\tilde{\chi}_j}g^*_{A\tilde{\chi}_j\tilde{\chi}_i})\Big]
\end{aligned}$$

$$\begin{aligned}
&+ \quad 2(1-\mu_i-\mu_j)\,\mathrm{Re}\Big[\mathcal{G}_h\mathcal{G}_H^*(g_{h\tilde{\chi}_i\tilde{\chi}_j}g^*_{H\tilde{\chi}_i\tilde{\chi}_j}+g^*_{h\tilde{\chi}_j\tilde{\chi}_i}g_{H\tilde{\chi}_j\tilde{\chi}_i})\Big] \\
&\quad -\frac{4M_{\tilde{\chi}_i}M_{\tilde{\chi}_j}}{s}\,\mathrm{Re}\Big[\mathcal{G}_h\mathcal{G}_H^*(g_{h\tilde{\chi}_i\tilde{\chi}_j}g_{H\tilde{\chi}_j\tilde{\chi}_i}+g^*_{h\tilde{\chi}_j\tilde{\chi}_i}g^*_{H\tilde{\chi}_i\tilde{\chi}_j})\Big] \\
&\mp \quad \sum_{\varphi=h,H}\Big(2(1-\mu_i-\mu_j)\,\mathrm{Re}\Big[\mathcal{G}_\varphi\mathcal{G}_A^*(g^*_{\varphi\tilde{\chi}_j\tilde{\chi}_i}g_{A\tilde{\chi}_j\tilde{\chi}_i}-g_{\varphi\tilde{\chi}_i\tilde{\chi}_j}g^*_{A\tilde{\chi}_i\tilde{\chi}_j})\Big] \\
&\quad +\frac{4M_{\tilde{\chi}_i}M_{\tilde{\chi}_j}}{s}\,\mathrm{Re}\Big[\mathcal{G}_\varphi\mathcal{G}_A^*(g^*_{\varphi\tilde{\chi}_j\tilde{\chi}_i}g^*_{A\tilde{\chi}_i\tilde{\chi}_j}-g_{\varphi\tilde{\chi}_i\tilde{\chi}_j}g_{A\tilde{\chi}_j\tilde{\chi}_i})\Big]\Big)\Big\}
\end{aligned} \tag{3.59}$$

The interference between the scalar and pseudoscalar Higgs channel is proportional to the minus (plus) sign for $\sigma^{++}$ ($\sigma^{--}$). $\mu_{i,j}$ denote the scaled chargino masses $M^2_{\tilde{\chi}_{i,j}}/s$ and $\beta_{ij}$ the velocity for non-degenerate chargino final states. The signal cross sections for $J_z=\pm 2$ are zero. The LO cross section for the background process $\gamma\gamma\to\tilde{\chi}_i^+\tilde{\chi}_i^-$ can be obtained from the corresponding quark process Eq. (3.20) by replacing the quark mass (charge) with the chargino mass (charge) and setting $N_c=1$. After $\cos\theta$ has been integrated out in the range $[-c,c]$ the polarized cross sections of the interference process $\gamma\gamma\to\tilde{\chi}_i^+\tilde{\chi}_i^-$ reads

$$\begin{aligned}
\sigma_{I,ii}^{++/--} &= -\frac{\sqrt{2}G_F\alpha^2 M_W M_{\tilde{\chi}_i}}{4\pi s}\ln\frac{1+\beta_{ii}c}{1-\beta_{ii}c} \\
&\quad\times\Big\{\sum_{\varphi}\Big[\beta_{ii}^2(\mathcal{G}_\varphi+\mathcal{G}_\varphi^*)(g_{\varphi\tilde{\chi}_i\tilde{\chi}_i}+g^*_{\varphi\tilde{\chi}_i\tilde{\chi}_i})\mp(\mathcal{G}_\varphi-\mathcal{G}_\varphi^*)(g_{\varphi\tilde{\chi}_i\tilde{\chi}_i}-g^*_{\varphi\tilde{\chi}_i\tilde{\chi}_i})\Big] \\
&\quad - \Big[(\mathcal{G}_A+\mathcal{G}_A^*)(g_{A\tilde{\chi}_i\tilde{\chi}_i}+g^*_{A\tilde{\chi}_i\tilde{\chi}_i})\mp\beta_{ii}^2(\mathcal{G}_A-\mathcal{G}_A^*)(g_{A\tilde{\chi}_i\tilde{\chi}_i}-g^*_{A\tilde{\chi}_i\tilde{\chi}_i})\Big]\Big\} \\
\sigma_{I,ii}^{+-/-+} &= 0
\end{aligned} \tag{3.60}$$

The minus (plus) sign in the contributions proportional to $(\mathcal{G}_\Phi-\mathcal{G}_\Phi^*)$ $(\Phi=h,H,A)$ corresponds to $\sigma^{++}$ ($\sigma^{--}$). Assuming CP-invariance, the couplings $g_{\Phi\tilde{\chi}_i\tilde{\chi}_j}$ are real and orthogonal so that the formulae (3.59) and (3.60) adopt a much simpler form.

In the neutralino channel there are no background and interference contributions at LO. The neutralino signal cross section is given by the chargino result (3.59) after replacing the masses appropriately and the chargino couplings $g_{\Phi\tilde{\chi}_i\tilde{\chi}_j}$ with the neutralino couplings $g_{\Phi\tilde{\chi}_i^0\tilde{\chi}_j^0}$, cf. Table 3.1. For equal neutralinos in the final state Bose symmetry requires an additional factor 1/2.

### 3.3.4 Results

The cross section of the linear collider process

$$e^+e^-\to\gamma\gamma\to X_1X_2\ , \quad X_{1,2}=t,b,\tau,\tilde{\chi}_i^\pm,\tilde{\chi}_i^0 \tag{3.61}$$

is obtained by folding the cross section of the subprocess $\gamma\gamma\to X_1X_2$ denoted by $\hat{\sigma}$ with the $\gamma\gamma$ luminosity. The $\gamma\gamma$ luminosity for Compton scattered photons off (polarized) electron/positron beams has been calculated [66]. It has been given as a function of the photon energy, of the initial electron/positron and laser polarization as well as of the final state photon helicities.

The differential photon luminosity $\mathcal{L}^{\gamma\gamma}$ is maximal and peaked towards high energies if the electron/positron and laser beams are polarized and have opposite helicity. The electron/positron helicities $P_{e^\pm}$ will therefore be chosen equal to 1 in the following and the

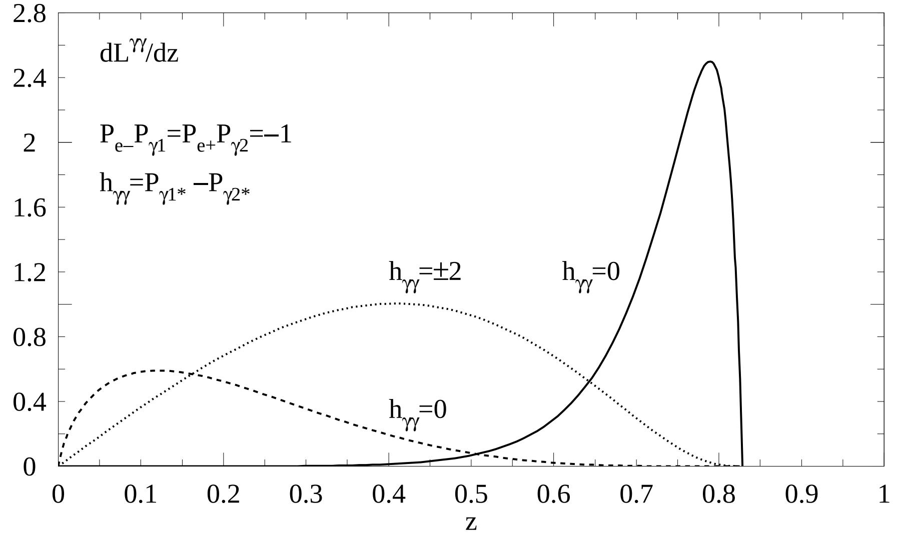

Figure 3.12: *The differential* $\gamma\gamma$ *luminosity as a function of* $z = \sqrt{s_{\gamma\gamma}}/\sqrt{s_{ee}}$ *for the* $e^+e^-$ *c.m. energy* $\sqrt{s_{ee}} = 500$ *GeV.* $\sqrt{s_{\gamma\gamma}}$ *denotes the* $\gamma\gamma$ *c.m. energy. The curves correspond to different polarizations of the final state photons. The full curve is the result for the outgoing photon helicities* $P_{\gamma_1^*} = P_{\gamma_2^*} = 1$ *and the dashed one for* $P_{\gamma_1^*} = P_{\gamma_2^*} = -1$. *The curves for* $P_{\gamma_1^*} = 1$, $P_{\gamma_2^*} = -1$ *and* $P_{\gamma_1^*} = -1$, $P_{\gamma_2^*} = 1$ *are identical and added in one curve.*

incoming photon helicities $P_{\gamma_{1,2}}$ are set equal to $-1$ each. For illustration, Fig. 3.12 shows the differential luminosity for this helicity choice and $\sqrt{s_{ee}} = 500$ GeV. The curves correspond to different helicity combinations between the outgoing photons. As can be inferred from the figure, the luminosity is maximal and peaked at the upper end of the energy range of the scattered photons if their helicities are $P_{\gamma_1^*} = P_{\gamma_2^*} = 1$.

The polarized fermion, respectively SUSY particle production cross section is given by a superposition of the different helicity combinations of the scattered photons:

$$\sigma^{pol}(e^+e^- \to X_1X_2) = \int_{\tau_0}^{\frac{x}{x+1}} dz \sum_{h_i,h_j=+,-} \frac{d\mathcal{L}^{\gamma\gamma}(h_ih_j)}{dz}\, \hat{\sigma}^{h_ih_j}(\gamma\gamma \to X_1X_2; \hat{s}_{\gamma\gamma} = z^2 s_{ee}) \quad (3.62)$$

where $\tau_0 = (M_{X_1} + M_{X_2})/\sqrt{s_{ee}}$ with $\sqrt{s_{ee}}$ denoting the c.m. energy of the incoming electron and positron. $\sqrt{\hat{s}_{\gamma\gamma}}$ stands for the c.m. energy of the $\gamma\gamma$ fusion subprocess. The upper integration limit depends on $x = (2\sqrt{s_{ee}}\omega_0)/M_e^2$ where $M_e$ denotes the electron mass. The laser energy $\omega_0$ will be chosen equal to 1.26 eV in the subsequent analysis.

The formulae of the polarized subprocess cross sections $\hat{\sigma}$ for the signal, background and interference reaction have been given in the previous subsections. In the case of $b\bar{b}$ production the resummed cross section for the 2-jet final state, cf. Eq. (3.55), will be used.

### $b\bar{b}$ final state

Fig. 3.13 shows the total cross section and the result for the signal and background part of $b\bar{b}$ production in the two-jet topology as a function of the pseudoscalar Higgs mass $M_A$. The c.m. energy of the incoming electron and positron has been chosen such that the energy squared of the subprocess $\hat{s}_{\gamma\gamma} = z_0^2 s_{ee}$ is equal to $M_A^2$. $z_0$ is the position where the differential luminosity $[d\mathcal{L}^{++} + \mathcal{L}^{--}]/dz$ becomes maximal for $\sqrt{s}_{ee}$. The fusion process folded with the

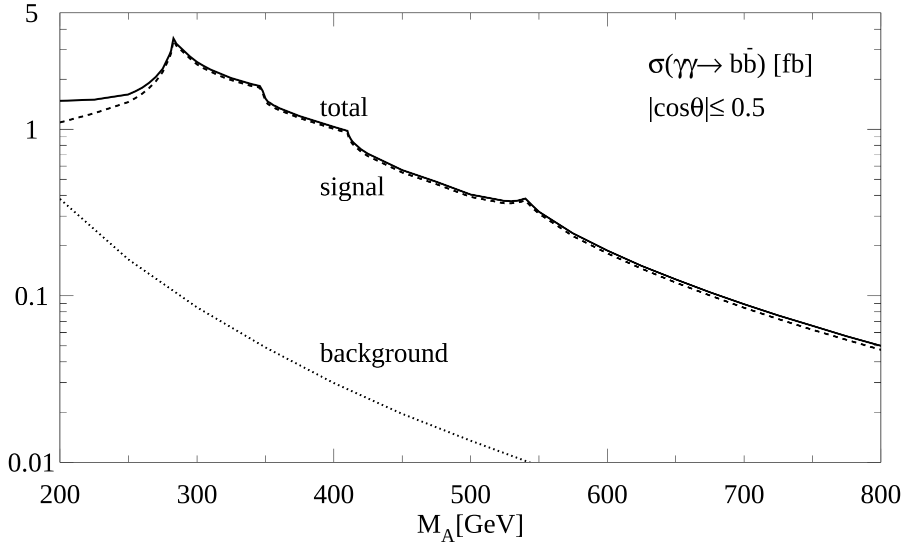

Figure 3.13: *The total, signal and background cross sections of the process* $\gamma\gamma \to b\bar{b}$ *for* $\mu = M_2 = 200$ *GeV and* $\tan\beta = 7$. $\cos\theta$ *has been integrated in the range* $[-0.5...0.5]$.

$\gamma\gamma$ luminosity is then integrated over the range

$$\begin{aligned}[z_{min}, z_{max}] &= [z_0 - 5\,\mathrm{GeV}/\sqrt{s}_{ee}, z_0 + 5\,\mathrm{GeV}/\sqrt{s}_{ee}] \\ &= [(M_A - 5\,\mathrm{GeV})/\sqrt{s}_{ee}, (M_A + 5\,\mathrm{GeV})/\sqrt{s}_{ee}] \qquad (3.63)\end{aligned}$$

This choice of $z_0$ and $\sqrt{s}_{ee}$ guarantees that the pseudoscalar Higgs boson $A$ is nearly produced on-shell in the signal process

$$\sigma_S^{pol}(e^+e^- \to b\bar{b}) = \int_{z_{min}}^{z_{max}} dz\ \hat{\sigma}_S^{++}(\gamma\gamma \to b\bar{b}; \hat{s}_{\gamma\gamma}) \left[\frac{d\mathcal{L}^{++}}{dz} + \frac{d\mathcal{L}^{--}}{dz}\right] \qquad (3.64)$$

particularly since $[d\mathcal{L}^{++}+\mathcal{L}^{--}]/dz$ drops rapidly around the maximum, cf. Fig. 3.12. Furthermore, the signal process is folded with the maximum luminosity for a given electron/positron c.m. energy. The integration interval $(2 \times 5)$ GeV$/\sqrt{s}_{ee}$ accounts for the limited energy resolution of about 10 GeV which may be achieved at a high-luminosity $e^+e^-$ linear collider.

The interference cross section here and in the following plots is not shown separately since it is fairly small in this specific numerical example, only of $\mathcal{O}(10^{-3}$ fb). The heavy CP-even Higgs mass $M_H$ and $M_A$ differ by at most $\sim$ 2.5 GeV for the chosen SUSY parameter set. The interference cross section, which is proportional to the real part of the MSSM Higgs propagators, is therefore almost vanishing since $A$ and $H$ are produced nearly on-shell and the contribution of the light scalar Higgs is very much suppressed as it is far off-shell.

The SUSY parameters are chosen as $\mu = M_2 = 200$ GeV, $\tan\beta = 7$, common sfermion mass $M_S = 1$ TeV and the SUSY breaking trilinear couplings are set equal to 0. The NLO corrections and leading higher order contributions have been included in the way outlined above. The $\mathcal{O}(\alpha_s)$ real and virtual corrections to the signal part amount up to $\sim$ 20% compared to the LO cross section. The NLO background cross section is about a factor 10 to 60 larger than the LO result in the considered mass range because at next-to-leading order the $J_z = 0$ background suppression by $m_b^2/s$ is removed and becomes of $\mathcal{O}(1)$. In the case of the interference part the NLO corrections are large.

The background contribution can be reduced enormously by cutting away the 3-jet events. With the chosen cuts defining the 2-jet topology the background is suppressed by 2 orders of magnitude compared to the complete 3-jet NLO cross section. The reason is that the 2-jet NLO cross section is dominated by the helicity-flipped $J_z = 0$ states which are suppressed. [It is the non helicity-flipped $J_z = 0$ states which remove the $m_b^2/s$ suppression at NLO.] In contrast the signal is reduced by $\sim 40\%$ while the interference part is reduced by an order of magnitude.

The background can further be suppressed by cutting the integration region in $\cos\theta$ where $\theta$ denotes the angle between the $b$-quark and the beam axis. The integration range has been chosen $[-0.5, 0.5]$ in Fig. 3.13. More than 90% of the background proceeding via $t$- and $u$-channel diagrams is cut away whereas the isotropic signal is reduced by a factor 1/2 only.

In the 2-jet topology the resummation turns out to be important. It increases the 2-jet signal by up to $\sim 30\%$ and changes the interference 2-jet cross section by $\mathcal{O}(100\%)$. For the background reaction the impact is even larger. At the upper mass range of $M_A$ it is the main contribution to the complete 2-jet background result.

The signal process shows a rich structure. The two peaks at $M_A \approx 280$ and 540 GeV are due to the behaviour of the $\gamma\gamma A$ form factor which peaks when the chargino thresholds $\tilde{\chi}_1^+\tilde{\chi}_1^-$ and $\tilde{\chi}_2^+\tilde{\chi}_2^-$ are reached. The masses of the charginos for the chosen parameter set are

$$M_{\tilde{\chi}_1^\pm} = 141\text{ GeV}\ , \qquad M_{\tilde{\chi}_2^\pm} = 270\text{ GeV} \tag{3.65}$$

The kink around 410 GeV can be understood from the $H \to b\bar{b}$ branching fraction, c.f. Fig. 3.8. It drops when the $\tilde{\chi}_1^+\tilde{\chi}_2^-$ channel opens. The peak at $\sim 350$ GeV, finally, is a mixture of the behaviour of the branching fraction and $\gamma\gamma A$ form factor at the $t\bar{t}$ threshold.

As can be inferred from Fig. 3.13 the resummed 2-jet signal cross section amounts up to a few fb whereas the background is less than 0.5 fb. By focusing on the 2-jet final states and cutting the integration range in $\cos\theta$ the signal to background ratio can be enhanced to significances $S/\sqrt{B}$ above 5 in the whole $M_A$ range 200...800 GeV for an integrated luminosity of $\int\mathcal{L} = 100\text{ fb}^{-1}$ in three years. Demanding the total cross section to exceed 1 fb $\gamma\gamma$ fusion allows to find the pseudoscalar and scalar Higgs bosons for masses less than about 400 GeV. Higgs production via Compton back-scattered photons therefore provides a powerful mechanism for the heavy MSSM Higgs boson search in the $b\bar{b}$ channel.

### $t\bar{t}$ and $\tau^+\tau^-$ final states

Fig. 3.14 illustrates the results for the $t\bar{t}$ and $\tau^+\tau^-$ final states at next-to-leading order. If not stated otherwise the SUSY parameters and the smearing procedure with the $\gamma\gamma$ luminosity are the same as in the $b\bar{b}$ case in the following.

For $t\bar{t}$ the (2+3)-jet NLO cross section has been plotted. Since the electric top-quark charge is 2/3 and enters in the fourth power in the background process, the background is rather large. Furthermore, the 2-jet topology is not suppressed very much because of the large top-quark mass. Therefore the restriction on the 2-jet final state is not efficient. Also due to the large top mass the cut in $\cos\theta$ does not lead to a significant enhancement in the signal to background ratio though it may be improved if the cut is chosen equal to 0.7. Nevertheless, the significance does not achieve the $5\sigma$ level.

Below the $t\bar{t}$ threshold the complete $\tau^+\tau^-$ production cross section amounts up to $\mathcal{O}(10\text{ fb})$. The $\tau^\pm$ charge is unity so that the background is large. Since the $\tau$ mass is rather small

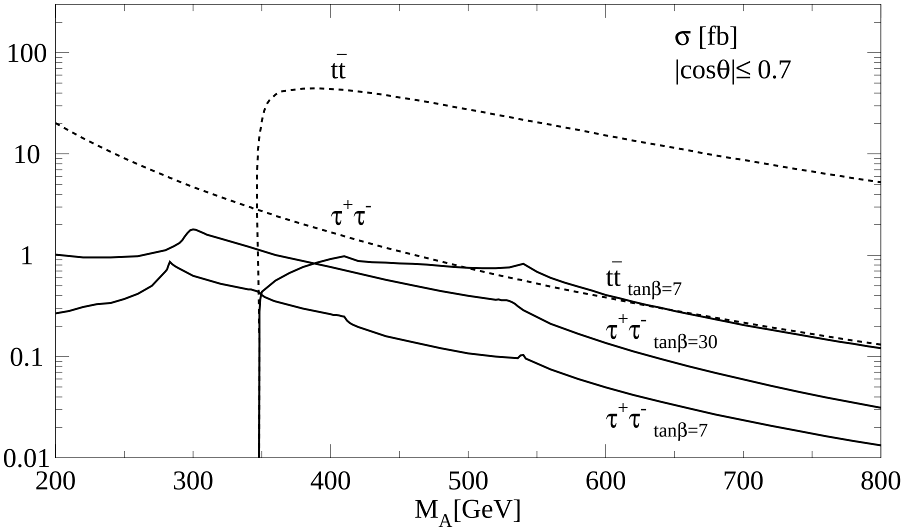

Figure 3.14: *Full lines: The signal cross sections of the processes* $\gamma\gamma \to t\bar{t}$ $(\tan\beta = 7)$ *and* $\gamma\gamma \to \tau^+\tau^-$ $(\tan\beta = 7, 30)$ *for* $\mu = M_2 = 200$ *GeV. Dashed lines: Background processes only.* $\cos\theta$ *has been integrated in the range* $[-0.7...0.7]$.

a cut in $\cos\theta$ is worthwhile. The best signal to background ratio can be achieved for the integration region $|\cos\theta| < 0.7$. Nevertheless for moderate values of $\tan\beta = 7$ the signal is too small compared to the background cross section to reach significances above 5. The situation changes for larger values of $\tan\beta$ since the branching fraction of $A \to \tau^+\tau^-$ increases with $\tan\beta$ as can be inferred from Fig. 3.8. The signal cross section is therefore larger for $\tan\beta = 30$ whereas the background cross section remains the same so that in the mass range $M_A \approx 300...480$ GeV significances exceeding 5 with $\tau^+\tau^-$ production cross sections larger than 1 fb can be achieved.

In contrast to the $\tau^+\tau^-$ channel, increasing the value of $\tan\beta$ will not enhance the signal to background ratio in $t\bar{t}$ production since the $A$ Yukawa coupling to the top quarks is proportional to $\cot\beta$ so that the $t\bar{t}$ signal cross section decreases with rising $\tan\beta$.

The peaks and kinks in the $t\bar{t}$ and $\tau^+\tau^-$ signal cross sections can readily be explained by the behaviour of the $H$ and $A$ branching fractions in these channels and the $\gamma\gamma A$ form factor when the various chargino and the $t\bar{t}$ production thresholds are reached. For $\tan\beta = 30$ the chargino masses are

$$M_{\tilde{\chi}_1^\pm} = 149\ GeV\ , \qquad M_{\tilde{\chi}_2^\pm} = 266\ GeV \tag{3.66}$$

**Chargino and neutralino production**

Fig. 3.15 presents the NLO cross sections for chargino and neutralino production as a function of the pseudoscalar Higgs mass. Each curve shows the sum of all possible chargino and neutralino final states, respectively, except for $\tilde{\chi}_1^0\tilde{\chi}_1^0$. The chargino masses for the chosen parameter set have been given in (3.65) and the neutralino masses are

$$\begin{array}{lllll} M_{\tilde{\chi}_1^0} & = & 85\ GeV & M_{\tilde{\chi}_2^0} & = & 148\ GeV \\ M_{\tilde{\chi}_3^0} & = & 208\ GeV & M_{\tilde{\chi}_4^0} & = & 271\ GeV \end{array} \tag{3.67}$$

Since the chargino and neutralino masses are rather large a cut in $\theta$ does not improve the

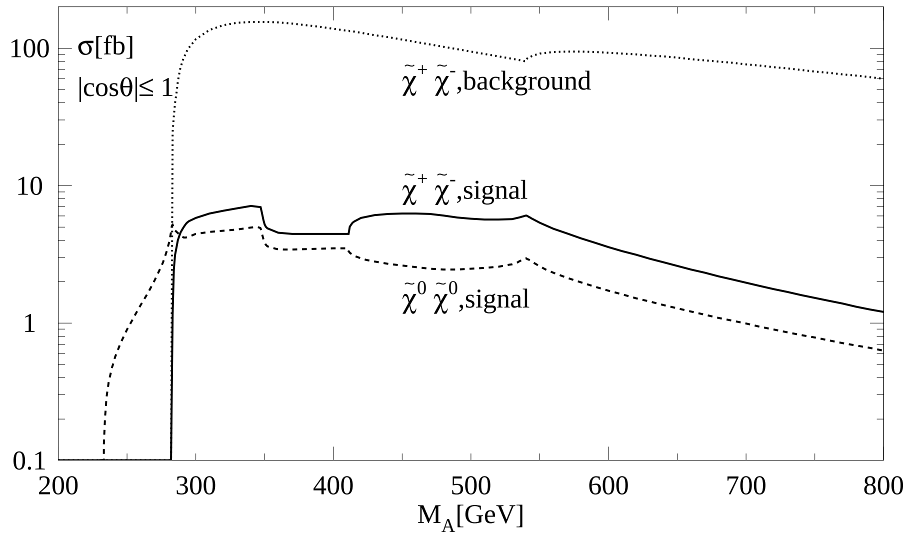

Figure 3.15: *Full (dashed) line: Signal cross section of the process* $\gamma\gamma \to \tilde{\chi}^+\tilde{\chi}^-$ $(\gamma\gamma \to \tilde{\chi}^0\tilde{\chi}^0)$. *Dotted line: Background cross section of the process* $\gamma\gamma \to \tilde{\chi}^+\tilde{\chi}^-$. *All possible chargino and neutralino final states except for* $\tilde{\chi}^0_1\tilde{\chi}^0_1$ *are added up. The SUSY parameters are chosen* $\mu = M_2 = 200$ *GeV and* $\tan\beta = 7$. $\cos\theta$ *has been integrated in the range* $[-1, ..., 1]$.

signal to background ratio. Therefore $\cos\theta$ has been integrated in the limits $-1$ and 1.

Above the $\tilde{\chi}^+_1\tilde{\chi}^-_1$ production threshold, *i.e.* $M_A \approx 280$ GeV, the chargino channel opens. Since the chargino charge is three times larger than the $b$-quark charge, the background is large and amounts up to $\mathcal{O}(100 \text{ fb})$. The kink at $\sim$ 540 GeV is related to the $\tilde{\chi}^+_2\tilde{\chi}^-_2$ threshold.

The signal cross section develops a rather complex structure due to the behaviour of the $H$ and $A$ chargino branching fractions at the $t\bar{t}$, $\tilde{\chi}^+_1\tilde{\chi}^-_2$ and the $\tilde{\chi}^+_2\tilde{\chi}^-_2$ thresholds. The form of the signal at the $t\bar{t}$ and $\tilde{\chi}^+_2\tilde{\chi}^-_2$ thresholds is in addition influenced by the behaviour of the $\gamma\gamma A$ form factor. The cross section varies between $\sim$ 1 to 6 fb. It is too small to allow for the Higgs detection in the chargino channel.

Above $M_A \approx 230$ GeV, the threshold for the $\tilde{\chi}^0_1\tilde{\chi}^0_2$ production is reached and the neutralino channel opens. It does not acquire any LO background and interference contributions due to neutralinos. The kinks and peaks in the signal curve correspond to the various chargino thresholds and the $t\bar{t}$ threshold. The neutralino branching fraction drops when the chargino channels open up. On the other hand the $\gamma\gamma A$ form factor peaks when the $\tilde{\chi}^+_1\tilde{\chi}^-_1$ and $\tilde{\chi}^+_2\tilde{\chi}^-_2$ thresholds are reached. The signal cross section amounts up to a few fb. Due to the lower branching ratio compared to the chargino channel the neutralino signal is smaller. Above $M_A \approx 280$ GeV the neutralino channel has to fight against the background stemming from the chargino decays: Neutralinos can decay into a lighter neutralino and a $Z$ boson, for example:

$$\tilde{\chi}^0_2 \to \tilde{\chi}^0_1 + Z \tag{3.68}$$

Charginos may decay into a neutralino and a $W^\pm$ boson:

$$\tilde{\chi}^\pm_1 \to \tilde{\chi}^0_1 + W^\pm \tag{3.69}$$

Due to the escaping LSPs and neutrinos the final states in the chargino and neutralino cascade decays are rather similar. Since the chargino background is very large it will be challenging to separate the neutralino signal from the chargino background. Exploiting the different decay topologies, however, the neutralino channel may serve for the heavy MSSM Higgs boson search also in the mass range above the chargino production threshold.

### 3.3.5 Discovery reach

The c.m. energy in all production channels has been integrated in a narrow energy range around $M_A$. Since the mass of the heavy scalar Higgs $H$ differs hardly from $M_A$ it is also produced almost on-shell. Though it will be very difficult if not impossible to separate the pseudoscalar and scalar heavy Higgs particle, the detection of additional heavy Higgs particles will help to disentangle the MSSM from the SM if only one light Higgs boson has been discovered at the LHC as it might be the case in the parameter region $M_A \gtrsim 200$ GeV and $\tan\beta \gtrsim 6$ up to 15.

The analysis has demonstrated that heavy MSSM Higgs production in polarized $\gamma\gamma$ fusion at a Compton collider provides an excellent mechanism to detect the pseudoscalar and scalar Higgs bosons in the $b\bar{b}$ channel for moderate values of $\tan\beta$. By this way the discovery region which is not covered by the LHC can be closed. In addition, the mass range up to which the Higgs bosons can be detected in $\gamma\gamma$ fusion extends up to $\sim 0.8\sqrt{s_{ee}}$ in contrast to $e^+e^-$ collisions with a discovery range of $\sim 0.5\sqrt{s_{ee}}$. For the detection in the $b\bar{b}$ channel it is crucial, however, to investigate 2-jet final states. Including NLO and resummation of higher orders the analysis has been completed to the currently most accurate level.

While the $t\bar{t}$ mode is not promising, an additional channel is provided by $\tau^+\tau^-$ production for large values of $\tan\beta$. The neutralino channel, finally, can be exploited in mass regions below the chargino threshold, if it is kinematically allowed, where it is not plagued by the large chargino background. Above the threshold the different topologies of the final states may help to extract the neutralino signal from the chargino background.

# Chapter 4

# The Lifetime of Higgs particles

The two basic properties characterizing particles are the mass and the lifetime. As outlined in the previous chapter the masses of the SM and MSSM Higgs particles can be determined with high accuracy at the LHC and high-energy $e^+e^-$ linear colliders. The determination of the lifetimes, *i.e.* the total widths of the Higgs bosons is a more difficult task, especially for Higgs states with narrow widths.

Starting with a theoretical overview over the total widths and the main decay channels of the SM Higgs boson and the MSSM Higgs scalars, several mechanisms will be presented, subsequently, which can be exploited at $e^+e^-$ linear colliders in order to determine the SM Higgs lifetime for masses in the intermediate range where it is narrow. The MSSM case will be discussed qualitatively.

## 4.1 The SM Higgs boson decays

The Higgs couplings to the $W$, $Z$ gauge bosons and to the fermions are proportional to the masses of these particles, cf. Eqs. (2.10), (2.14). Consequently, the Higgs boson will predominantly decay into the heaviest particles of the SM, i.e. $W$, $Z$ gauge bosons, top and bottom quark, if this is kinematically allowed.

The Higgs couplings to $\gamma\gamma$, $\gamma Z$ and $gg$ are mediated by heavy particle loops. The Higgs decays into these particles only play a rôle for Higgs masses below $\sim$ 140 GeV, where the total Higgs decay width is rather small. They are interesting since they are sensitive to scales far beyond the Higgs mass and thus to new particles whose masses are generated by the Higgs mechanism.

The main contributions to the $H\gamma\gamma$ coupling come from top-quark and $W$ boson loops. In the intermediate mass range, $M_W \le M_H \le 2M_Z$, the $W$-loop contribution dominates and interferes destructively with the fermion amplitude. The same holds true for the $H\gamma Z$ coupling. The Higgs coupling to gluons is practically almost built up by top-quark loops and the branching ratio is only sizeable below the $WW$ threshold.

The decay modes discussed in the following are generated with the FORTRAN program HDECAY [67]. They include electroweak [68] and QCD corrections [58, 59]. Also the decay into off-shell particles below the threshold is taken into account [69–71].

In Fig. 4.1 the total decay width and the branching ratios of the SM Higgs particle are shown as a function of the Higgs mass. Below about 140 GeV the total width is less than

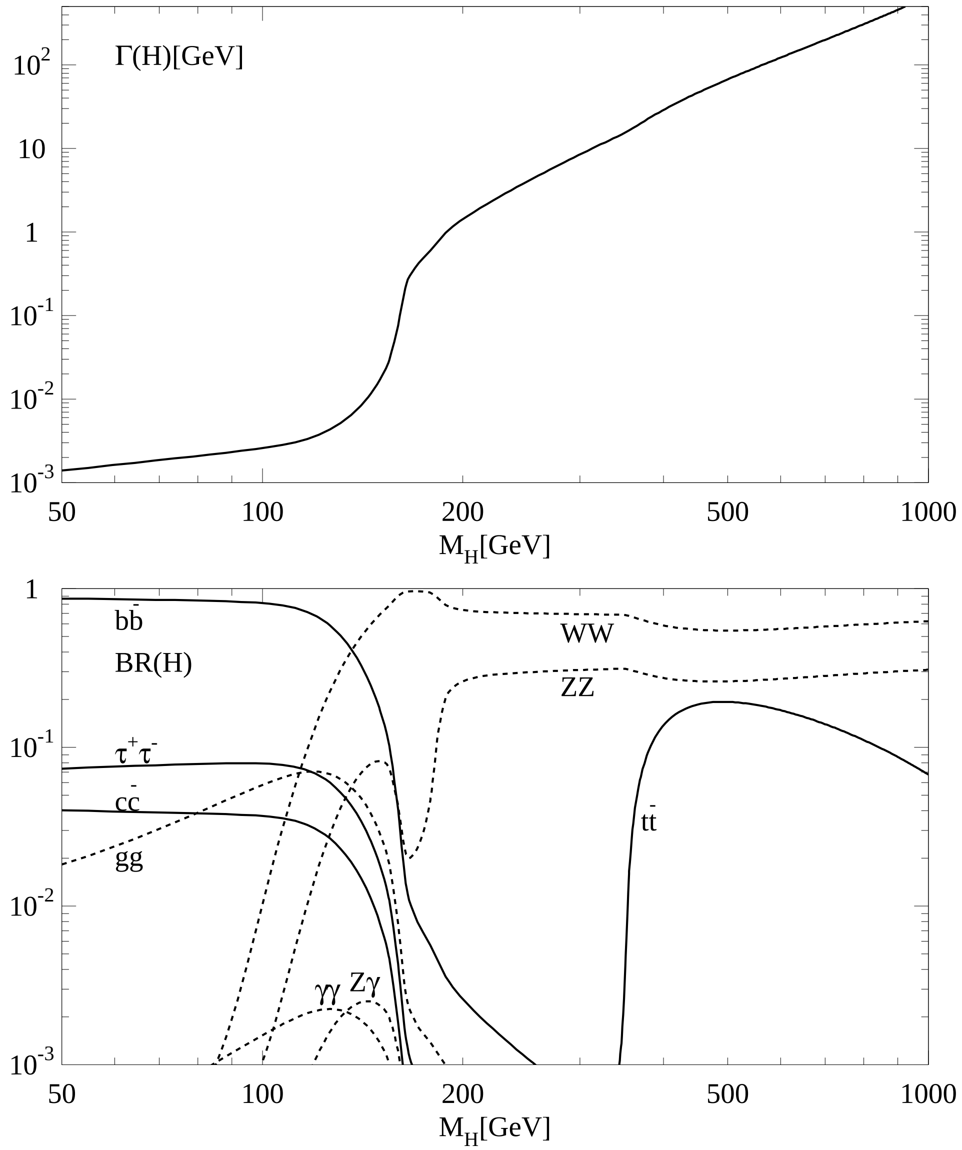

Figure 4.1: *(a) Total decay width of the SM Higgs boson as a function of its mass. (b) Branching ratios of the dominant decay modes of the SM Higgs particle.*

10 MeV, *i.e.* rather small. The Higgs preferentially decays into $b$-quarks with a branching ratio of about 85%. The next important decay channels are provided by the decays into $\tau^+\tau^-$, charm-quarks and gluons. Beyond $\sim$ 140 GeV the decay into $W$ bosons becomes dominant followed by the $ZZ$ decay mode. Above $M_H = 2m_t$ the decay into top quarks is kinematically possible. The branching ratio, however, always remains below 20% since the decay width is proportional to the Higgs mass whereas the leading $WW$ and $ZZ$ decay widths grow with the third power of the Higgs mass. Thus the total width strongly increases with the Higgs mass, up to 600 GeV for $M_H = 1$ TeV.

## 4.2 Decay modes of the MSSM Higgs particles

### 4.2.1 The total decay widths and branching ratios of non-SUSY decays

The MSSM Higgs bosons mainly decay into heavy quarks and gauge bosons if kinematically allowed. This is due to the fact that the corresponding couplings are proportional to the masses of the particles which are generated by the Higgs mechanism. In contrast to the SM, however, the decay into bottom quarks becomes dominant for large $\tan\beta$ since the couplings are enhanced in this case, c.f. Table 2.1. Furthermore, the couplings to $W$ and $Z$ bosons are suppressed by $\cos(\beta-\alpha)$ or $\sin(\beta-\alpha)$ compared to the SM couplings. The decay widths and branching ratios discussed below have been obtained by means of the FORTRAN program HDECAY [67]. The Higgs sector contains the radiative corrections due to top/bottom and squark loops calculated in the effective potential approach, and the NLO QCD corrections as well as the mixing in the stop and sbottom sectors are included [21]. Off-shell decays into vector gauge bosons and top-quarks below the threshold have also been taken into account [70, 71].

The leading order widths of $h$, $H$ into gluons are mediated by quark and squark loops which are important for squark masses below about 400 GeV [72]. In contrast to the SM, the bottom quark contribution can become important for large values of $\tan\beta$ where the relevant coupling is strongly enhanced. The pseudoscalar $A$ decay into gluons only involves quark loops and no squark loops since $A$ flips the helicity of the squarks whereas the gluon coupling to squarks conserves the squark-helicity. The decays of the CP-even neutral Higgs particles $h, H$ into photons are generated by heavy charged fermion, $W$ boson, charged Higgs boson, chargino and sfermion loops whereas the corresponding $A$ decay is mediated by fermion and chargino loops only.

The heavy scalar particle $H$ can also decay into a pair of light Higgs bosons or a pair of pseudoscalar bosons if kinematically allowed. The radiatively corrected Higgs self-couplings in the one-loop leading $m_t^4$ approximation are given by Eq. (2.49). Moreover, the heavy Higgs particles can decay into a gauge and a Higgs boson.

Figs. 4.2 and 4.3 show the total decay widths of the MSSM Higgs particles and the neutral Higgs boson branching ratios into non-SUSY particles as a function of the corresponding Higgs mass for two values of $\tan\beta = 3$, 50. As can be inferred from Fig. 4.3 the light scalar Higgs boson dominantly decays into bottom quarks, independent of $\tan\beta$, with a branching ratio up to about 90%. The remaining 10% are almost solely supplemented by the decay into $\tau$'s. At the maximum value of the light Higgs mass, *i.e.* in the decoupling limit, the branching ratios approach the SM values.

For large $\tan\beta$ the dominant decay mode of the heavy scalar Higgs boson is the decay into bottom quarks (90%), followed by the decay into $\tau^+\tau^-$ which amounts up to about 10%. For small values of $\tan\beta$, $H$ preferentially decays into a pair of light Higgs bosons when kinematically allowed. Otherwise the $b$ decay takes over the dominant rôle below the $t\bar{t}$ threshold. The next important channels are provided by the decays into $W$ and $Z$ bosons, respectively. Beyond the $t\bar{t}$ threshold the decay into top quarks is by far dominant.

For large values of $\tan\beta$ the branching ratios of the pseudoscalar Higgs show the same pattern as those for $H$. For small $\tan\beta$ values the bottom decay only dominates below the

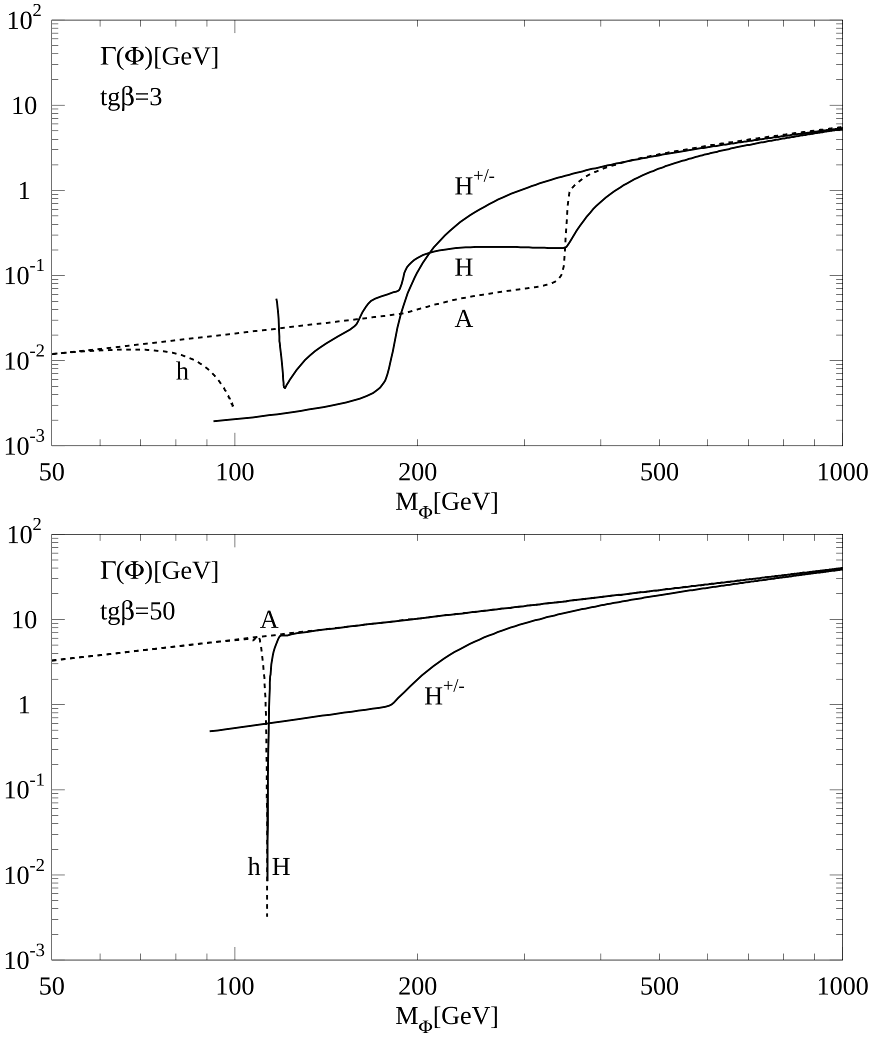

Figure 4.2: *Total decay widths of the MSSM Higgs particles as a function of the corresponding Higgs mass for* $\tan\beta = 3, 50$*. Decays into SUSY particles have not been taken into account and the common squark mass has been set to* $M_S = 1$ *TeV.*

$t\bar{t}$ threshold, the next important channels being the $Zh$ and $\tau^+\tau^-$ decay. Above the $Zh$ and below the $t\bar{t}$ threshold the $gg$ channel turns up. As soon as the $t\bar{t}$ threshold is reached, the $t\bar{t}$ decay is overwhelming.

### 4.2.2 Decays into SUSY particles

If MSSM Higgs boson decays into charginos and neutralinos are kinematically allowed they have to be taken into account. Their branching ratios may yield 100% below the various top-quark thresholds so that the Higgs boson search at the LHC becomes difficult because some of these decays develop invisible signatures [45].

The Higgs decays into sfermions of the first two generations are not important. If decays into sfermions of the third generation are kinematically allowed they can become sizeable, however, and reach branching ratios of up to 80%.

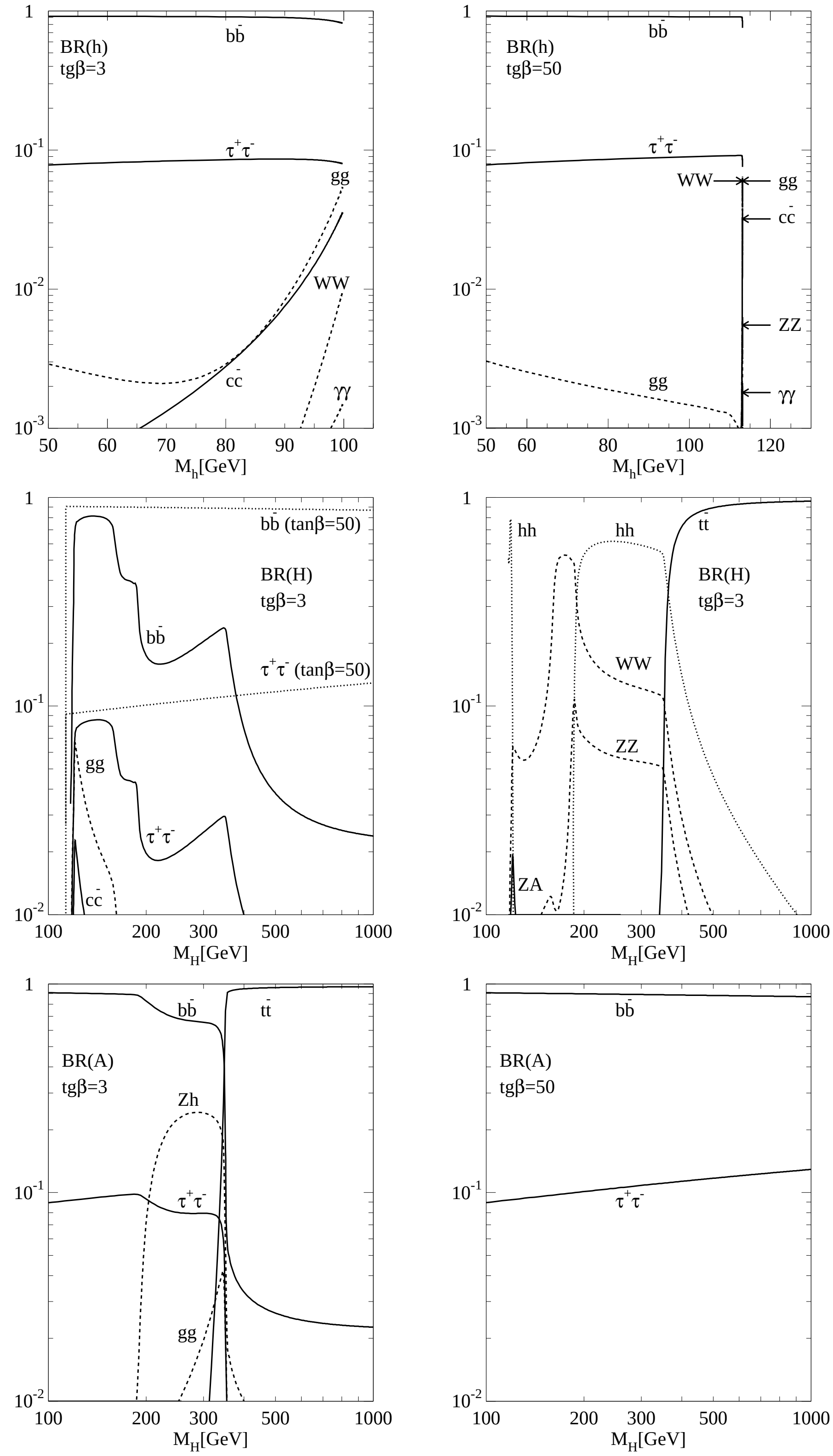

Figure 4.3: *Branching ratios of the neutral MSSM Higgs bosons as a function of the corresponding Higgs mass for* $\tan\beta = 3, 50$ *and vanishing mixing. Decays into SUSY particles are not included and the common squark mass has been set to* $M_S = 1$ *TeV.*

## 4.3 Determination of the lifetime of Higgs bosons

The lifetime of the Higgs bosons can be determined by exploiting the relation

$$\Gamma_{tot} = \Gamma_i / BR_i \tag{4.1}$$

where $\Gamma_i$ denotes the partial width of the decay $H \to$ final state $i$ and $BR_i$ the corresponding branching ratio. For this task several measurements have to be combined. The branching ratio $BR_i$ is determined by measuring both the exclusive process into the final state $i$ and the inclusive Higgs rate in the same production channel $X \to H$:

$$\begin{array}{lcl} \sigma^{incl}_{X\to H} & \sim & \Gamma_{H\to X} \\ \sigma^{excl}_{X\to i} & \sim & \Gamma_{H\to X} BR_i \end{array} \tag{4.2}$$

Considering all possible production channels at $e^+e^-$ colliders the Higgs-strahlung process $e^+e^- \to ZH$ is the only channel being suitable for an inclusive measurement. The Higgs scalar is detected by analysing the recoil spectrum of the $Z$ boson decay products that are visible. In the case of the MSSM also the associated production channels $Ah$ and $AH$ have to be taken into account.

The partial decay width $\Gamma_i$ is extracted from the inverse process $i \to H$ or in associated production where the Higgs particle is radiated off particle $i$. The Higgs boson can either decay into the same state $i$ or another state $j$. In the latter case the branching ratio $BR_j$ has also to be determined in the Higgs-strahlung process.

$$\begin{array}{rcl} \sigma_{i\to H\to i} & \sim & \Gamma_i BR_i \\ \text{or}\quad \sigma_{i\to H\to j} & \sim & \Gamma_i BR_j \end{array} \tag{4.3}$$

If either the initial or the final state $i$ are not on-shell the corresponding Higgs form factor will be probed at different scales in production and decay, respectively, thus allowing new physics to enter in the determination of the total width. These new effects are associated with a scale $\Lambda$ at which they become sizeable. If the scales $q^2$ at which the Higgs form factor is probed are small compared to $\Lambda^2$, the error due to new physics in the extraction of $\Gamma_{tot}$ is $\mathcal{O}(q^2/\Lambda^2)$.

In the following the mechanisms which can be exploited at high-energy $e^+e^-$ colliders for the measurement of $\Gamma_{tot}$ both in the SM and the MSSM in the intermediate mass range will be discussed from a theoretical point of view and some illustrative numbers will be given [73]. The analysis will be model-independent up to the error originating from the scale dependence of the Higgs couplings.

### 4.3.1 The total width of the SM Higgs boson

In the intermediate mass range the relevant channels for the extraction of the total width are given by $i = \gamma\gamma, WW$ and $ZZ$. While the $\gamma$'s are on-shell, the $W$ and $Z$ bosons can be off-shell. Demanding the $\gamma\gamma$ branching ratio $BR_{\gamma\gamma}$ to be bigger than $10^{-3}$ and $BR_{WW}, BR_{ZZ} > 10^{-2}$, the $\gamma\gamma$ channel can be used for $M_H \lesssim 155$ GeV, the $ZZ$ channel for $M_H \gtrsim 110$ GeV and the $WW$ channel in the whole intermediate range, cf. Fig. 4.1. For high-luminosity linear colliders this corresponds to an event rate $\mathcal{O}(10)...\mathcal{O}(10^2)$ for $\gamma\gamma$ and $WW/ZZ$ final states, respectively:

$$\begin{array}{l} \sqrt{s} = 350 \text{ GeV} \\ M_h = 100...200 \text{ GeV} \quad : \quad \sigma(ZH) = 150...70 \text{ fb} \quad \text{and } \int \mathcal{L} = 500 \text{ fb}^{-1} \end{array}$$

**a) $\gamma\gamma$ channel**
From a theoretical point of view the $\gamma\gamma$ channel provides the cleanest method for the determination of $\Gamma_{tot}$ since the photons are on-shell both in the production and the decay channel. The $\gamma\gamma$ fusion Higgs production with the $\gamma$'s resulting from the Compton scattering of laser light can be used to extract the Higgs decay width into $\gamma\gamma$:

$$\sigma(\gamma\gamma \to H) = 8\pi^2 \frac{\Gamma(H \to \gamma\gamma)}{M_H} \frac{d\mathcal{L}^{\gamma\gamma}}{ds_{\gamma\gamma}} \tag{4.4}$$

$d\mathcal{L}^{\gamma\gamma}/ds_{\gamma\gamma}$ denotes the $\gamma\gamma$ luminosity at $\sqrt{s_{\gamma\gamma}} = M_H$. The cross section and hence the partial width can be determined with an accuracy of about 2% [74]. The on-shell $\gamma$'s ensure the model-independence of the analysis.

Yet, the measurement of the branching ratio $BR_{\gamma\gamma}$ in the Higgs-strahlung channel

$$e^+e^- \to ZH \to Z + \gamma\gamma \tag{4.5}$$

is affected by a huge background rendering the error in $BR_{\gamma\gamma}$ as big as about 15% for $M_H \lesssim 130$ GeV [75]. This error translates into the maximum accuracy with which $\Gamma_{tot}$ can be determined in the $\gamma\gamma$ channel.

**b) $WW$ channel**
The $WW$ channel is a valuable alternative to the $\gamma\gamma$ mode [76]. The branching ratio into $W$ bosons, with one $W$ being virtual, in the lower intermediate Higgs mass range can be determined with an error of $\mathcal{O}(5\%)$ down to Higgs masses $M_H \approx 120$ GeV [76, 77] in the exclusive process

$$\sigma_{ZH\to ZWW} \equiv \sigma(e^+e^- \to ZH \to ZWW) \sim \Gamma_{ZZ} BR_{WW} \tag{4.6}$$

[In the following the $W$ and $Z$ bosons may be understood as virtual where appropriate.] The partial width in turn can be extracted from the $WW$ fusion process $e^+e^- \to \bar{\nu}_e \nu_e H$ [39–41] with

$$\sigma(e^+e^- \to \bar{\nu}_e \nu_e H) = \frac{2G_F^2 M_W^4}{M_H^2 \pi^2} \ln \frac{s}{M_H^2} \frac{\Gamma(H \to WW)}{M_H} [1 + \Delta_W] \tag{4.7}$$

$\Delta_W$ parameterizes the non-zero mass effects for $H$ and $W$ in the intermediate mass range. In the limit $M_W^2 \ll M_H^2 \ll s$ it approaches zero, $\Delta_W \to 0$.

The $W$ bosons in the fusion process are off-shell with a maximum virtuality of $\sim M_W/2$. Hence, the model dependence introduced by anomalous $HWW$ couplings is negligible compared to the experimental errors if this effect is associated with high scales $\Lambda = 1$ TeV.

The $H$ bosons produced in $WW$ fusion can be best detected in the $b\bar{b}$ decay channel

$$\sigma_{WW\to b\bar{b}} \equiv \sigma(WW \to H \to b\bar{b}) \sim \Gamma_{WW} BR_{b\bar{b}} \tag{4.8}$$

Therefore in order to extract the partial width $\Gamma_{WW}$ the branching ratio $BR(H \to b\bar{b})$ has to be measured, too. This can be done in the exclusive process

$$\sigma_{ZH\to Zb\bar{b}} \equiv \sigma(e^+e^- \to ZH \to Zb\bar{b}) \sim \Gamma_{ZZ} BR_{b\bar{b}} \tag{4.9}$$

Together with the inclusive process

$$\sigma_{ZH} \equiv \sigma(e^+e^- \to ZH) \sim \Gamma_{ZZ} \tag{4.10}$$

all ingredients necessary for the determination of $\Gamma_{tot}$ are available

$$\Gamma_{tot} = \frac{\Gamma_{WW}}{BR_{WW}} \sim \frac{\sigma_{WW\to b\bar{b}}}{BR_{WW}BR_{b\bar{b}}} \sim \frac{\sigma_{WW\to b\bar{b}}\sigma^2_{ZH}}{\sigma_{ZH\to Zb\bar{b}}\sigma_{ZH\to ZWW}} \tag{4.11}$$

For example, for $M_H = 120$ GeV ($\sqrt{s} = 350$ GeV, $\int \mathcal{L} = 500$ fb$^{-1}$) the errors in the various cross sections are: $(\delta\sigma/\sigma)_{WW\to b\bar{b}} \approx 2.6\%$ [78], $(\delta\sigma/\sigma)_{ZH\to Zb\bar{b}} \approx 2.4\%$ [76] and $(\delta\sigma/\sigma)_{ZH} \approx 2.1\%$ [76]. The error in $\Gamma_{tot}$ is therefore dominated by the error in $BR_{WW}$ being $\mathcal{O}(5\%)$. This results in $\delta\Gamma_{tot}/\Gamma_{tot} \approx 7.4\%$.

With rising Higgs mass the uncertainty in the determination of $BR_{b\bar{b}}$ increases since the branching ratio decreases and thus renders its measurement more difficult. For $M_H = 140$ GeV an error in $\Gamma_{tot}$ less than 10% [76, 78, 79] still seems feasible whereas for $M_H$ near and above the $H \to WW$ threshold the $b\bar{b}$ channel is not useful any more.

Instead the decay $H \to WW$ can be exploited in this mass range. The Higgs mass has to be reconstructed from the four-jet final state resulting from the decay of the $W$ bosons. In addition, for Higgs masses where the decay $H \to ZZ$ is not negligible, the $ZZ$ and $WW$ modes have to be separated by reconstructing their invariant 2-jet-masses. For $M_H = 160$ GeV ($\sqrt{s} = 350$ GeV, $\int \mathcal{L} = 500$ fb$^{-1}$) the cross section $e^+e^- \to WW \to H \to WW$ can be measured with an error of about 3.1% if an efficiency of $\sim 30\%$ for the detection of the $WW$ mode is assumed. Hence, with $(\delta\sigma/\sigma)_{ZH\to ZWW} = 3.5\%$ [77] and $(\delta\sigma/\sigma)_{ZH} = 2.8\%$ [77] the error in $\Gamma_{tot}$ will be 9.5%.

**c) $ZZ$ channel**

Provided the Higgs mass is large enough the $ZZ$ channel can be exploited for the measurement of the Higgs lifetime. The partial width $\Gamma(H \to ZZ)$ is accessible in the Higgs-strahlung process [37]

$$\sigma(e^+e^- \to ZH) = \frac{G_F(v_e^2 + a_e^2)}{3\sqrt{2}} \frac{M_Z^4}{M_H^3 s} \Gamma(H \to ZZ)[1 + \Delta_Z] \tag{4.12}$$

where $\Delta_Z$ accounts for the non-zero intermediate Higgs and $Z$ boson mass effects and $\Delta_Z \to 0$ for $M_Z^2 \ll M_H^2 \ll s$. One of the $Z$ bosons is virtual. The $HZZ$ coupling is measured at the scale $q^2 = s$ in this process whereas the exclusive process $e^+e^- \to ZH \to Z + ZZ$ which provides the branching ratio $BR(H \to ZZ)$ probes the $HZZ$ coupling at the scale $q^2 = M_Z^2$. Hence, for $\sqrt{s} = 500$ GeV and $\Lambda = 1$ TeV the error due to anomalous effects in the $HZZ$ coupling may be $\sim 25\%$. By measuring the Higgs-strahlung process at different c.m. energies and extrapolating down to $\sqrt{s} = M_Z$, the uncertainty due to new physics effects can be reduced to $\mathcal{O}(M_Z^2/\Lambda^2)$. The $ZZ$ fusion process $e^+e^- \to ZZ \to H$, though an order of magnitude smaller than the $WW$ fusion process, may serve as a cross-check. With a $Z$ boson virtuality of $\sim M_Z/2$ the error accounting for anomalous $HZZ$ couplings is less than in Higgs-strahlung.

For the detection of the process $HZ \to ZZZ$ most of the $Z$ decay channels can be used since the final state does not encounter any extra neutrinos. Furthermore the $ZZZ$ continuum background is small so that the error in the determination of the cross section is essentially given by the total rate in this channel.

### 4.3.2 Total widths of the MSSM Higgs particles

Since the MSSM contains a quintet of Higgs bosons the extraction of the lifetime of each Higgs scalar is more involved than in the SM. In order to illustrate the strategy to be followed the lifetime of the light CP-even Higgs boson $h$ will be discussed. The discussion may be understood as synopsis of the qualitative features concerning the determination of the lifetime. In order to make quantitative statements, a detailed experimental analysis has to be performed.

Fig. 4.3 shows the dominant branching ratios of $h$ for $\tan\beta = 3$ and 50 (decays into SUSY particles are not included). Outside the decoupling region the gauge boson channels play a minor rôle whereas the $b\bar{b}$ channel is dominating in the whole parameter range followed by the $\tau^+\tau^-$ channel. Especially for large $\tan\beta$ values the Yukawa coupling $hbb \sim m_b \tan\beta$ is strongly enhanced resulting in a total $h$ width much larger than in the SM for the same Higgs mass.

**a) Gauge boson channels**
For the reasons described above the gauge boson channels are less useful for the $h$ width measurement over most of the parameter range. Only in the decoupling limit they approach the SM values and the same methods as in the SM can be applied by properly taking into account the changes in the couplings due to mixing effects in the Higgs sector.

**b) $b\bar{b}$ channel**
The branching ratio $BR(h \to b\bar{b})$ required for the $\Gamma_{tot}$ determination in the $b\bar{b}$ channel can be extracted by comparing the inclusive process $e^+e^- \to Zh$ with the exclusive process $e^+e^- \to Zh \to Zb\bar{b}$. The measurement of the partial width $\Gamma(h \to b\bar{b})$ or equivalently the coupling $hb\bar{b}$ in the process $e^+e^- \to hb\bar{b}$ [80–82] is much more involved. The Higgs-radiation cross section $e^+e^- \to hb\bar{b}$ is small over a large part of the MSSM parameter range including the decoupling region. Being proportional to $\tan^2\beta$ it only becomes accessible for large values of $\tan\beta$.

The diagrams contributing to the processes $e^+e^- \to hb\bar{b}$ and $e^+e^- \to H/Ab\bar{b}$ are shown in Fig. 4.4. Since the associated production of $h$ with $b\bar{b}$ also includes the coupling $Ab\bar{b}$, the determination of the required Yukawa coupling is more complicated than in the SM. Yet, each coupling $\Phi b\bar{b}$ ($\Phi = h, H, A$) can be extracted by solving the equation system for all three processes. Assuming polarized electron/positron beams and the knowledge of the couplings $g_{ZZh/H}$ and $g_{ZAh/H}$ the cross sections for the processes $e^+e^- \to H_i b\bar{b}$ read

$$\begin{array}{rcl} \sigma_{hb\bar{b}} & = & |g_{hb\bar{b}}A_1 + g_{Ab\bar{b}}A_2 + A_3|^2 \\ \sigma_{Hb\bar{b}} & = & |g_{Hb\bar{b}}A'_1 + g_{Ab\bar{b}}A'_2 + A'_3|^2 \\ \sigma_{Ab\bar{b}} & = & |g_{hb\bar{b}}A''_1 + g_{Hb\bar{b}}A''_2 + g_{Ab\bar{b}}A''_3|^2 \end{array} \qquad (4.13)$$

where $A_i, A'_i, A''_i$ $(i = 1, 2, 3)$ denote the helicity amplitudes of the corresponding subprocesses. Up to discrete ambiguities this system is in principle solvable for all $b\bar{b}$ Higgs Yukawa couplings.

As is evident from the previous discussion and Fig. 4.4 the final state $b\bar{b}b\bar{b}$ includes several resonant channels. By applying experimental cuts the various resonances have to be separated so that the contribution due to $b \to bh$ can be extracted. The Yukawa coupling $hb\bar{b}$ *e.g.* could be determined in the region where one of the possible $b$-pairings forms a resonance at the $h$ mass and the invariant mass of the remaining $b$-pair does not reconstruct the pseudoscalar mass $M_A$. In the decoupling limit $h$ behaves like a SM boson and is not affected by heavy Higgs boson resonances.

**c) $\tau^+\tau^-$ channel**
Since the $\tau^+\tau^-$ Higgs Yukawa coupling is proportional $m_\tau \tan\beta$ this channel can be exploited

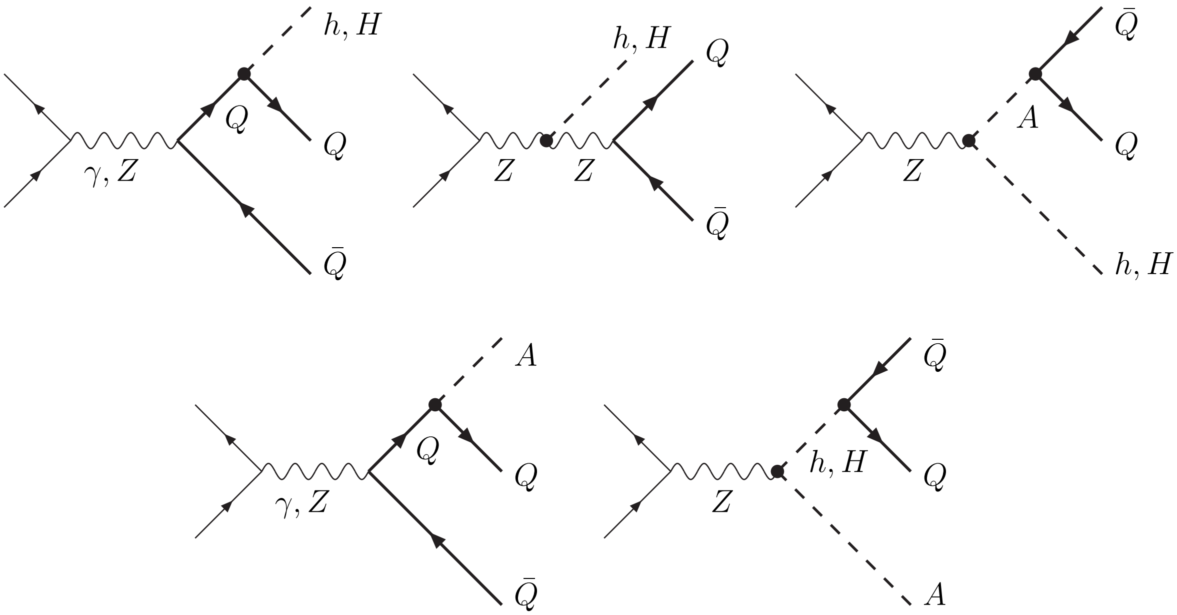

Figure 4.4: *Diagrams contributing to the radiation of scalar and pseudoscalar MSSM Higgs bosons in* $e^+e^-$ *collisions;* $Q = t, b$ *[82].*

for large $\tan\beta$, too. On the one hand no ambiguity in pairing the $b$-jets arises here. On the other hand the neutrino in the $\tau$ decay requires the reconstruction of the invariant $\tau^+\tau^-$ mass, which is necessary for the separation of the $A$ resonance, from the mass recoiling against the $b\bar{b}$ pair.

# Chapter 5

# SM and MSSM Higgs self-couplings

In the preceding chapters the discovery of Higgs particles in the SM and the MSSM, the determination of their masses and lifetimes and the Higgs couplings to gauge and matter particles have been described in detail. In order to complete the profile of the Higgs bosons, the Higgs self-couplings have to be probed. This step is essential for the clarification of the nature of the mechanism that creates particle masses in the SM and its supersymmetric extensions. Only the knowledge of the Higgs self-couplings will allow for the reconstruction of the Higgs potential so that the Higgs mechanism can be established experimentally.

In this chapter various double and triple Higgs production mechanisms in the SM and the MSSM will be analysed [83]. [The relation to general 2-Higgs doublet models has been discussed in Ref. [84].] At hadron colliders and high-energy $e^+e^-$ linear colliders Higgs pair production via double Higgs-strahlung off $W$ or $Z$ bosons [85–87] and through $WW$ or $ZZ$ fusion [87–94] allows direct access to the trilinear Higgs self-couplings. In addition at *pp* colliders gluon-gluon fusion [61],[94–97] can be exploited, and at photon colliders high-energy $\gamma\gamma$ fusion [87, 88, 98] is sensitive to $\lambda_{HHH}$. For the MSSM case all possible neutral multi-Higgs final states as defined in Ref. [23] will be taken into account and thus a theoretically complete picture for testing the trilinear Higgs self-couplings will be elaborated. By including new results from parton level background analyses [99–101] and detector simulations [100–102] the potential of measuring the trilinear Higgs self-couplings at $e^+e^-$ linear colliders and at LHC, respectively, will be discussed. A short remark will be made on the present expectations of determining the quadrilinear Higgs self-coupling(s). The first section will be dedicated to the linear collider, first examining the SM case before turning on to the MSSM. The second section will focus on the LHC.

## 5.1 Higgs self-couplings at $e^+e^-$ linear colliders

The two main processes at $e^+e^-$ linear colliders which are sensitive to $\lambda_{HHH}$ are double Higgs-strahlung and $WW$ double-Higgs fusion:

$$\begin{aligned} &\text{double Higgs-strahlung} \quad : \quad && e^+e^- \underset{Z}{\longrightarrow} ZHH \\ &WW \text{ double-Higgs fusion}: \quad && e^+e^- \underset{WW}{\longrightarrow} \bar{\nu}_e \nu_e HH \end{aligned} \tag{5.1}$$

The cross section for $ZZ$ fusion is an order of magnitude smaller than that for $WW$ fusion because of the small electron-$Z$ couplings.

double Higgs-strahlung: $e^+e^- \to ZHH$

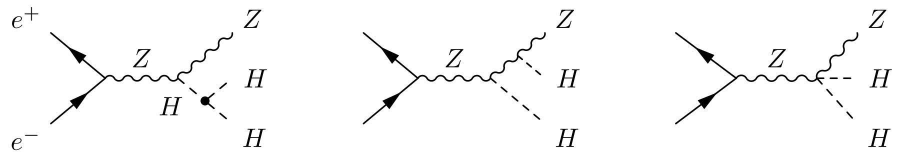

$WW$ double-Higgs fusion: $e^+e^- \to \bar{\nu}_e \nu_e HH$

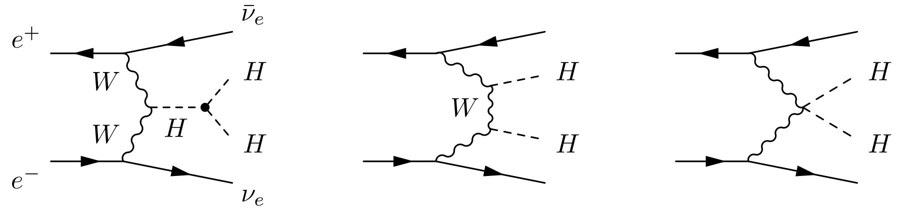

Figure 5.1: *Generic diagrams for the processes which contribute to Higgs-pair production in the Standard Model at $e^+e^-$ linear colliders: double Higgs-strahlung and $WW$ fusion.*

Fig. 5.1 shows the generic diagrams which contribute to the two processes. Their cross sections are small, of the order of a few fb and below, for Higgs masses in the intermediate range so that high-luminosities as expected at $e^+e^-$ linear colliders are needed in order to produce sufficiently high signal rates and to separate the signal from the background.

In the minimal supersymmetric extension there are five physical Higgs states as outlined in Chapter 2. This leads to six CP-invariant trilinear Higgs couplings among the neutral Higgs bosons. The couplings including radiative corrections in the one-loop leading $m_t^4$ approximation are given in Eq. (2.49). In the following analysis the dominant one-loop and the leading two-loop corrections to the masses and couplings have been included, cf. [21, 103]. The upper bound of the light Higgs mass strongly depends on the radiative corrections and thus on the values of the mixing parameters $A$ and $\mu$. In contrast, the trilinear Higgs self-couplings show a weak dependence on the radiative corrections when evaluated for the physical Higgs masses. In Figs. 5.2 and 5.3 the trilinear Higgs self-couplings and the gauge-Higgs couplings are given as a function of $M_A$ for two representative values of $\tan\beta$, *i.e.* $\tan\beta = 3, 50$. Around $M_A = 120$ GeV the couplings vary rapidly for large $\tan\beta$. This region corresponds to the cross-over of the mass branches in the neutral CP-even Higgs sector, cf. Eq. (2.47). As can be inferred from Fig. 5.3 the couplings involving a pair of pseudoscalar Higgs bosons are rather small compared to the couplings involving pure CP-even Higgs states. Note also that the trilinear Higgs couplings may become zero for some parameter values. Fig. 5.4 demonstrates for $\lambda_{hhh}$ and $\lambda_{Hhh}$ the modification of the trilinear couplings when mixing effects are included. Evidently, the change is rather small. The mixing effects are also discussed in Ref. [104].

At $e^+e^-$ linear colliders there are many processes which involve the trilinear MSSM Higgs-

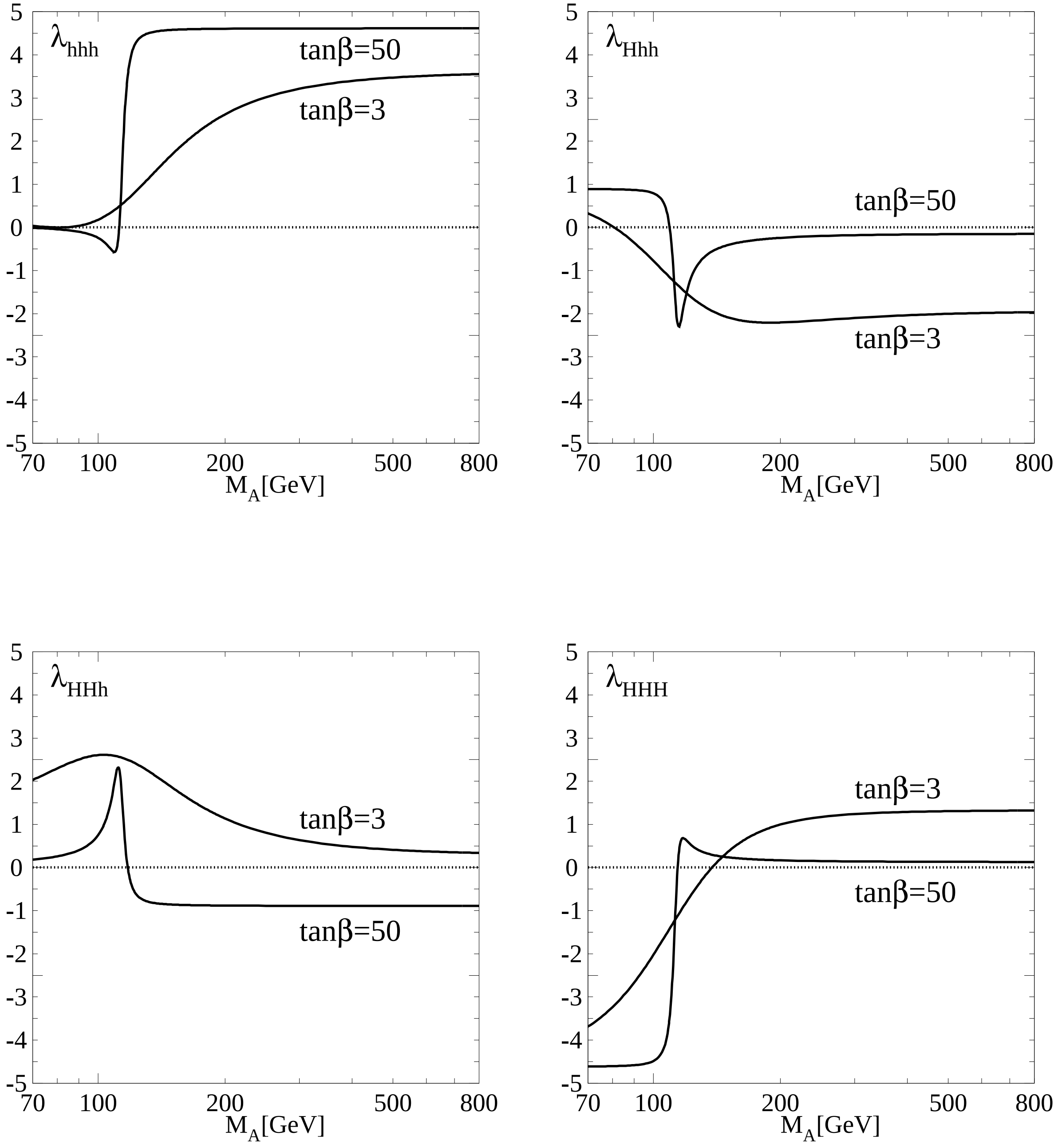

Figure 5.2: *Variation of the trilinear couplings between CP-even Higgs bosons with $M_A$ for tan$\beta = 3$ and 50 in the MSSM; the region of rapid variations corresponds to the $h/H$ cross-over region in the neutral CP-even sector.*

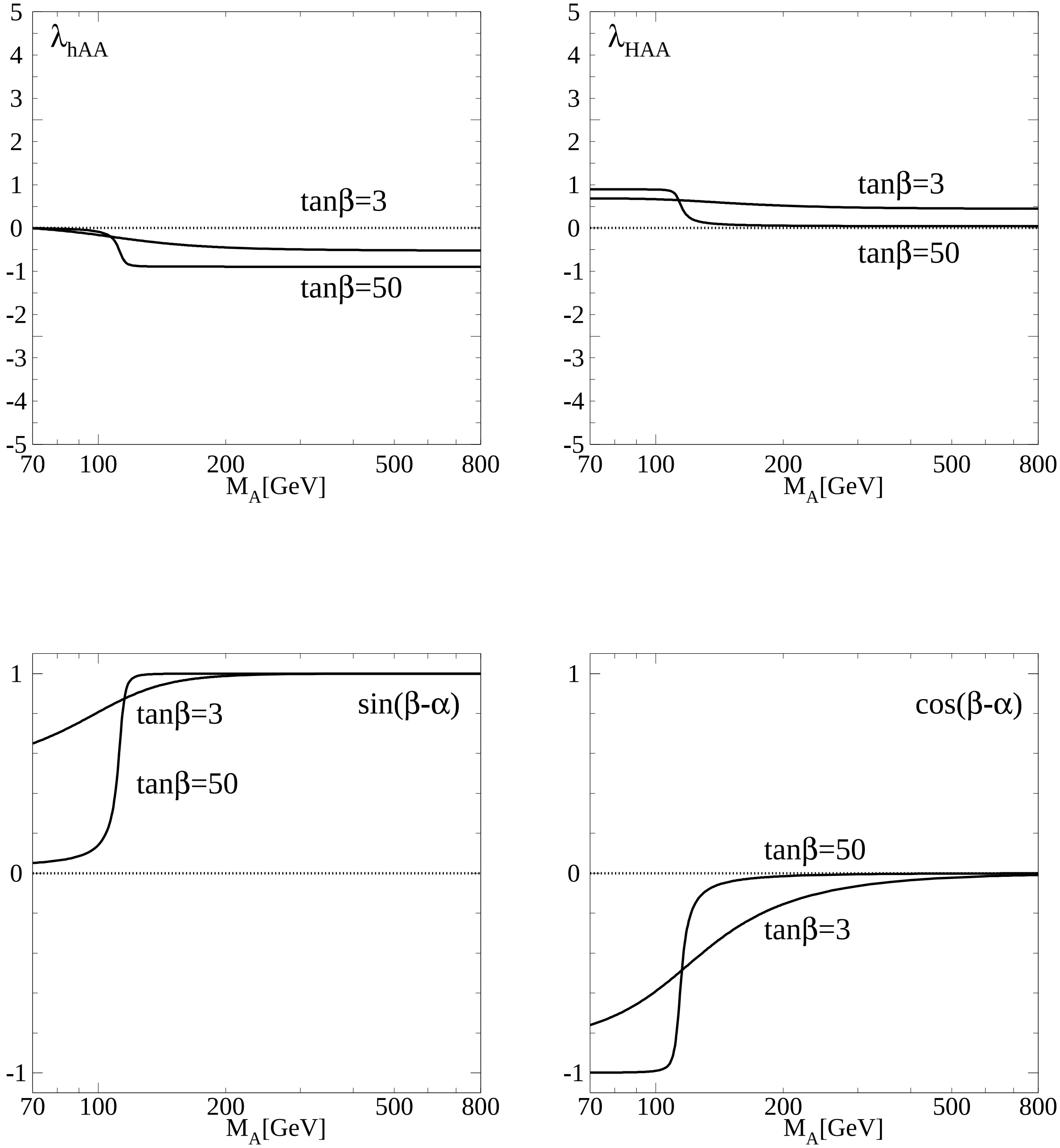

Figure 5.3: *Upper set: Variation of the trilinear couplings between CP-even and CP-odd Higgs bosons with* $M_A$ *for* $\tan\beta = 3$ *and* 50 *in the MSSM. Lower set: ZZh and ZZH gauge couplings in units of the SM coupling.*

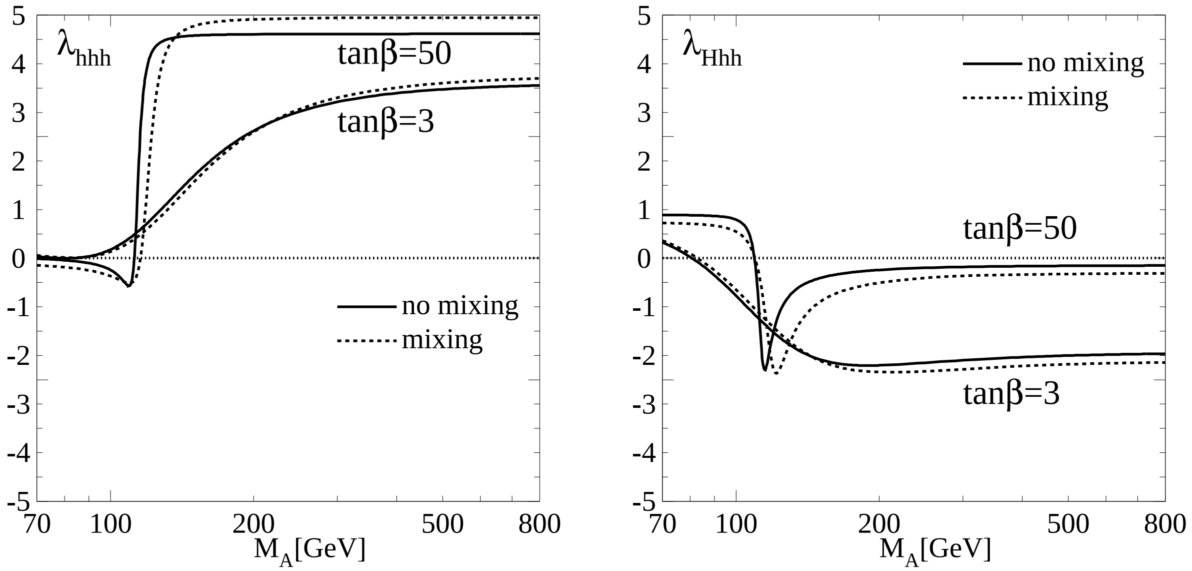

Figure 5.4: *Modification of the trilinear couplings* $\lambda_{hhh}$ *and* $\lambda_{Hhh}$ *due to mixing effects for* $A = \mu = 1$ *TeV.*

boson couplings [23]:

$$\begin{array}{lllll} \text{double Higgs-strahlung:} & e^+e^- \to ZH_iH_j & \text{and} & ZAA & [H_{i,j} = h, H] \\ \text{triple Higgs production:} & e^+e^- \to AH_iH_j & \text{and} & AAA & \\ WW \text{ fusion} \qquad : & e^+e^- \to \bar{\nu}_e\nu_e H_iH_j & \text{and} & \bar{\nu}_e\nu_e AA & \end{array} \tag{5.2}$$

Table 5.1 shows which trilinear couplings are involved in the various processes, cf. Fig. 5.5. If all cross sections would yield sufficiently high signal rates, the system could be solved for all $\lambda$'s up to discrete ambiguities by using the double Higgs-strahlung and the triple Higgs production processes $Ahh$ and $AAA$ [”bottom-up-approach”]. The processes $ZAA$ and $AAA$ can be used to solve for the couplings $\lambda(hAA)$ and $\lambda(HAA)$. The processes $Zhh$ and $Ahh$ provide the couplings $\lambda(hhh)$ and $\lambda(Hhh)$. Subsequently the process $ZHh$ can be exploited to extract the coupling $\lambda(HHh)$ and finally $ZHH$ for the determination of $\lambda(HHH)$ The remaining triple Higgs production processes $AHh$ and $AHH$ provide additional redundant information.

In practice, not all the cross sections can be measured experimentally since some are too small. In this case, however, one can compare the theoretical predictions of the cross sections with the experimental results for the accessible channels and by this means test the trilinear Higgs couplings stringently [”top-down approach”].

In the MSSM, the couplings involving a CP-odd Higgs boson pair, *i.e.* $\lambda(hAA)$ and $\lambda(HAA)$, are small. The analysis can then be carried out without making use of the processes $ZAA$ and $AAA$. [The validity of this approach can be checked experimentally in a model-independent way: Assuming the knowledge of the predetermined couplings between gauge and Higgs bosons the measurement of $\sigma(ZAA)$ and $\sigma(AAA)$ provides an upper bound on $\lambda_{hAA}$ and $\lambda_{HAA}$.] The processes $ZH_iH_j$ and $Ahh$ are then sufficient to solve for the couplings among the neutral CP-even Higgs bosons in the manner described above, c.f. the double Higgs-strahlung: $e^+e^- \to ZH_iH_j$, $ZAA$ $[H_{i,j} = h, H]$

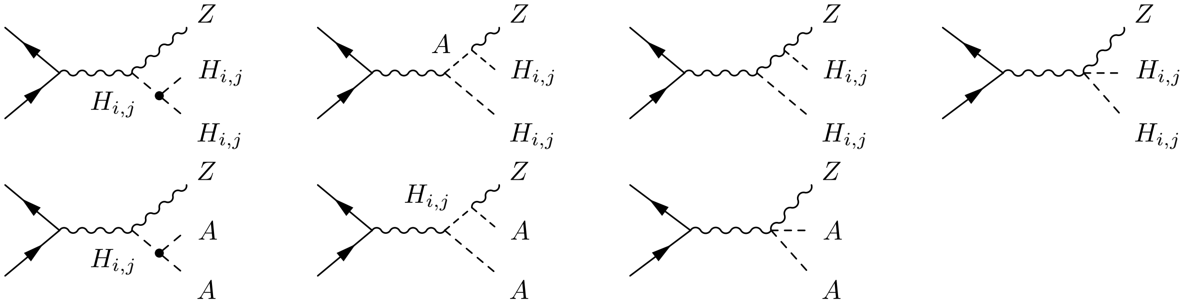

triple Higgs production: $e^+e^- \to AH_iH_j$, $AAA$

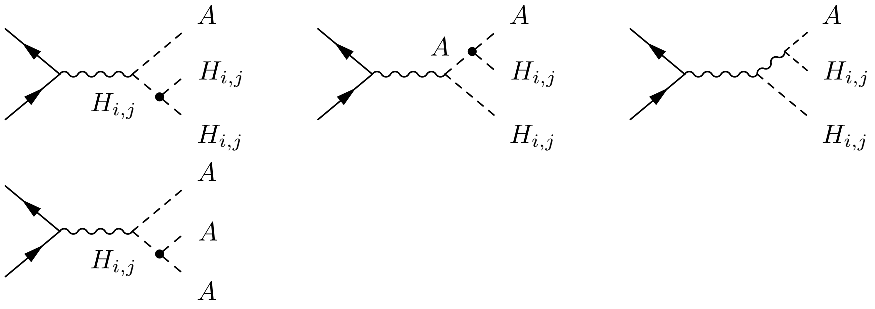

$WW$ fusion: $e^+e^- \to \bar{\nu}_e\nu_e H_iH_j$, $AA$

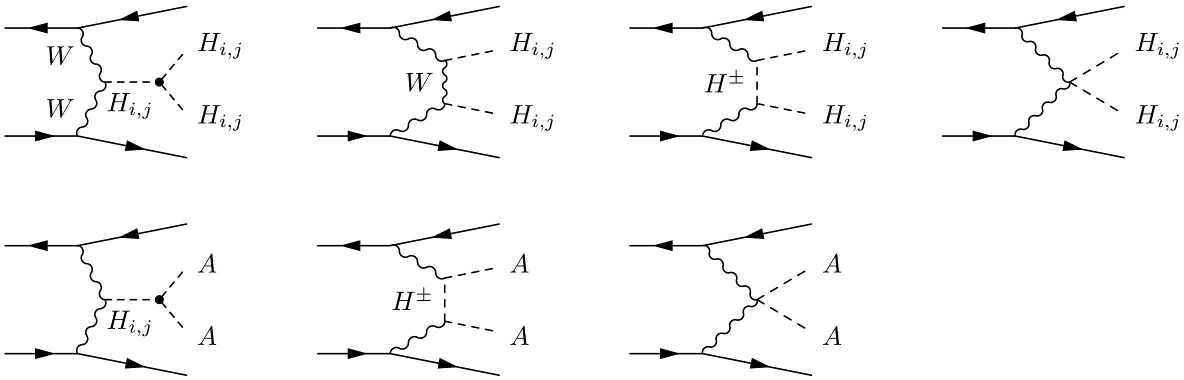

Figure 5.5: *Processes contributing to double and triple Higgs production involving trilinear couplings in the MSSM.*

| | double Higgs−strahlung | | | | triple Higgs−production | | | |
|---|---|---|---|---|---|---|---|---|
| $\lambda$ | $Zhh$ | $ZHh$ | $ZHH$ | $ZAA$ | $Ahh$ | $AHh$ | $AHH$ | $AAA$ |
| $hhh$ | × | | | | × | | | |
| $Hhh$ | × | × | | | × | × | | |
| $HHh$ | | × | × | | | × | × | |
| $HHH$ | | | × | | | | × | |
| $hAA$ | | | | × | × | × | | × |
| $HAA$ | | | | × | | × | × | × |

Table 5.1: *The trilinear couplings between neutral CP-even and CP-odd MSSM Higgs bosons which can generically be probed in double Higgs-strahlung and associated triple Higgs-production, are marked by a cross. [The matrix for WW fusion is isomorphic to the matrix for Higgs-strahlung.]*

double-line box of Table 5.1.

The processes $e^+e^- \to ZH_iA$ and $e^+e^- \to \bar{\nu}_e\nu_e H_iA$ $[H_i = h, H]$ with a CP even-odd Higgs pair in the final state cannot be used to extract the trilinear Higgs self-couplings. They are mediated by a virtual $Z$ boson which subsequently decays into a parity-mixed final state $Z^* \to H_iA$. Hence, they only involve gauge interactions and no Higgs boson self-interactions.

### 5.1.1 SM double-Higgs production in $e^+e^-$ collisions

The (unpolarized) differential cross section for the double Higgs-strahlung process $e^+e^- \to ZHH$, cf. Fig. 5.1, can be cast into the form [23]

$$\frac{d\sigma(e^+e^- \to ZHH)}{dx_1 dx_2} = \frac{\sqrt{2}G_F^3 M_Z^6}{384\pi^3 s}\frac{v_e^2 + a_e^2}{(1-\mu_Z)^2}\,\mathcal{Z} \tag{5.3}$$

after the angular dependence has been integrated out. The vector and axial-vector $Z$ charges of the electron are defined by $v_e = -1 + 4\sin^2\theta_W$ and $a_e = -1$. $x_{1,2} = 2E_{1,2}/\sqrt{s}$ are the scaled energies of the two Higgs particles, $x_3 = 2 - x_1 - x_2$ is the scaled energy of the $Z$ boson, and $y_i = 1 - x_i$; the square of the reduced masses is denoted by $\mu_i = M_i^2/s$, and $\mu_{ij} = \mu_i - \mu_j$. In terms of these variables, the coefficient $\mathcal{Z}$ can be written as:

$$\mathcal{Z} = \mathfrak{a}^2 f_0 + \frac{1}{4\mu_Z(y_1 + \mu_{HZ})}\left[\frac{f_1}{y_1 + \mu_{HZ}} + \frac{f_2}{y_2 + \mu_{HZ}} + 2\mu_Z\mathfrak{a}f_3\right] + \left\{y_1 \leftrightarrow y_2\right\} \tag{5.4}$$

with

$$\mathfrak{a} = \frac{\lambda_{HHH}}{y_3 - \mu_{HZ}} + \frac{2}{y_1 + \mu_{HZ}} + \frac{2}{y_2 + \mu_{HZ}} + \frac{1}{\mu_Z} \tag{5.5}$$

The coefficients $f_i$ are given by

$$f_0 \;=\; \mu_Z[(y_1 + y_2)^2 + 8\mu_Z]/8$$

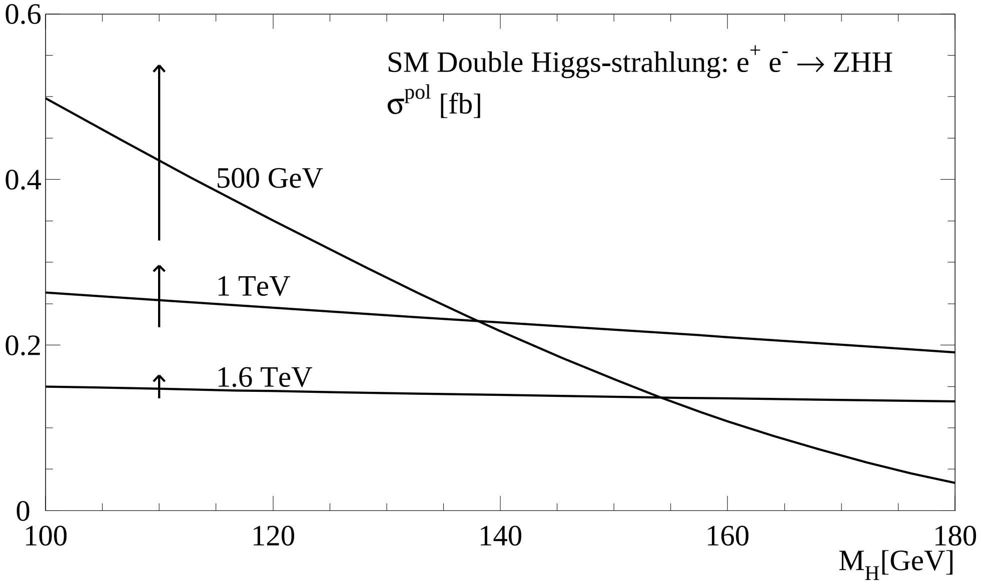

Figure 5.6: *The cross section for double Higgs-strahlung in the SM at three collider energies:* 500 *GeV,* 1 *TeV and* 1.6 *TeV. The electron/positron beams are taken oppositely polarized. The vertical arrows correspond to a variation of the trilinear Higgs coupling from* 1/2 *to* 3/2 *of the SM value.*

$$\begin{aligned}
f_1 &= (y_1-1)^2(\mu_Z-y_1)^2 - 4\mu_H y_1(y_1+y_1\mu_Z-4\mu_Z) \\
&\quad + \mu_Z(\mu_Z-4\mu_H)(1-4\mu_H) - \mu_Z^2 \\
f_2 &= [\mu_Z(y_3+\mu_Z-8\mu_H)-(1+\mu_Z)y_1y_2](1+y_3+2\mu_Z) \\
&\quad + y_1y_2[y_1y_2+1+\mu_Z^2+4\mu_H(1+\mu_Z)] + 4\mu_H\mu_Z(1+\mu_Z+4\mu_H)+\mu_Z^2 \\
f_3 &= y_1(y_1-1)(\mu_Z-y_1) - y_2(y_1+1)(y_1+\mu_Z) + 2\mu_Z(1+\mu_Z-4\mu_H) \qquad (5.6)
\end{aligned}$$

The first term in the coefficient $\mathfrak{a}$ involves the trilinear Higgs self-coupling. The other terms are due to sequential Higgs-strahlung and due to the 4-Higgs-gauge-coupling. The various terms can be identified by analysing the propagators they are associated with.

The double Higgs-strahlung process is mediated by an s-channel $Z$ boson. Since $Z$ has spin one it only couples to a left-handed electron and a right-handed positron and vice versa. Due to CP-invariance the total cross section for double Higgs-strahlung therefore doubles if electron-positron beams with opposite polarization are used.

Fig. 5.6 shows the total cross section of double Higgs-strahlung as a function of the Higgs mass for three typical $e^+e^-$ collider energies, *i.e.* $\sqrt{s} = 500$ GeV, 1 TeV and 1.6 TeV. The electron-positron beams are taken oppositely polarized $[\lambda_{e^-}\lambda_{e^+} = -1]$ so that the cross section is enhanced by a factor two. Due to the s-channel $Z$ boson propagator, the cross sections show scaling behaviour beyond the threshold region. The arrows indicate the modifications of the cross sections with a variation of the trilinear Higgs coupling from 1/2 to 3/2 in units of the SM coupling. They increase with rising coupling. Fig. 5.7 illustrates the sensitivity to $\lambda_{HHH}$ if the coupling is varied in the range $[-\lambda_{HHH}, 2\lambda_{HHH}]$. Evidently, the sensitivity of the double Higgs-strahlung process to the value of the Higgs self-coupling is not washed out by the irreducible background diagrams which do not involve $\lambda_{HHH}$. The influence of these diagrams increases with rising energy so that the sensitivity to the trilinear coupling is

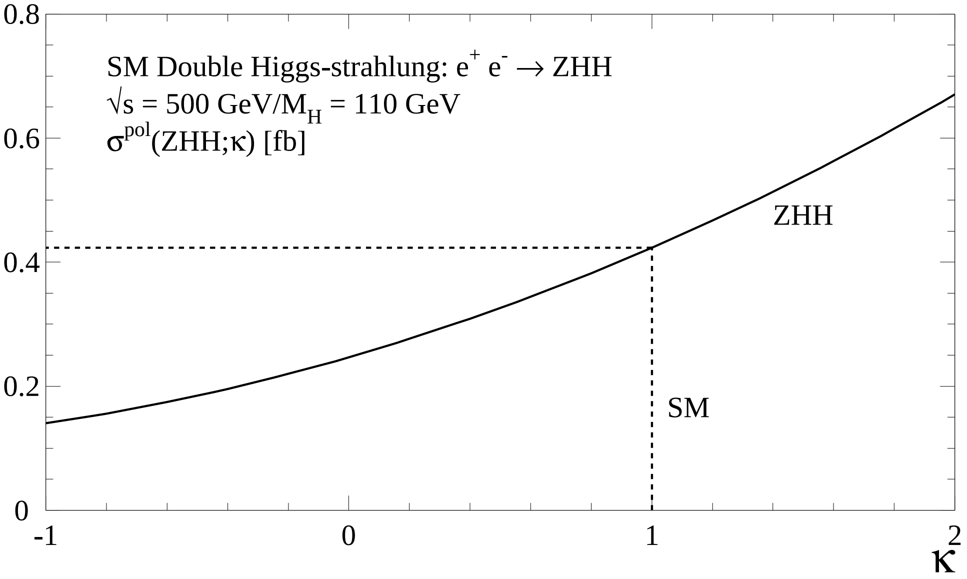

Figure 5.7: *Variation of the cross section $\sigma(ZHH)$ with the modified trilinear coupling $\kappa\lambda_{HHH}$ at a collider energy of $\sqrt{s} = 500$ GeV and $M_H = 110$ GeV.*

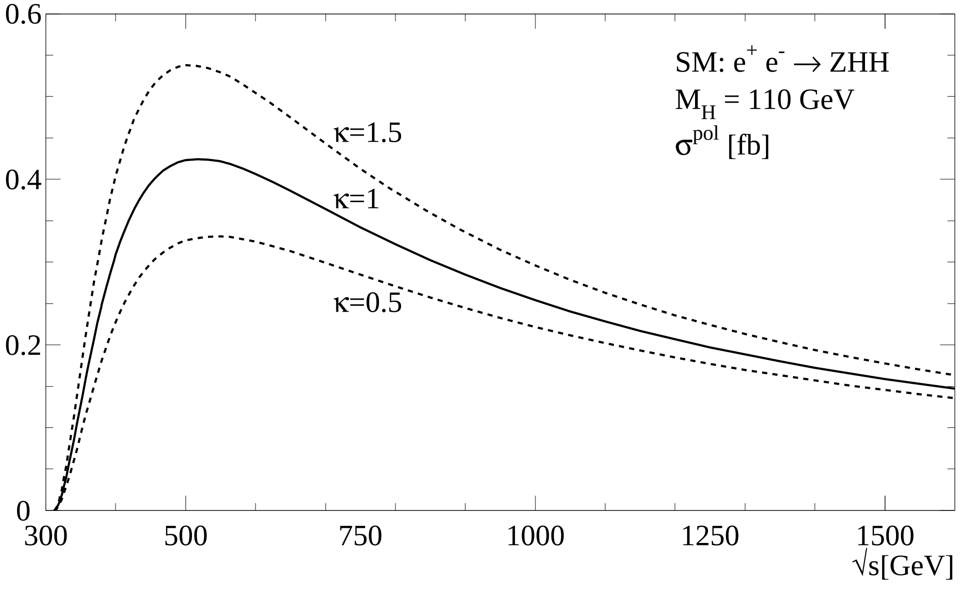

Figure 5.8: *The energy dependence of the cross section for double Higgs-strahlung for a fixed Higgs mass $M_H = 110$ GeV. The variation of the cross section for modified trilinear couplings $\kappa\lambda_{HHH}$ is indicated by the dashed lines.*

largest near the kinematic threshold as can be inferred form Fig. 5.8. This behaviour results from the propagator of the virtual Higgs boson connecting the two real Higgs bosons which is maximal near the threshold. Furthermore Fig. 5.8 shows that the maximum double Higgs-strahlung cross section is reached for energies $\sqrt{s} \sim 2M_H + M_Z + 200$ GeV, *i.e.* $\sqrt{s} = 500$ GeV for Higgs masses in the lower part of the intermediate range. A c.m. energy of 500 GeV is therefore a good choice in this mass range since the cross section as well as the sensitivity to $\lambda_{HHH}$ is maximal.

### 5.1.2 SM $WW$ double-Higgs fusion

For high energies the logarithmic behaviour of the $t$-channel diagram contributing to the $WW$ fusion process, cf. Fig. 5.1, dominates over the scaling behaviour due to the $Z$ boson propagator in the s-channel of the double Higgs-strahlung process. Therefore the $WW$ double-Higgs fusion process provides the largest cross section at high c.m. energies for Higgs masses in the intermediate range, especially when the initial state beams are taken oppositely polarized.

In order to get a rough estimate of the cross section for $WW$ double-Higgs fusion the equivalent particle approximation [40, 105] can be applied. In this approximation the $W$ bosons are regarded as partons in the electron and positron, respectively, with the $W$ bosons taken on-shell. The production amplitude for the dominant longitudinal degrees of freedom is given by [92]

$$\mathcal{M}_{LL} = \frac{G_F \hat{s}}{\sqrt{2}} \left\{ (1+\beta_W^2) \left[ 1 + \frac{\lambda_{HHH}}{(\hat{s}-M_H^2)/M_Z^2} \right] + \frac{1}{\beta_W \beta_H} \left[ \frac{(1-\beta_W^4)+(\beta_W-\beta_H\cos\theta)^2}{\cos\theta - x_W} - \frac{(1-\beta_W^4)+(\beta_W+\beta_H\cos\theta)^2}{\cos\theta + x_W} \right] \right\} \tag{5.7}$$

with $\beta_{W,H}$ denoting the $W$, $H$ velocities in the c.m. frame, and $x_W = (1-2M_H^2/\hat{s})/(\beta_W\beta_H)$. $\hat{s}^{1/2}$ is the invariant energy of the $WW$ pair; $\theta$ is the Higgs production angle in the c.m. frame of $WW$. After integrating out the angular dependence the corresponding total cross section reads [23]

$$\begin{aligned}
\hat{\sigma}_{LL} &= \frac{G_F^2 M_W^4}{4\pi\hat{s}} \frac{\beta_H}{\beta_W(1-\beta_W^2)^2} \left\{ (1+\beta_W^2)^2 \left[ 1 + \frac{\lambda_{HHH}}{(\hat{s}-M_H^2)/M_Z^2} \right]^2 \right. \\
&+ \frac{16}{(1+\beta_H^2)^2 - 4\beta_H^2\beta_W^2} \left[ \beta_H^2(-\beta_H^2 x_W^2 + 4\beta_W\beta_H x_W - 4\beta_W^2) + (1+\beta_W^2-\beta_W^4)^2 \right] \\
&+ \frac{1}{\beta_W^2\beta_H^2} \left( l_W + \frac{2x_W}{x_W^2-1} \right) \Big[ \beta_H(\beta_H x_W - 4\beta_W)(1+\beta_W^2-\beta_W^4+3x_W^2\beta_H^2) \\
&\qquad\qquad + \beta_H^2 x_W(1-\beta_W^4+13\beta_W^2) - \frac{1}{x_W}(1+\beta_W^2-\beta_W^4)^2 \Big] \\
&+ \frac{2(1+\beta_W^2)}{\beta_W\beta_H} \left[ 1 + \frac{\lambda_{HHH}}{(\hat{s}-M_H^2)/M_Z^2} \right] \Big[ l_W(1+\beta_W^2-\beta_W^4-2\beta_W\beta_H x_W + \beta_H^2 x_W^2) \\
&\qquad\qquad \left. + 2\beta_H(x_W\beta_H - 2\beta_W) \Big] \right\}
\end{aligned} \tag{5.8}$$

with $l_W = \log[(x_W-1)/(x_W+1)]$. Folding $\hat{\sigma}_{LL}$ with the longitudinal $W_L$ spectra [40, 105],

$$f_L(z) = \frac{G_F M_W^2}{2\sqrt{2}\pi^2} \frac{1-z}{z} \qquad [z = E_W/E_e] \tag{5.9}$$

| $\sigma$ [fb] | | $WW$ | $ZZ$ |
|---|---|---|---|
| $\sqrt{s} = 1$ TeV | $M_H = 110$ GeV | 0.104 | 0.013 |
| | 150 GeV | 0.042 | 0.006 |
| | 190 GeV | 0.017 | 0.002 |
| $\sqrt{s} = 1.6$ TeV | $M_H = 110$ GeV | 0.334 | 0.043 |
| | 150 GeV | 0.183 | 0.024 |
| | 190 GeV | 0.103 | 0.013 |

Table 5.2: *Total cross sections for SM pair production in $WW$ and $ZZ$ fusion at $e^+e^-$ colliders for two characteristic energies and masses in the intermediate range (unpolarized beams).*

a rough estimate of the cross section for the process $e^+e^- \to WW \to HH\bar{\nu}_e\nu_e$ can be obtained. Though the value of the exact calculation is overestimated by a factor 2 to 5, depending on the collider energy, the approximated cross section is helpful for a transparent interpretation of the exact result.

For high energies the cross section is dominated by the $t$-channel exchange which does not include the trilinear Higgs self-coupling. The convoluted $WW$ fusion process $e^+e^- \to HH\bar{\nu}_e\nu_e$ nevertheless remains sensitive to $\lambda_{HHH}$ because the major contribution to the cross section stems from the lower end of the $WW$ spectrum so that also in the high-energy limit the sensitivity to the Higgs self-coupling is maintained.

In the subsequent analysis the exact values for the $WW$ fusion cross sections have been used with the $W$ bosons being off-shell and the transverse degrees of freedom included. The cross sections have been calculated numerically with the semi-analytical CompHEP program [106]. The electron-positron beams are taken oppositely polarized thus enhancing the cross section by a factor four since the $W^-$ boson only couples to left-handed electrons. The results are shown in Fig. 5.9 for three collider energies, $\sqrt{s} = 500$ GeV, 1 TeV and 1.6 TeV, as a function of the Higgs mass. As anticipated the $WW$ fusion cross section increases with rising energy. The arrows indicate the modification of the cross sections due to the variation of the Higgs self-coupling from $1/2\lambda_{HHH}$ to $3/2\ \lambda_{HHH}$. Fig. 5.10 shows the variation of the cross section with $\kappa\lambda$, $\kappa = -1$ to 2. Due to destructive interference with the gauge diagrams the cross section decreases with rising $\lambda_{HHH}$. As expected the sensitivity to a variation of the Higgs self-coupling is smaller for high c.m. energies.

The cross sections for $ZZ$ fusion are not shown because they are an order of magnitude below the $WW$ fusion values as can be inferred from Table 5.2. This is due to the smallness of the $Ze^+e^-$ coupling.

The preceding discussion shows that for moderate energies double Higgs-strahlung $e^+e^- \to ZHH$ is the preferred channel for measurements of the trilinear Higgs-self couplings whereas for energies in the TeV range $WW$ double Higgs fusion $e^+e^- \to WW \to HH\bar{\nu}_e\nu_e$ is the more suitable channel. Since for both processes the cross sections are nevertheless small high luminosities as foreseen for $e^+e^-$ linear colliders are needed. A further enhancement

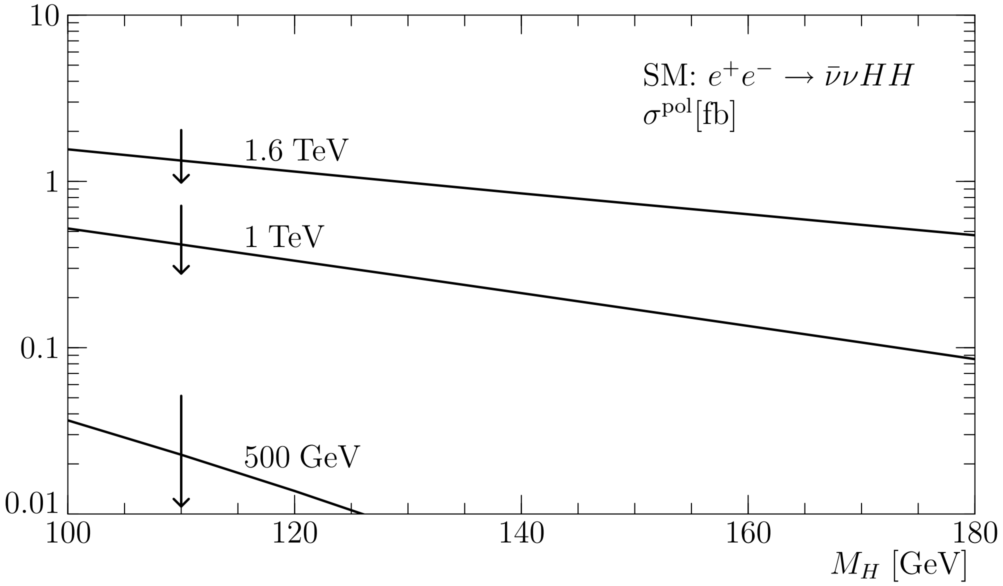

Figure 5.9: *The total cross section for WW double-Higgs fusion in the SM at three collider energies:* 500 *GeV,* 1 *TeV and* 1.6 *TeV. The vertical arrows correspond to a variation of the trilinear Higgs coupling from* 1/2 *to* 3/2 *of the SM value.*

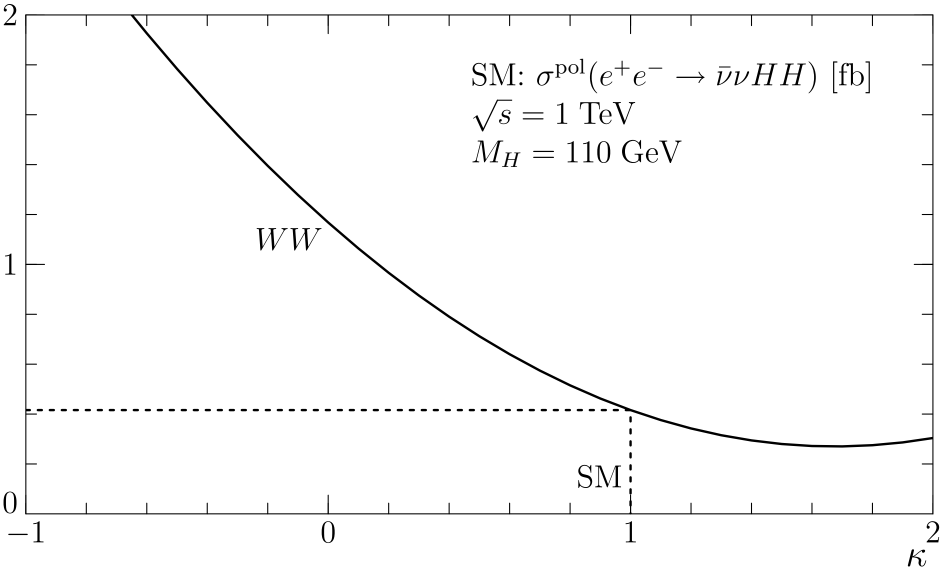

Figure 5.10: *Variation of the cross section* $\sigma(e^+e^- \longrightarrow \bar{\nu}_e\nu_e HH)$ *with the modified trilinear coupling* $\kappa\lambda_{HHH}$ *at a collider energy of* $\sqrt{s} = 1$ *TeV and* $M_H = 110$ *GeV.*

| | | $\sigma(e^+e^- \to ZHHH)$[ab] |
|---|---|---|
| $\sqrt{s}=1$ TeV | $M_H=110$ GeV | 0.44 [0.41/ 0.46] |
| | 150 GeV | 0.34 [0.32/ 0.36] |
| | 190 GeV | 0.19 [0.18/ 0.20] |
| $\sqrt{s}=1.6$ TeV | $M_H=110$ GeV | 0.30 [0.29/ 0.32] |
| | 150 GeV | 0.36 [0.34/ 0.39] |
| | 190 GeV | 0.39 [0.36/ 0.43] |

Table 5.3: *Representative values for triple SM Higgs-strahlung (unpolarized beams). The sensitivity to the quadrilinear coupling is illustrated by the variation of the cross sections when* $\lambda_{HHHH}$ *is altered by factors* 1/2 *and* 3/2*, as indicated in the square brackets.*

of a factor two for Higgs-strahlung and four for $WW$ fusion can be achieved by taking the electron-positron beams oppositely polarized. Clear multi-$b$ signatures like $e^+e^- \to Z(b\bar{b})(b\bar{b})$ and $e^+e^- \to (b\bar{b})(b\bar{b}) + \not{E}$ will enable the separation of the signal from the background. Experimental simulations taking into account detector properties have demonstrated that for Higgs masses in the intermediate range and an integrated luminosity of $\int \mathcal{L} = 500$ fb$^{-1}$ the trilinear Higgs coupling may be determined with 20% accuracy [107].

For the reconstruction of the Higgs potential also the quadrilinear Higgs self-coupling has to be determined. This coupling can in principle be measured directly in triple Higgs production: $e^+e^- \to ZHHH$ and $e^+e^- \to HHH\bar{\nu}_e\nu_e$. Yet, these cross sections are reduced by three orders of magnitude with respect to the corresponding double Higgs production cross sections. This is due to the suppression of the quadrilinear coupling compared to the trilinear coupling and due to the additional particle in the final state so that the total signal cross section is reduced by a factor $[\lambda^2_{HHHH}\lambda_0^4/16/\pi^2]/[\lambda^2_{HHH}\lambda_0^2/M_Z^2] \sim 10^{-3}$. Likewise, the irreducible background diagrams are suppressed. A few exemplifying results are given in Table 5.3.

### 5.1.3 Double and triple Higgs production in the MSSM

In the MSSM the following trilinear self-couplings arise among the neutral Higgs bosons

$hhh$, $Hhh$, $HHh$, $HHH$
$hAA$, $HAA$

There are many more quadrilinear couplings [84]. The double and triple Higgs production processes and the trilinear couplings involved are listed in Table 5.1. Since in most of the MSSM parameter space the Higgs bosons $H$ and $A$ are heavy the emphasis of the subsequent analysis will be on the production of a light Higgs boson pair with heavy Higgs boson final states taken into account where necessary.

In contrast to the SM, the resonant production of a heavy Higgs boson $H$ that subsequently decays into a light Higgs boson pair is possible. The resonant production is important in part of the parameter space with $H$ masses between 200 and 350 GeV and for moderate values of $\tan\beta$ [70]. In this case the branching ratio obtained from the partial width

$$\Gamma(H \to hh) = \frac{\sqrt{2}G_F M_Z^4 \beta_h}{32\pi M_H} \lambda_{Hhh}^2 \tag{5.10}$$

is neither too small nor too close to unity to be accessible directly. The resonant $H$ decay enhances the total production cross section for $hh$ by an order of magnitude [23] thus improving the potential for the measurement of the Higgs self-coupling $\lambda_{Hhh}$. Apart from the exceptional case of a light pseudoscalar Higgs boson $A$ the coupling $\lambda_{Hhh}$ is the only trilinear Higgs self-coupling which is accessible via resonant decay. All the other couplings have to be extracted from the continuum pair production. The generic diagrams contributing to double and triple Higgs production and $WW$ double Higgs fusion have been shown in Fig. 5.5.

### 5.1.4 MSSM double Higgs-strahlung

The (unpolarized) production cross section for a pair of light Higgs bosons via Higgs-strahlung in the MSSM has the same structure as in the SM yet involving $H$ and $A$ exchange diagrams [23, 83, 104], cf. Fig. 5.5:

$$\frac{d\sigma(e^+e^- \to Zhh)}{dx_1 dx_2} = \frac{\sqrt{2}G_F^3 M_Z^6}{384\pi^3 s} \frac{v_e^2 + a_e^2}{(1-\mu_Z)^2} \mathcal{Z}_{11} \tag{5.11}$$

with

$$\begin{aligned}
\mathcal{Z}_{11} \;=\; & \mathfrak{a}^2 f_0 + \frac{\mathfrak{a}}{2}\left[\frac{\sin^2(\beta-\alpha) f_3}{y_1 + \mu_{1Z}} + \frac{\cos^2(\beta-\alpha) f_3}{y_1 + \mu_{1A}}\right] \\
& + \frac{\sin^4(\beta-\alpha)}{4\mu_Z (y_1 + \mu_{1Z})}\left[\frac{f_1}{y_1 + \mu_{1Z}} + \frac{f_2}{y_2 + \mu_{1Z}}\right] \\
& + \frac{\cos^4(\beta-\alpha)}{4\mu_Z (y_1 + \mu_{1A})}\left[\frac{f_1}{y_1 + \mu_{1A}} + \frac{f_2}{y_2 + \mu_{1A}}\right] \\
& + \frac{\sin^2 2(\beta-\alpha)}{8\mu_Z (y_1 + \mu_{1A})}\left[\frac{f_1}{y_1 + \mu_{1Z}} + \frac{f_2}{y_2 + \mu_{1Z}}\right] + \left\{ y_1 \leftrightarrow y_2 \right\}
\end{aligned} \tag{5.12}$$

and

$$\mathfrak{a} = \left[\frac{\lambda_{hhh}\sin(\beta-\alpha)}{y_3 - \mu_{1Z}} + \frac{\lambda_{Hhh}\cos(\beta-\alpha)}{y_3 - \mu_{2Z}}\right] + \frac{2\sin^2(\beta-\alpha)}{y_1 + \mu_{1Z}} + \frac{2\sin^2(\beta-\alpha)}{y_2 + \mu_{1Z}} + \frac{1}{\mu_Z} \tag{5.13}$$

The notation is the same as in the Standard Model, with $\mu_1 = M_h^2/s$ and $\mu_2 = M_H^2/s$. Taking into account that in part of the parameter space the heavy neutral Higgs boson $H$ or the pseudoscalar Higgs boson $A$ may become resonant, the decay widths are included implicitly by shifting the masses to complex values $M \to M - i\Gamma/2$, *i.e.* $\mu_i \to \mu_i - i\gamma_i$ with the reduced width $\gamma_i = M_i\Gamma_i/s$, and by replacing products of propagators $\pi_1\pi_2$ with $\mathrm{Re}(\pi_1\pi_2^*)$.

Fig. 5.11 shows the total polarized cross section $Zhh$ for $\sqrt{s} = 500$ GeV as a function of the Higgs masses. The mixing parameters are chosen $A = 1$ TeV and $\mu = -1(1)$ TeV for $\tan\beta = 3(50)$. Choosing $\tan\beta$ and $M_h$ as input parameters the masses of the heavy Higgs bosons are fixed in the MSSM for given values of the mixing parameters [70]. As can be inferred from Fig. 5.11 the continuum cross section is smaller compared to the SM

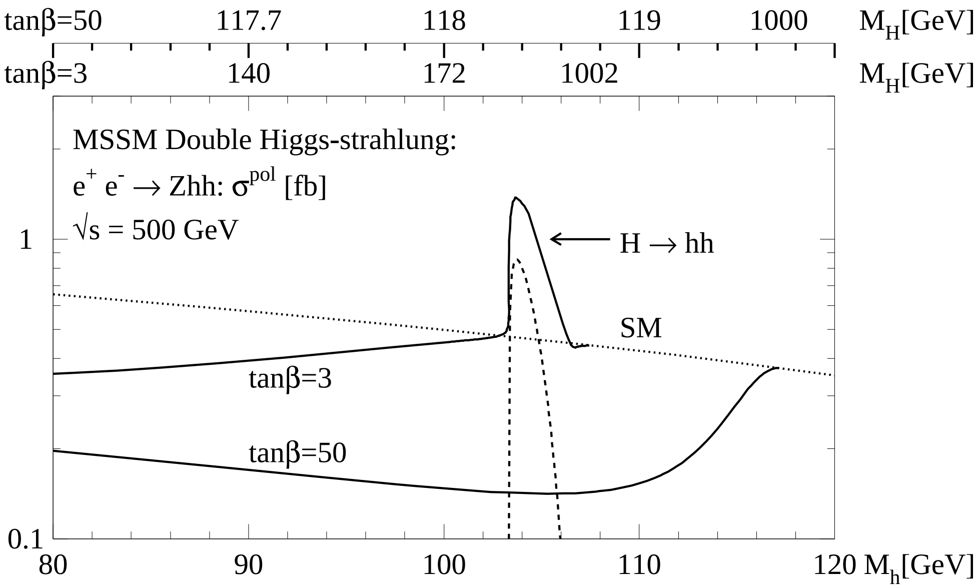

Figure 5.11: *Total cross sections for MSSM hh production via double Higgs-strahlung at $e^+e^-$ linear colliders for* $\tan\beta = 3$, $50$ *and* $\sqrt{s} = 500$ GeV, *including mixing effects [$A = 1$ TeV, $\mu = -1/1$ TeV for* $\tan\beta = 3/50$*]. The dotted line indicates the SM cross section. The dashed line represents the resonant contribution.*

result. This originates from the suppression of the MSSM vertices by sin / cos functions of the mixing angles $\alpha$ and $\beta$. In contrast, the cross section is enhanced by an order of magnitude when resonant $H$ production with subsequent decay $H \to hh$ is kinematically possible. Approaching the maximum value of $M_h$ for $\tan\beta$ fixed, $H$ and $A$ become very heavy and decouple so that the MSSM $Zhh$ cross section reaches the SM value. Due to the decoupling theorem resonant $H$ production does not increase the MSSM cross section for large values of $\tan\beta$ since the decay $H \to hh$ is kinematically not possible unless the decoupling region is reached where the $ZZH$ coupling is too small to produce a sizeable cross section.

The formulae for the Higgs-strahlung processes $ZH_iH_j$ $[H_i, H_j = h, H]$ are deferred to the Appendix. They are more complicated due to the different masses of the final state Higgs particles. The corresponding polarized cross sections are shown together with the SM cross section as a function of $M_h$ in Fig. 5.12. The c.m. energy is chosen equal to 500 GeV and $\tan\beta = 3$. Evidently, if kinematically possible, the cross sections $Zhh$, $ZHh$ and $ZHH$ add up approximately to the SM result.

### 5.1.5 Triple Higgs production

The processes $e^+e^- \to ZH_i$ and $e^+e^- \to AH_i$ are proportional to $\sin^2(\beta-\alpha)/\cos^2(\beta-\alpha)$ and $\cos^2(\beta-\alpha)/\sin^2(\beta-\alpha)$ for $H_i = h, H$, respectively, so that Higgs-strahlung and associated Higgs production are complementary to each other. In addition the processes are among themselves complementary [44]. Since the double and triple Higgs production processes $ZH_iH_j$, $ZAA$ and $AH_iH_j$, $AAA$ proceed via virtual $h, H$ bosons this behaviour will be found there, too, being of more complex matrix form, however, since the combination of

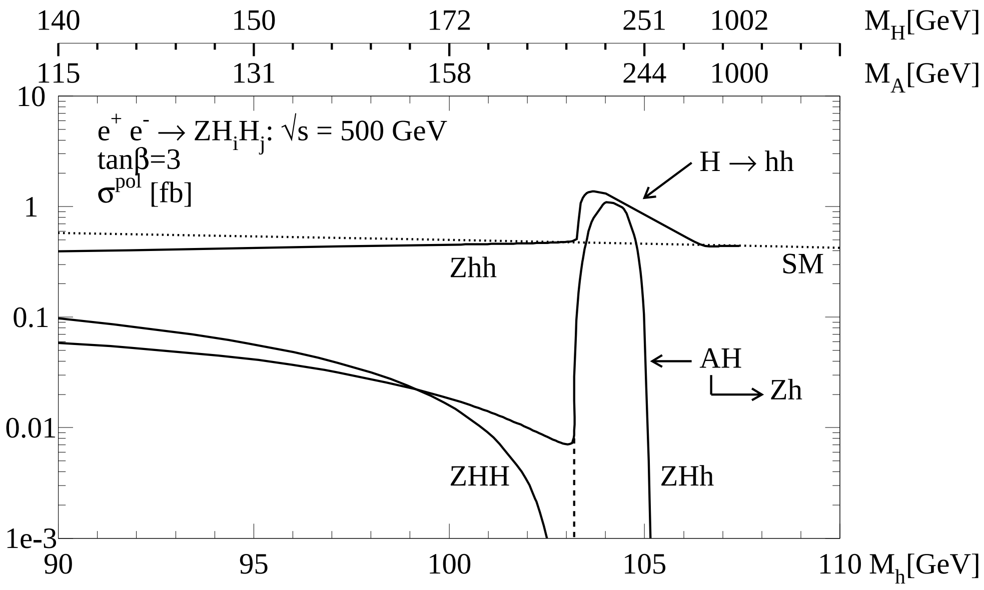

Figure 5.12: *Cross sections for the processes* $Zhh$, $ZHh$ *and* $ZHH$ *for* $\sqrt{s} = 500$ *GeV and* $tan\beta = 3$, *including mixing effects* ($A = 1$ *TeV*, $\mu = -1$ *TeV*).

the different mechanisms is more involved, cf. Fig. 5.5. In this subsection the processes $e^+e^- \to Ahh$ and $e^+e^- \to AAA$ will be discussed in more detail. The more complicated results for triple Higgs production involving heavy Higgs bosons are listed in the Appendix.

The unpolarized cross section for $e^+e^- \to Ahh$ is given by

$$\frac{d\sigma[e^+e^- \to Ahh]}{dx_1 dx_2} = \frac{G_F^3 M_Z^6}{768\sqrt{2}\pi^3 s} \frac{v_e^2 + a_e^2}{(1-\mu_Z)^2} \mathfrak{A}_{11} \tag{5.14}$$

where the function $\mathfrak{A}_{11}$ can be cast into the form

$$\begin{aligned}
\mathfrak{A}_{11} &= \left[\frac{c_1\lambda_{hhh}}{y_3-\mu_{1A}} + \frac{c_2\lambda_{Hhh}}{y_3-\mu_{2A}}\right]^2 \frac{g_0}{2} + \frac{c_1^2\lambda_{hAA}^2}{(y_1+\mu_{1A})^2} g_1 + \frac{c_1^2 d_1^2}{(y_1+\mu_{1Z})^2} g_2 \\
&+ \left[\frac{c_1\lambda_{hhh}}{y_3-\mu_{1A}} + \frac{c_2\lambda_{Hhh}}{y_3-\mu_{2A}}\right] \left[\frac{c_1\lambda_{hAA}}{y_1+\mu_{1A}} g_3 + \frac{c_1 d_1}{y_1+\mu_{1Z}} g_4\right] \\
&+ \frac{c_1^2\lambda_{hAA}^2}{2(y_1+\mu_{1A})(y_2+\mu_{1A})} g_5 + \frac{c_1^2 d_1 \lambda_{hAA}}{(y_1+\mu_{1A})(y_1+\mu_{1Z})} g_6 \\
&+ \frac{c_1^2 d_1 \lambda_{hAA}}{(y_1+\mu_{1A})(y_2+\mu_{1Z})} g_7 + \frac{c_1^2 d_1^2}{2(y_1+\mu_{1Z})(y_2+\mu_{1Z})} g_8 \\
&+ \left\{ y_1 \leftrightarrow y_2 \right\}
\end{aligned} \tag{5.15}$$

with $\mu_{1,2} = M_{h,H}^2/s$ and the vertex coefficients

$$c_1/c_2 = \cos(\beta-\alpha)/-\sin(\beta-\alpha) \qquad \text{and} \qquad d_1/d_2 = \sin(\beta-\alpha)/\cos(\beta-\alpha) \tag{5.16}$$

The coefficients $g_k$ are given by

$$g_0 = \mu_Z[(y_1+y_2)^2 - 4\mu_A]$$

$$\begin{aligned}
g_1 &= \mu_Z[y_1^2-2y_1-4\mu_1+1]\\
g_2 &= \mu_Z[y_1(y_1+2)+4y_2(y_2+y_1-1)+1-4(\mu_1+2\mu_A)]+(\mu_1-\mu_A)^2\\
&\quad [8+[(1-y_1)^2-4\mu_1]/\mu_Z]+(\mu_1-\mu_A)[4y_2(1+y_1)+2(y_1^2-1)]\\
g_3 &= 2\mu_Z(y_1^2-y_1+y_2+y_1y_2-2\mu_A)\\
g_4 &= 2\mu_Z(y_1^2+y_1+2y_2^2-y_2+3y_1y_2-6\mu_A)\\
&\quad +2(\mu_1-\mu_A)(y_1^2-y_1+y_2+y_1y_2-2\mu_A)\\
g_5 &= 2\mu_Z(y_1+y_2+y_1y_2+4\mu_1-2\mu_A-1)\\
g_6 &= 2\mu_Z(y_1^2+2y_1y_2+2y_2+4\mu_1-4\mu_A-1)\\
&\quad +2(\mu_1-\mu_A)(y_1^2-2y_1-4\mu_1+1)\\
g_7 &= 2[\mu_Z(2y_1^2-3y_1+y_1y_2+y_2-4\mu_1-2\mu_A+1)\\
&\quad +(\mu_1-\mu_A)(y_1+y_1y_2+y_2+4\mu_1-2\mu_A-1)]\\
g_8 &= 2\left\{\mu_Z(y_1+y_2+2y_1^2+2y_2^2+5y_1y_2-1+4\mu_1-10\mu_A)\right.\\
&\quad +4(\mu_1-\mu_A)(-2\mu_1-\mu_A-y_1-y_2+1)\\
&\quad +[2(\mu_1-\mu_A)((y_1+y_2+y_1y_2+y_1^2+y_2^2-1)\mu_Z+2\mu_1^2+4\mu_A^2-\mu_1+\mu_A)\\
&\quad \left.+\,6\mu_A(\mu_A^2-\mu_1^2)+(\mu_1-\mu_A)^2(1+y_1)(1+y_2)]/\mu_Z\right\}
\end{aligned}\tag{5.17}$$

The notation of the kinematics is the same as for double Higgs-strahlung.

The cross section for triple $A$ production is much simpler since there are only a few diagrams involved in the process, cf. Fig. 5.5:

$$\frac{d\sigma[e^+e^-\to AAA]}{dx_1dx_2}=\frac{G_F^3M_Z^6}{768\sqrt{2}\pi^3 s}\frac{v_e^2+a_e^2}{(1-\mu_Z)^2}\mathfrak{A}_{33}\tag{5.18}$$

where

$$\mathfrak{A}_{33}=D_3^2g_0+D_1^2g_1+D_2^2g_1'-D_3D_1g_3-D_3D_2g_3'+D_1D_2g_5\tag{5.19}$$

and

$$D_k=\frac{\lambda_{hAA}c_1}{y_k-\mu_{1A}}+\frac{\lambda_{HAA}c_2}{y_k-\mu_{2A}}\tag{5.20}$$

The scaled mass parameter $\mu_1$ has to be replaced by $\mu_A$ in the coefficients $g_i$ and $g_i'$ where the functions $g_i'$ are related to $g_i$ via $g_i'(y_1,y_2)=g_i(y_2,y_1)$.

Fig. 5.13 shows the results for the triple Higgs production processes $e^+e^-\to Ahh$ and $e^+e^-\to AAA$ compared to double Higgs-strahlung $e^+e^-\to Zhh$ and the SM counterpart, $e^+e^-\to ZHH$. The triple Higgs processes are small in the continuum. This behaviour can be explained by analysing the effective couplings. The process $e^+e^-\to Ah_{virt}\to Ahh$ involves the coupling $\cos(\beta-\alpha)\lambda_{hhh}$ and $e^+e^-\to AH_{virt}\to Ahh$ is proportional to $\sin(\beta-\alpha)\lambda_{Hhh}$. In both cases the products of the gauge and Higgs self-coupling are small as can be inferred from Figs. 5.2 and 5.3. Only if resonant $H$ production with subsequent $H\to hh$ decay is kinematically allowed the cross section increases by about three orders of magnitude. The process $e^+e^-\to Ah_{virt}\to AAA$ exhibits the effective coupling $\cos(\beta-\alpha)\lambda_{hAA}$, one of the factors always being small, and $e^+e^-\to AH_{virt}\to AAA$ is proportional to $\sin(\beta-\alpha)\lambda_{HAA}$ with $\lambda_{HAA}$ being of order 1/2. Taking into account the reduction of the phase space due to three heavy Higgs bosons $A$ in the final state the pseudoscalar triple Higgs production process is always small.

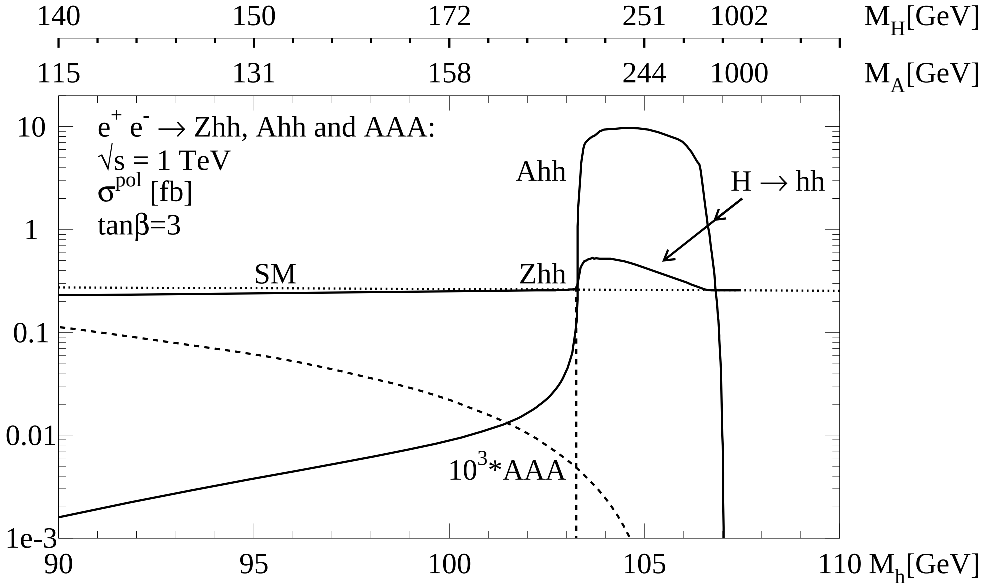

Figure 5.13: *Cross sections of the processes Zhh, Ahh and AAA for* $\tan\beta = 3$ *and* $\sqrt{s} =$ 1 *TeV, including mixing effects (*$A = 1$ *TeV,* $\mu = -1$ *TeV.)*

### 5.1.6 MSSM $WW$ double Higgs fusion

The $WW$ double Higgs fusion process in the MSSM involves also $H$ and $H^\pm$ exchange diagrams in contrast to the SM. The dominant longitudinal amplitude for on-shell $W$ bosons with a pair of light Higgs bosons in the final state is given by:

$$\begin{aligned}
\mathcal{M}_{LL} &= \frac{G_F \hat{s}}{\sqrt{2}} \Bigg\{ (1+\beta_W^2) \left[ 1 + \frac{\lambda_{hhh}\sin(\beta-\alpha)}{(\hat{s}-M_h^2)/M_Z^2} + \frac{\lambda_{Hhh}\cos(\beta-\alpha)}{(\hat{s}-M_H^2)/M_Z^2} \right] \\
&+ \frac{\sin^2(\beta-\alpha)}{\beta_W\beta_h} \left[ \frac{(1-\beta_W^4)+(\beta_W-\beta_h\cos\theta)^2}{\cos\theta - x_W} - \frac{(1-\beta_W^4)+(\beta_W+\beta_h\cos\theta)^2}{\cos\theta + x_W} \right] \\
&+ \frac{\cos^2(\beta-\alpha)}{\beta_W\beta_h} \left[ \frac{(\beta_W-\beta_h\cos\theta)^2}{\cos\theta - x_+} - \frac{(\beta_W+\beta_h\cos\theta)^2}{\cos\theta + x_+} \right] \Bigg\}
\end{aligned} \tag{5.21}$$

$\hat{s}^{1/2}$ is the c.m. energy of the subprocess, $\theta$ the scattering angle, $\beta_W$ and $\beta_h$ denote the velocities of the $W$ and $h$ bosons, and

$$x_W = \frac{1-2\mu_h}{\beta_W\beta_h} \qquad \text{and} \qquad x_+ = \frac{1-2\mu_h+2\mu_{H^\pm}-2\mu_W}{\beta_W\beta_h} \tag{5.22}$$

After integrating out the angular dependence, the total cross section of the fusion subprocess reads

$$\begin{aligned}
\hat{\sigma}_{LL} &= \frac{G_F^2 M_W^4}{4\pi\hat{s}} \frac{\beta_h}{\beta_W(1-\beta_W^2)^2} \Bigg\{ (1+\beta_W^2)^2 \left[ \frac{\lambda_{hhh} d_1}{(\hat{s}-M_h^2)/M_Z^2} + \frac{\lambda_{Hhh} d_2}{(\hat{s}-M_H^2)/M_Z^2} + 1 \right]^2 \\
&+ \frac{2(1+\beta_W^2)}{\beta_W\beta_h} \left[ \frac{\lambda_{hhh} d_1}{(\hat{s}-M_h^2)/M_Z^2} + \frac{\lambda_{Hhh} d_2}{(\hat{s}-M_H^2)/M_Z^2} + 1 \right] \left[ d_1^2 a_1^W + c_1^2 a_1^+ \right] \\
&+ \left( \frac{d_1^2}{\beta_W\beta_h} \right)^2 a_2^W + \left( \frac{c_1^2}{\beta_W\beta_h} \right)^2 a_2^+ + 4 \left( \frac{c_1^2 d_1^2}{\beta_W^2\beta_h^2} \right) \left[ a_3^W + a_3^+ \right] \Bigg\}
\end{aligned} \tag{5.23}$$

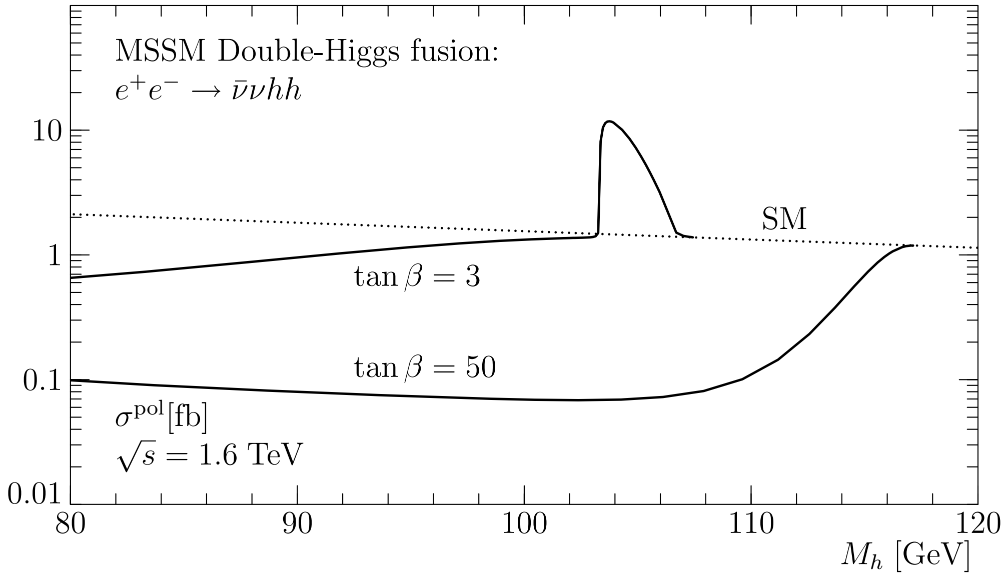

Figure 5.14: *Total cross sections for MSSM hh production via double WW double-Higgs fusion at e$^+$e$^-$ linear colliders for* $\tan\beta = 3$, $50$ *and* $\sqrt{s} = 1.6$ *TeV, including mixing effects (*$A = 1$ *TeV,* $\mu = -1/1$ *TeV for* $\tan\beta = 3/50$*).*

with

$$\begin{aligned}
a_1^W &= [(x_W\beta_h - \beta_W)^2 + r_W]l_W + 2\beta_h(x_W\beta_h - 2\beta_W) \\
a_2^W &= \left[\frac{1}{x_W}l_W + \frac{2}{x_W^2-1}\right]\Big[x_W^2\beta_h^2(3\beta_h^2x_W^2 + 2r_W + 14\beta_W^2) \\
&\quad - (\beta_W^2 + r_W)^2 - 4\beta_h\beta_W x_W(3\beta_h^2x_W^2 + \beta_W^2 + r_W)\Big] \\
&\quad - \frac{4}{x_W^2-1}\left[\beta_h^2(\beta_h^2x_W^2 + 4\beta_W^2 - 4\beta_h x_W\beta_W) - (\beta_W^2 + r_W)^2\right] \\
a_3^W &= \frac{1}{x_+^2 - x_W^2}\, l_W\Big[2\beta_W\beta_h x_W[(\beta_W^2 + x_W^2\beta_h^2)(x_W + x_+) + x_W r_W + x_+ r_+] \\
&\quad - x_+(r_+ + r_W + \beta_h^2x_W^2)(\beta_W^2 + \beta_h^2x_W^2) - \beta_W^2(x_+\beta_W^2 + 4\beta_h^2x_W^3 + x_+x_W^2\beta_h^2) \\
&\quad - x_+r_Wr_+\Big] + \beta_h^2\left[\beta_h^2x_+x_W - 2\beta_W\beta_h(x_W + x_+) + 4\beta_W^2\right] \\
a_i^+ &\equiv a_i^W\ (x_W \leftrightarrow x_+\ ,\ r_W \leftrightarrow r_+) \qquad (5.24)
\end{aligned}$$

and $r_W = 1 - \beta_W^4$, $r_+ = 0$.

The cross sections presented in Figs. 5.14 and 5.15 have been calculated exactly by means of the program CompHEP [106] without using any approximations. The electron-positron beams are taken oppositely polarized. The process involving a light Higgs bosons pair in the final state is suppressed compared to the SM unless resonance $H \to hh$ decay is possible for modest $\tan\beta$ values. In the case of large $\tan\beta$ the MSSM fusion process is much more suppressed and resonance production does not play any rôle since in this parameter range the gauge couplings involved are very small. Yet, the $H$ mass is rather light so that the processes $hh$, $Hh$ and $HH$ approximately add up to the SM cross section. The formulae for the longitudinal amplitudes $W_LW_L \to Hh, HH$ and $AA$ can be found in the Appendix.

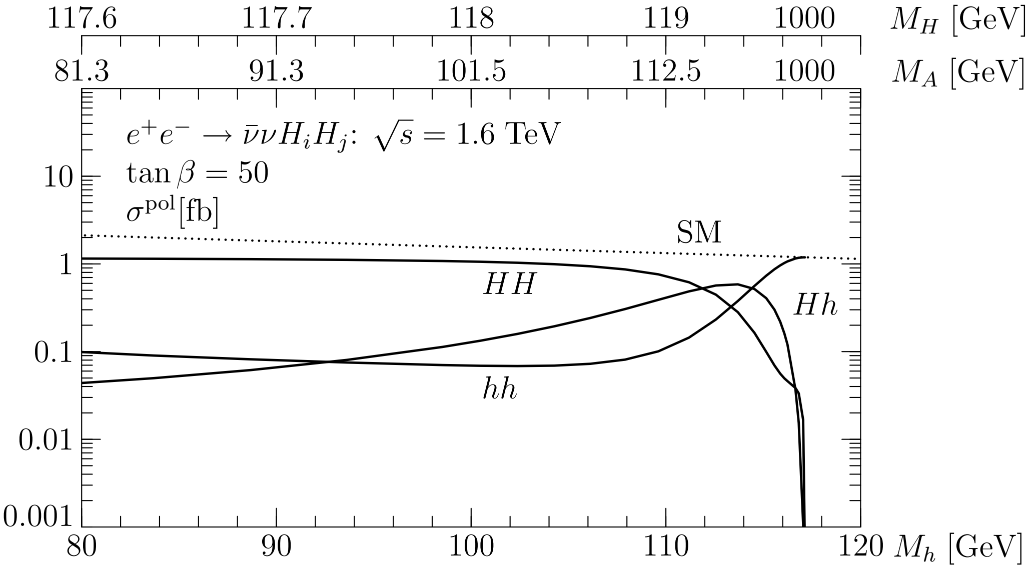

Figure 5.15: *Total cross sections for WW double-Higgs fusion with hh, Hh and HH final states for* $\sqrt{s} = 1.6$ *TeV and tan*$\beta = 50$*, including mixing effects (*$A = 1$ *TeV,* $\mu = 1$ *TeV).*

### 5.1.7 Sensitivity areas

In this subsection the perspectives for the determination of the Higgs self-couplings in the SM and the MSSM will be analysed. For the MSSM case, the feasibility of measuring the trilinear Higgs self-couplings shall be represented in compact form in sensitivity plots in the $[M_A, \tan\beta]$ plane [23, 83].

**1.) SM WW Double Higgs fusion**
Since for SM Higgs masses below 140 GeV the main decay channel is given by $H \to b\bar{b}$ the final state for the $WW$ fusion process is characterized by two $b\bar{b}$ pairs and missing energy in this mass region. Analogously, for $M_H \gtrsim 140$ GeV the final state consists of two $WW^{(*)}$ pairs and missing energy since in this case $H$ dominantly decays in $WW^{(*)}$, see Fig. 4.1. Possible background processes yielding $b\bar{b}b\bar{b} + \not{E}$ in the final state may proceed via the pure EW $WW$ fusion process being $\mathcal{O}(\alpha^6)$ or $\gamma\gamma$ fusion with a gluon exchanged between the $b$-quarks of $\mathcal{O}(\alpha^4\alpha_s^2)$ whereas the signal process is $\mathcal{O}(\alpha^4)$. Hence the $WW$ fusion background process is suppressed by $\mathcal{O}(\alpha^2)$ compared to the signal. $\gamma\gamma$ fusion results in large event rates in forward direction. In contrast the bottom quarks from the decay of the massive Higgs bosons are back-to-back. Applying appropriate angular cuts will hence help to reduce the background with respect to the signal. For $M_H \gtrsim 140$ GeV a possible background process is generated by $\gamma\gamma$ fusion being suppressed by $\mathcal{O}(\alpha^2)$ compared to the signal.

**2.) SM Double Higgs-strahlung**
In analogy to $WW$ fusion the double Higgs-strahlung process being $\mathcal{O}(\alpha^3)$ consists of a $Z$ boson and two $b\bar{b}$ pairs in the final state if $M_H \lesssim 140$ GeV and of $ZWW^{(*)}WW^{(*)}$ if $M_H \gtrsim 140$ GeV. For the low mass range signal to background analyses have been performed on parton level [99] as well as on detector level [102]. Assuming efficient $b$-tagging and high purity sampling of $b$-quarks the main background is due to irreducible EW processes of $\mathcal{O}(\alpha^5)$ and QCD backgrounds of $\mathcal{O}(\alpha^3\alpha_s^2)$. Another source is the intrinsic background

resulting from the signal diagrams which do not contain the trilinear Higgs self-coupling $\lambda_{HHH}$. The parton level analysis demonstrates that after applying typical selection cuts the signal to background ratio which may be reached for $M_H = 110$ GeV is $S/B = 25/60/140$ in the case of $\sqrt{s} = 500/1000/1500$ GeV [99]. These results are based on the assumption of a very high luminosity (chosen equal to $\int \mathcal{L} = 1$ ab$^{-1}$ in [99]), excellent $b$-tagging performances and high di-jet resolution.

Whereas the previous results have been obtained without taking into account detector effects, the analyses of Ref. [102] are based on a detector simulation and include hadronization effects. The examined final state consists of $b\bar{b}b\bar{b}q\bar{q}$, the $q\bar{q}$ pair resulting from the $Z$ boson decay. The study of the 6-jet topology demonstrates that for $M_H \sim 100$ GeV and $\int \mathcal{L} = 500$ fb$^{-1}$ a significance of 5 might be achievable, high $b$-tagging efficiency and purity provided ($\epsilon_b = 0.85$, $\epsilon_{not\,b} = 0.9$).

**3.) MSSM Double Higgs-strahlung**

For the process $Zhh$, there exists a parton level analysis of the signal to background ratio [100, 101]. The final state is given by $Zb\bar{b}b\bar{b}$ since $h$ dominantly decays into $b\bar{b}$ independent of the value of $\tan\beta$ [59, 70, 71]. A low and a high $\tan\beta$ scenario has been investigated, mixing effects included ($A = 2.4$ TeV, $\mu = 1$ TeV). After applying appropriate acceptance cuts the main background results from pure EW and EW/QCD mixed processes. Applying selection cuts according to the kinematics of the signal process, it yields 156 events for $\int \mathcal{L} = 500$ fb$^{-1}$ and $\tan\beta = 3$, $M_h = 104$ GeV. For these parameters resonant $H$ production with subsequent decay $H \to hh$ is possible. The background only amounts to a 10% correction. In the case of $\tan\beta = 50$ where no resonant production is possible and the cross section is strongly suppressed, only for Higgs masses in the decoupling limit a reasonable event rate of 15 may be achieved. The analysis does not take into account $b$-tagging efficiency and $Z$ boson decay.

The feasibility of measuring the trilinear Higgs self-couplings of the MSSM can be summarized in sensitivity plots in the $[M_A, \tan\beta]$ plane [23, 83]. The sensitivity criteria for a point in the plane to allow for the measurement of the trilinear coupling in the corresponding channel have been chosen as follows:

$$\begin{array}{ll} (i) & \sigma[\lambda] > 0.01 \text{ fb} \\ (ii) & \text{eff}\{\lambda \to 0\} > 2 \text{ st.dev.} \quad \text{for} \quad \int \mathcal{L} = 2 \text{ ab}^{-1} \end{array} \tag{5.25}$$

The first criterion demands the value of the cross section of the examined process to be larger than 0.01 fb, corresponding to at least 20 events for an integrated luminosity of $\int \mathcal{L} = 2$ ab$^{-1}$. The second condition is fulfilled if the effect of the trilinear coupling on the cross section exceeds 2 standard-deviations. (The second criterion is changed slightly where appropriate, cf. Figs. 5.16 and 5.17.) If more stringent cuts are applied the results will not change dramatically, cf. Ref. [104]. The sensitivity areas have been analysed based on the double Higgs-strahlung and triple Higgs production processes. $WW$ double Higgs fusion would provide additional information especially for higher c.m. energies. For the sake of simplicity no mixing effects have been included.

Figs. 5.16 and 5.17 show the sensitivity areas for the trilinear couplings among the neutral CP-even Higgs bosons. The c.m. energy has been chosen equal to 500 GeV for double Higgs-strahlung if at most one heavy Higgs boson is present in the final state. Otherwise $\sqrt{s} = 1$ TeV yields larger sensitivity regions. Likewise the areas for triple Higgs production involving $A$ are larger for 1 TeV. Unless interference effects become important the size of the sensitivity areas in $\tan\beta$ can be explained by analysing the values of the effective couplings

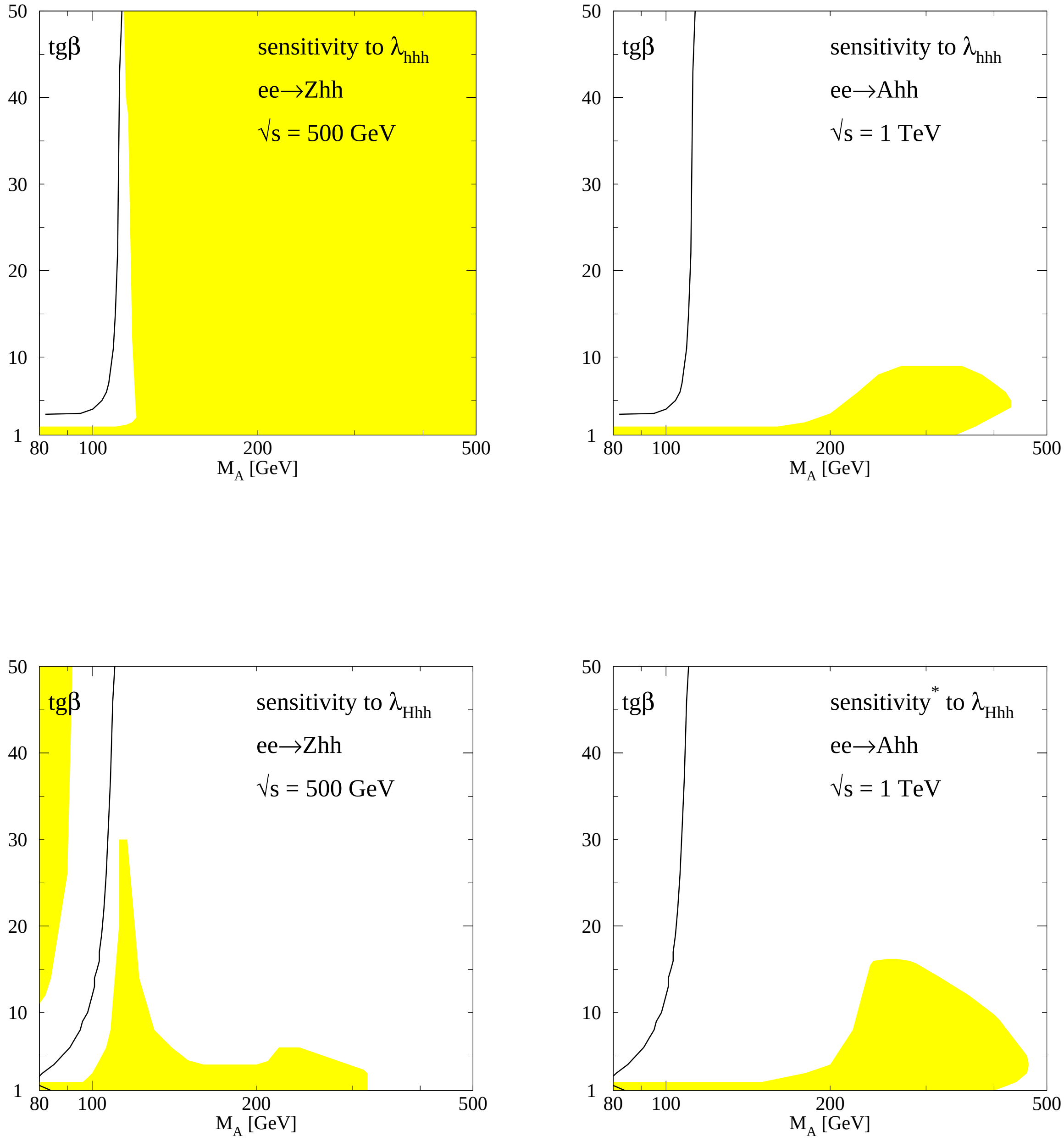

Figure 5.16: *Sensitivity [* eff*$\{\lambda \to (1 \pm \frac{1}{2})\lambda)\} > 2$*st.dev.] to the couplings* $\lambda_{hhh}$ *and* $\lambda_{Hhh}$ *in the processes* $e^+e^- \to Zhh$ *and* $e^+e^- \to Ahh$ *for collider energies* 500 *GeV and* 1 *TeV, respectively (no mixing). [Vanishing trilinear couplings are indicated by contour lines.]*

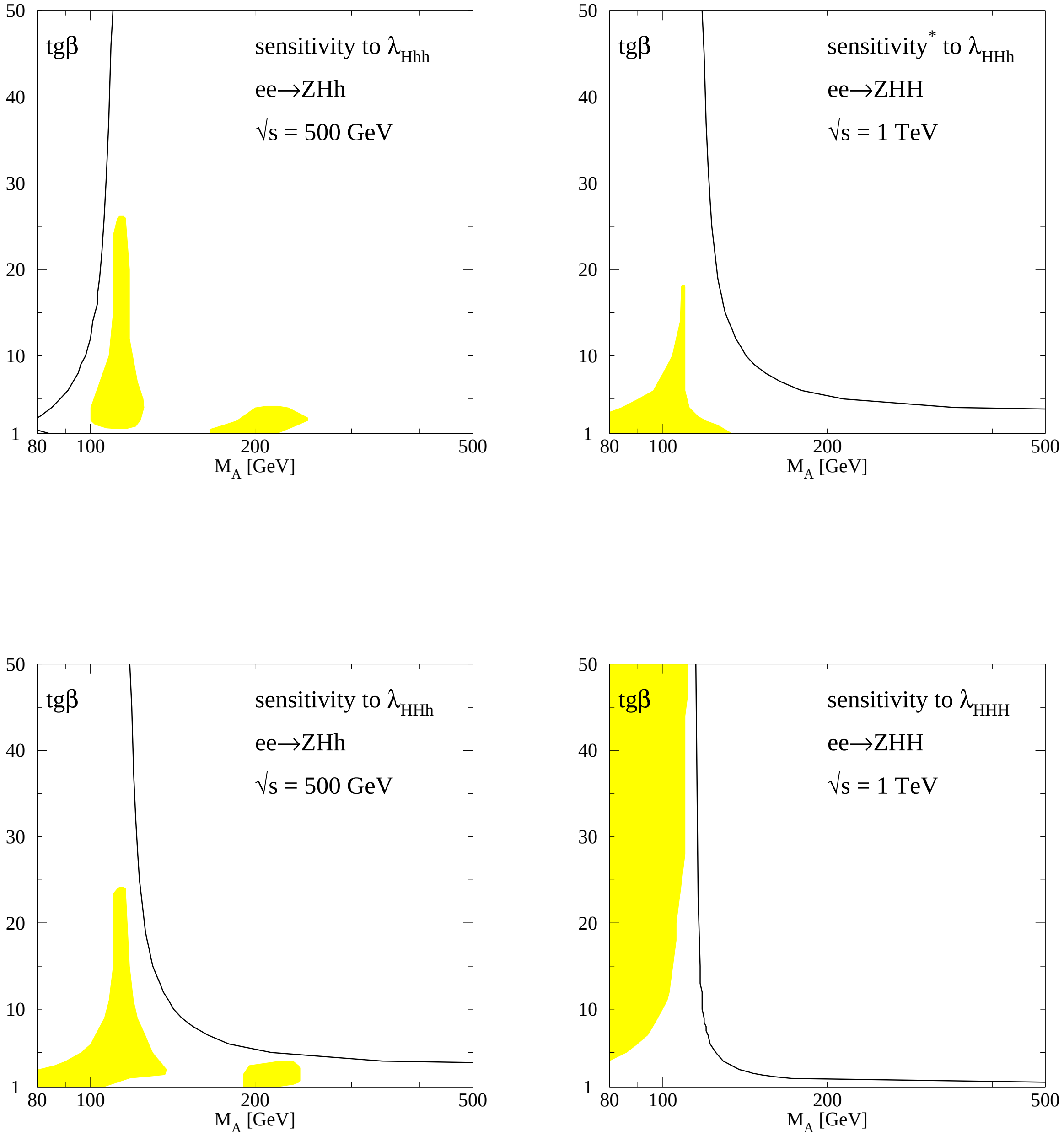

Figure 5.17: *Sensitivity [* eff{$\lambda \to 0$} $>$ 1st.dev.] to the couplings $\lambda_{Hhh}$, $\lambda_{HHh}$ and $\lambda_{HHH}$ in the processes $e^+e^- \to ZHh$ and $e^+e^- \to ZHH$ for collider energies 500 GeV and 1 TeV, respectively (no mixing).*

$\lambda\sin(\beta-\alpha)$ and $\lambda\cos(\beta-\alpha)$ involved in the various channels. The couplings are shown separately in Figs. 5.2 and 5.3. For large values of $M_A$ the areas are limited by phase space effects and due to the suppression of the $H$ and $A$ propagators for large masses. The figures show that the coupling $\lambda_{hhh}$ is accessible in most of the parameter space whereas the parameter range for the other couplings is much smaller.

The sensitivity areas have been constructed without taking into account any experimental efficiencies and background effects so that the given results must be regarded as best case. Considering experimental boundary conditions the areas will shrink. This effect may be reduced, however, if sophisticated cuts on signal and background are applied.

## 5.2 Higgs pair production at the LHC

Higgs pair production at the LHC follows the same pattern as at the linear collider with the exception that gluon-gluon fusion provides an additional channel. The partonic cross sections can be derived from the corresponding $e^+e^-$ processes by replacing the couplings appropriately. The cross sections at hadron level are obtained from the partonic results $\hat{\sigma}(qq' \to HH; \hat{s} = \tau s)$ of the quark subprocess by folding with the appropriate luminosities $d\mathcal{L}^{qq'}/d\tau$:

$$\sigma(pp \to HH) = \int_{4M_H^2/s}^{1} d\tau \frac{d\mathcal{L}^{qq'}}{d\tau} \hat{\sigma}(qq' \to HH; \hat{s} = \tau s) \tag{5.26}$$

where

$$\frac{d\mathcal{L}^{qq'}}{d\tau} = \int_{\tau}^{1} \frac{dx}{x} q(x; Q^2) q'(\tau/x; Q^2) \tag{5.27}$$

with $q$ and $q'$ denoting the quark densities in the proton [108], taken at a typical factorization scale $Q \sim M_H$.

Being of up to $\mathcal{O}(10\text{ fb})$ in the SM case the results for the double Higgs production cross sections at the LHC are larger than in $e^+e^-$ collisions. Yet, the signal processes are plagued by an overwhelming QCD background

### 5.2.1 SM double Higgs production

The processes for the production of a pair of Higgs bosons in the final state at the LHC are given by double Higgs-strahlung off $W$ and $Z$ bosons [86], $WW$ and $ZZ$ fusion [90–94] and gluon-gluon fusion [61],[94–96], in generic notation:

double Higgs-strahlung : $q\bar{q} \to W^*/Z^* \to W/Z + HH$
$WW/ZZ$ double-Higgs fusion : $qq \to qq + WW/ZZ \to HH$
gluon fusion : $gg \to HH$

Fig. 5.18 shows generic diagrams contributing to these processes. Since high energetic protons contain a large number of gluons, gluon-gluon fusion [61], [94–96], provides an important mechanism for Higgs pair production at the LHC. The fusion proceeds via heavy top-quark triangle and box diagrams, cf. Fig. 5.18. As in the case of single Higgs production [109] QCD radiative corrections play an important rôle. In the limit $M_H^2 \ll 4M_t^2$ they yield a $K$ factor double Higgs-strahlung: $q\bar{q} \to ZHH/WHH$

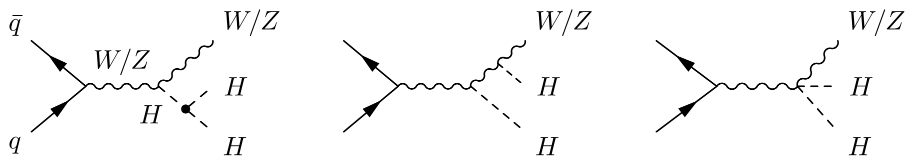

$WW/ZZ$ double-Higgs fusion: $qq \to qqHH$

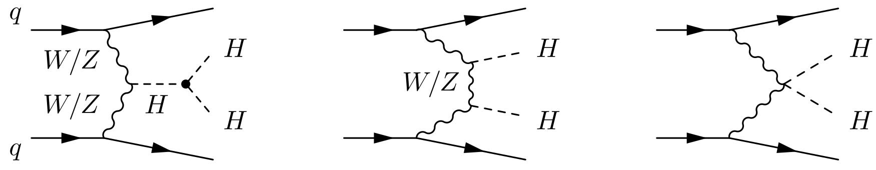

$gg$ double-Higgs fusion: $gg \to HH$

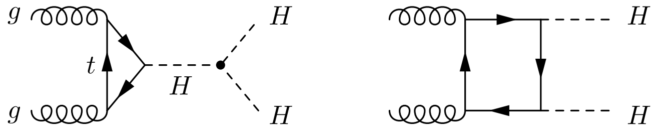

Figure 5.18: *Processes contributing to Higgs-pair production in the Standard Model at the LHC: double Higgs-strahlung, $WW/ZZ$ fusion, and $gg$ fusion (generic diagrams).*

of about 1.9 [61]. For Higgs masses beyond the top-quark threshold a similar $K$ factor is expected.

Fig. 5.19 shows the results of the Higgs pair production mechanisms as a function of the Higgs mass in the intermediate mass range. The dominating process is gluon-gluon fusion followed by $WW + ZZ$ fusion being about one order of magnitude smaller. The ratio of $WW$ to $ZZ$ fusion is $\sim 2.3$. For $M_H \lesssim 140$ GeV, $WW/ZZ$ fusion yields two $b\bar{b}$ pairs resulting from the $H$ decay in the final state. For $M_H \gtrsim 140$ GeV the final state is characterized by $WW^{(*)}WW^{(*)}$. The additional light quark jets due to the fragmentation $q \to W/Z + q$ with a transverse momentum of $p_T \sim \frac{1}{2}M_{W/Z}$ may be exploited to tag the fusion process. The double Higgs-strahlung process $WHH + ZHH$ provides the smallest cross section due to the scaling behaviour, *i.e.* $\hat{\sigma} \sim 1/\hat{s}$. Because of the smaller $q\bar{q}Z$ coupling $WHH$ dominates over $ZHH$ by a factor of about 1.6. The arrows indicate the sensitivity of the double Higgs production processes to a variation of the trilinear Higgs self-coupling in the range $[\frac{1}{2}\lambda_{HHH}, \frac{3}{2}\lambda_{HHH}]$. The size of the cross sections does not exceed $\mathcal{O}(10 \text{ fb})$. High luminosities are therefore needed to enable the extraction of the signal from the large QCD background.

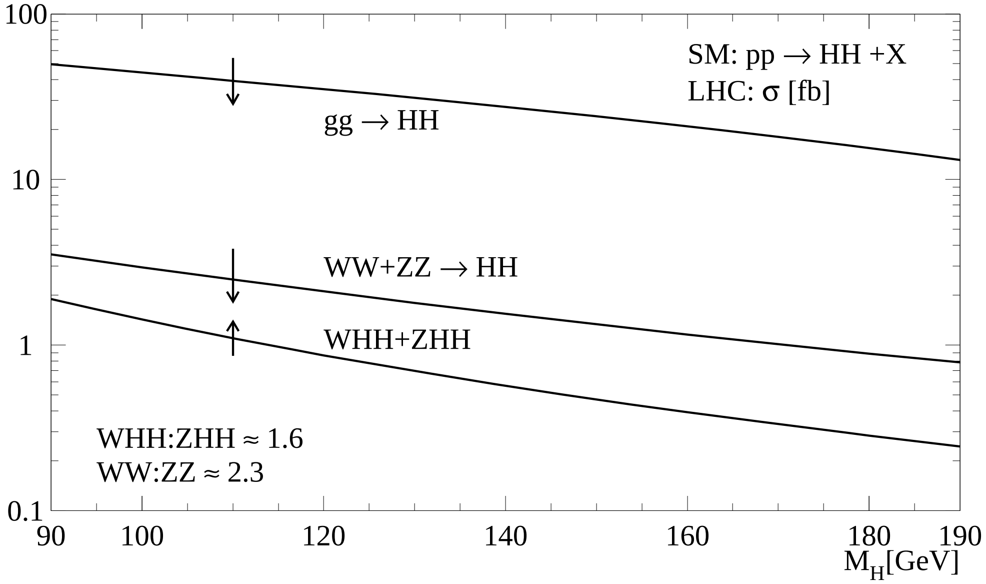

Figure 5.19: *The cross sections for gluon fusion, $WW/ZZ$ fusion and double Higgs-strahlung $WHH$, $ZHH$ in the SM. The vertical arrows correspond to a variation of the trilinear Higgs coupling from* $1/2$ *to* $3/2$ *of the SM value.*

### 5.2.2 Higgs pairs in the MSSM

There are many processes at the LHC which involve the trilinear MSSM Higgs self-couplings [61, 83, 96, 97]:

| | | | | |
|---|---|---|---|---|
| double Higgs-strahlung | : | $q\bar{q} \to W/Z + H_iH_j$ | and | $W/Z + AA \quad [H_{i,j} = h, H]$ |
| triple Higgs production | : | $q\bar{q} \to AH_iH_j$ | and | $AAA$ |
| $WW/ZZ$ double-Higgs fusion | : | $qq \to qq + H_iH_j$ | and | $qq + AA$ |
| $gg$ fusion | : | $gg \to H_iH_j, \quad H_iA$ | and | $AA$ |

As in the SM case also gluon-gluon fusion plays a rôle in contrast to the linear collider. Since in the major part of the parameter space $H$ and $A$ are quite heavy the main focus of the subsequent analysis will be on the production of a light Higgs boson pair. The diagrams contributing to the individual production processes are shown in Fig. 5.20. Some results will also be presented for heavy Higgs boson final states. The cross sections are small unless they include resonant decays. For example in the case of $WHh/ZHh$ they proceed via

$$\begin{aligned} q\bar{q} &\to Z^* \to AH \to ZHh \qquad (5.28)\\ q\bar{q} &\to W^* \to H^\pm H \to WHh \end{aligned}$$

The corresponding diagrams are shown in Fig. 5.21. These resonant heavy Higgs boson decays can largely enhance the cross sections. Since they only involve gauge interactions they are useless for the measurement of the Higgs self-couplings, however.

The results for the $hh$ production processes, *i.e.*

$$\begin{aligned} pp &\to gg \to hh \qquad (5.29)\\ pp &\to Z/W + hh \quad \text{and} \quad A + hh \end{aligned}$$

double Higgs-strahlung: $q\bar{q} \to Zhh/Whh$

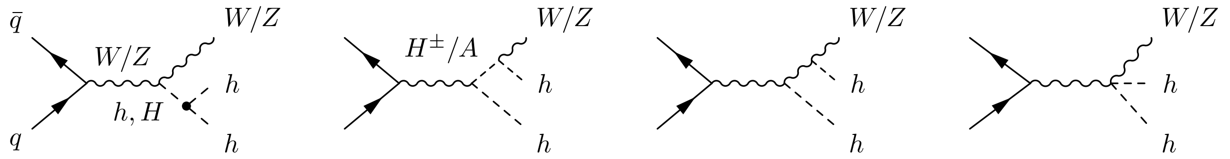

triple Higgs production: $q\bar{q} \to Ahh$

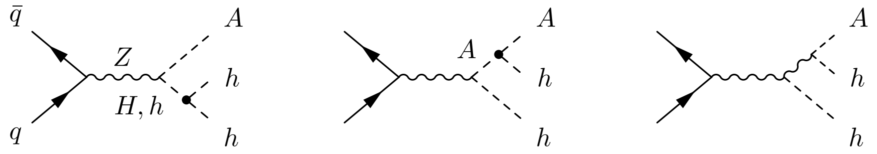

$WW/ZZ$ double-Higgs fusion: $qq \to qqhh$

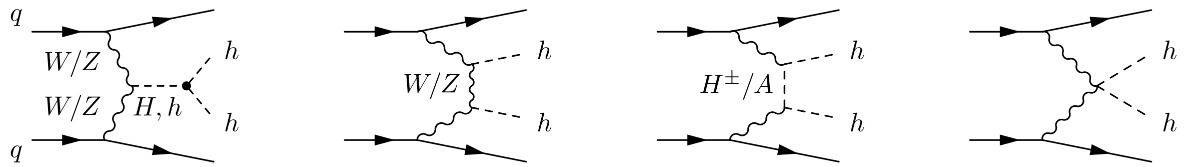

$gg$ double-Higgs fusion: $gg \to hh$

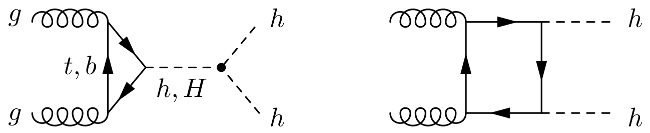

Figure 5.20: *Processes contributing to double and triple Higgs production involving trilinear couplings in the MSSM.*

cascade decay: $q\bar{q} \to AH/HH^{\pm} \to ZHh/WHh$

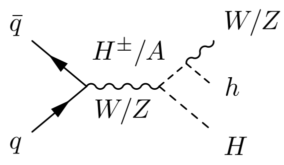

Figure 5.21: *Processes which contribute to double light plus heavy Higgs production in the MSSM but do not involve trilinear couplings.*

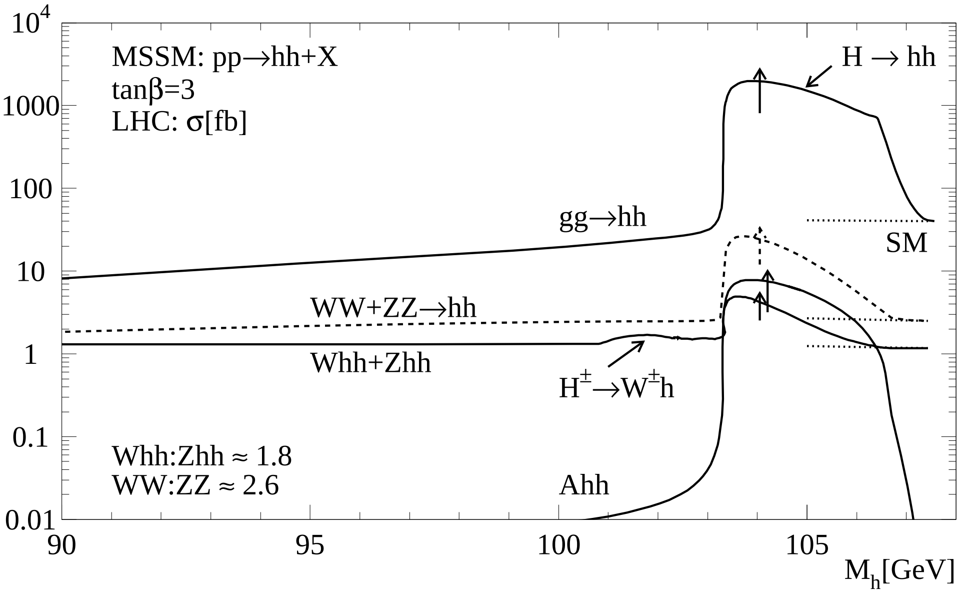

Figure 5.22: *Total cross sections for MSSM hh production via double Higgs-strahlung* $Whh$ *and* $Zhh$*,* $WW/ZZ$ *fusion and gluon fusion at the LHC for* $\tan\beta = 3$*, including mixing effects (*$A = 1$ *TeV,* $\mu = -1$ *TeV).*

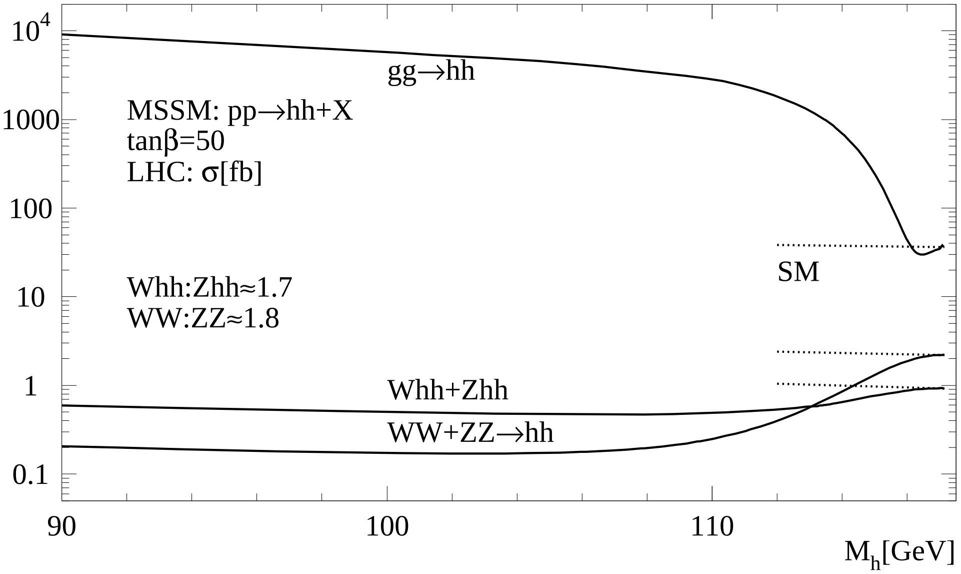

Figure 5.23: *Total cross sections for MSSM hh production via double Higgs-strahlung* $Whh$*,* $Zhh$*,* $WW/ZZ$ *fusion and gluon fusion at the LHC for* $\tan\beta = 50$*, including mixing effects (*$A = 1$ *TeV,* $\mu = 1$ *TeV).*

| $\sigma$ [fb] | $Whh$ | $WHh$ | $WHH$ | $\sum_{i,j} WH_iH_j$ | $WHH_{SM}$ |
|---|---|---|---|---|---|
| $M_A = 100$ GeV<br>$M_h = 98.53$ GeV | 0.332 | 0.017 | 0.540 | 0.889 | 0.908 |
| $\sigma$ [fb] | $Zhh$ | $ZHh$ | $ZHH$ | $\sum_{i,j} ZH_iH_j$ | $ZHH_{SM}$ |
| $M_A = 112$ GeV<br>$M_h = 109.61$ GeV | 0.175 | 0.036 | 0.287 | 0.498 | 0.431 |

Table 5.4: *Total cross sections for $W/Z + H_iH_j$ compared to the corresponding SM cross section. The mixing parameters are chosen $A = \mu = 1$ TeV and* $\tan\beta = 50$.

are demonstrated in Fig. 5.22. For moderate values of $\tan\beta$ the order of the cross sections is the same as in the SM. Yet, the cross sections rise enormously if cascade decays proceeding via intermediate resonant heavy Higgs bosons [44]

$$H \to hh, \quad A \to Zh \quad \text{and} \quad H^\pm \to W^\pm h \tag{5.30}$$

are kinematically possible. The resonant $H$ decay increases the cross sections by up to 2 orders of magnitude giving rise to about a million events in gluon-gluon fusion. This channel therefore allows for the light MSSM Higgs boson search at the LHC [9, 101, 110, 111]. The resonant decay regions are indicated by arrows in Fig. 5.22. In the case of $Whh$ also the resonant decay $H^\pm \to W^\pm h$ leads to an enhancement of the cross section. The vertical arrows illustrate the sensitivity to a variation of $\lambda_{Hhh}$ in the range $[\frac{1}{2}\lambda_{Hhh}, \frac{3}{2}\lambda_{Hhh}]$. In the continuum region the same variation of $\lambda_{hhh}$ induces a 10% modification of the cross sections.

For large values of $\tan\beta$ cascade decays do not play any rôle since they are kinematically forbidden until the decoupling region has been reached where they are not sizeable any more, see Fig. 5.23. The gluon fusion cross section is nevertheless very large due to the enhancement of the $hbb$ Yukawa coupling $\sim m_b \tan\beta$ growing with $\tan\beta$. Since this coupling enters quadratically in the box diagram and only linearly in the triangle loop connecting the gluons to the Higgs boson the sensitivity to the trilinear Higgs self-coupling is small. Yet, the huge cross section leading to the multi-$b$ final states $pp \to hh \to (b\bar{b})(b\bar{b})$ with two resonance structures and large transverse momenta allows for the $h$ Higgs boson search in the large $\tan\beta$ region at the LHC. The $WW/ZZ$ fusion and Higgs-strahlung cross sections are suppressed in the continuum compared to their SM counterparts until the decoupling limit is reached. The heavy Higgs boson is fairly light in this parameter region so that the cross sections with $hh$, $Hh$ and $HH$ final states approximately add up to the SM cross section as can be inferred from Table 5.4 for some representative examples.

Fig. 5.24 shows the cross sections of double Higgs-strahlung involving a heavy and a light CP-even Higgs boson in the final state. In the continuum they are below 0.1 fb. Cascade decays, cf. Fig. 5.21,

$$\begin{aligned} pp &\underset{Z}{\to} AH \to ZHh \\ pp &\underset{W}{\to} H^\pm H \to W^\pm Hh \end{aligned} \tag{5.31}$$

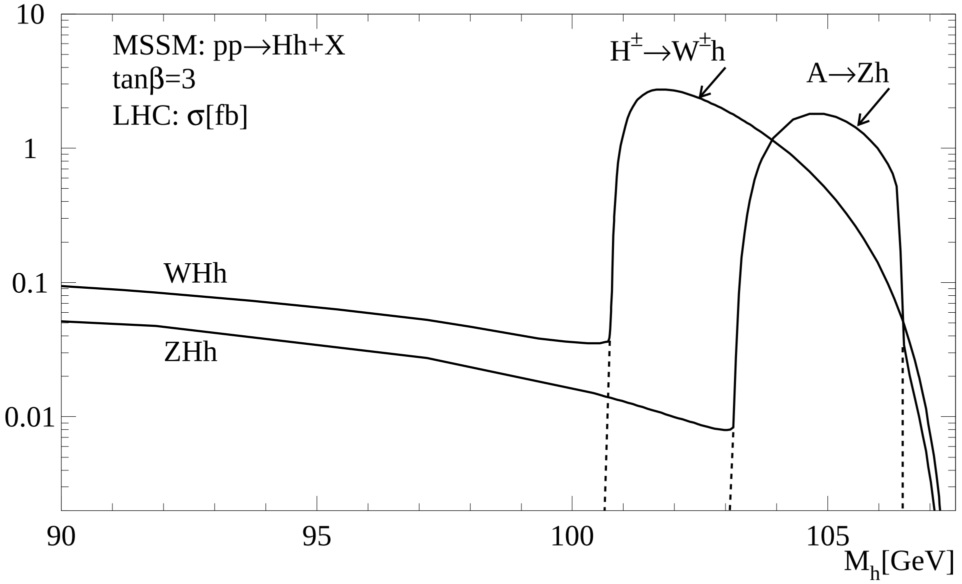

Figure 5.24: *Total cross sections for MSSM Hh production in the processes* $WHh$ *and* $ZHh$ *for* $\tan\beta = 3$*, including mixing effects (*$A = 1$ *TeV,* $\mu = -1$ *TeV).*

give rise to an enhancement by up to 2 orders of magnitude. Mediated by pure gauge interactions they cannot be exploited for the determination of the Higgs self-couplings.

### 5.2.3 Extraction of the signal

In Ref. [100, 101] the extraction of the double Higgs production signal in the channel

$$gg \to hh \to (b\bar{b})(b\bar{b}) \tag{5.32}$$

has been studied both at parton level and in a more realistic detector simulation. As the previous analysis has shown, in the SM case the gluon-gluon fusion cross section is of $\mathcal{O}(10\text{ fb})$ only. Bearing in mind the huge QCD background at the LHC the extraction of the SM signal does not seem to be realistic. In contrast, in the case of the MSSM light Higgs boson $h$ there are regions in the MSSM parameter space where the signal is largely enhanced due to resonant $H$ production with subsequent decay $H \to hh$. Independent of the value of $\tan\beta$, $h$ dominantly decays into a $b\bar{b}$ pair [59, 70, 71] yielding a four $b$ final state in gluon-gluon fusion.

In the parton level analysis of Ref. [100, 101] the potential of extracting the trilinear Higgs coupling $\lambda_{Hhh}$ in the resonant region has been investigated for the parameter set $\tan\beta = 3$, $M_A = 210$ GeV, the mixing parameters $A = -\mu = 1$ TeV and the common squark mass set equal to 1 TeV. Assuming efficient $b$-quark tagging and high purity the main background is due to irreducible QCD modes [110] of $\mathcal{O}(\alpha_s^4)$, EW processes of $\mathcal{O}(\alpha_{em}^4)$ and QCD and EW mixed contributions of $\mathcal{O}(\alpha_s^2\alpha_{em}^2)$. Applying typical LHC detector cuts to the partons and selection cuts appreciating the kinematics of the signal process, the signal and background rates can be reduced to the same level. In a conservative scenario the signal cross section reduces to 102 fb and the background yields 453 fb. Assuming an integrated luminosity of $\int \mathcal{L} = 100\text{ fb}^{-1}$ a sufficiently high signal to background ratio should be achievable. A more realistic analysis based on a detector simulation predicts a signal rate of 38 events per year after all efficiencies and selection cuts have been included [100, 101]. Though a background study on detector level has not been performed yet the results from the parton level analysis predict an encouraging level of background suppression thus demanding for a detailed detector study. Nevertheless, according to the present results the signal seems to be feasible in this parameter region.

For large values of $\tan\beta$ the signal is strongly enhanced due to the large Yukawa coupling $hb\bar{b}$ as has been pointed out previously. Since the box diagram is more favored by this effect than the triangle diagram the sensitivity to the Higgs self-couplings is lost. The large $\tan\beta$ scenario may, however, provide an additional channel for the $h$ detection at moderate $M_A$ values. The detector simulation yields for the signal 1044 events for $M_h = 105$ GeV and $A = \mu = 1$ TeV.

Though the QCD background is very large the determination of the self-coupling $\lambda_{Hhh}$ seems feasible at the LHC in the cascade decay $H \to hh$. In the large $\tan\beta$ regime the extraction of the coupling will be very difficult since no resonance production takes place and the signal sub-process is dominated by the box diagram contributions. In this case, however, the gluon fusion process can be exploited for the light scalar Higgs boson search. The experimental determination of the remaining trilinear Higgs couplings at the LHC will be a difficult task. Since $h$ cannot decay in a pair of pseudoscalar Higgs states and $H \to AA$ is kinematically forbidden in the considered MSSM parameter space, trilinear couplings involving pseudoscalar Higgs bosons have to be extracted from the continuum. The same holds true for $\lambda_{hhh}$, $\lambda_{HHh}$ and $\lambda_{HHH}$ which are not involved in cascade decays. The continuum signal might be swamped by the jetty QCD background if it is not rejected sufficiently well.

# Chapter 6

# Conclusions

This thesis has presented a theoretical analysis of the properties of the SM and MSSM Higgs bosons which can be investigated at the LHC and $e^+e^-$ linear colliders.

The search for Higgs bosons is crucial to prove their existence. Although there are several production mechanisms at the LHC that allow to find the SM or the MSSM Higgs bosons, experimental studies exhibit a region around moderate values of $\tan\beta$ where the heavy MSSM Higgs particles $H$ and $A$ may escape detection. An alternative to the search for $H$ and $A$ at the LHC is provided by Higgs boson production at $\gamma\gamma$ colliders which may be realized by Compton backscattering of laser light from high-energy electron/positron beams. The most promising search channels with large branching ratios are given by the Higgs decays into $b\bar{b}$, $t\bar{t}$, $\tau^+\tau^-$ and chargino or neutralino pairs. They have been investigated by including the polarized NLO results for the signal, background and interference processes and also the resummation of higher orders where necessary. Polarization of the electron/positron and laser beams helps to increase the significances by suppressing the helicity modes of the background processes, that are not compatible with the signal.

For the anticipated luminosities at future $\gamma\gamma$ colliders, the $b\bar{b}$ mode develops sufficiently high significances for the $H$ and $A$ discovery in the whole analysed mass range from 200 to 800 GeV for moderate and large values of $\tan\beta$. The restriction to two-jet topologies in the final state and a cut in the scattering angle of the $b$-quark with respect to the beam axis have been crucial for the reduction of the background. Since the Higgs Yukawa coupling to $\tau^+\tau^-$ increases with $\tan\beta$, also the $\tau^+\tau^-$ channel provides a discovery potential in parts of the $A/H$ mass range for large values of $\tan\beta$. For the $t\bar{t}$ and chargino decay channels the extraction of the signal will be more challenging due to larger backgrounds. The Higgs search in the neutralino channel is confronted with decay products stemming from charginos beyond the corresponding kinematic thresholds. This is due to the final states of the neutralino and chargino cascade decays being rather similar because of the escaping LSP and neutrinos. The different decay topologies may be exploited, however, in order to extract the signal.

Summarizing the results, $\gamma\gamma$ fusion at $e^+e^-$ linear colliders provides a valuable alternative for the heavy Higgs boson search in a variety of decay channels of which the $b\bar{b}$ mode is outstanding.

In addition to the mass, the second basic feature characterizing Higgs particles is their lifetime, or equivalently their total width. Mechanisms that can be exploited at $e^+e^-$ linear colliders for the determination of the small lifetime of a SM Higgs boson in the intermediate mass range have been compared. They use the relation $\Gamma_{tot} = \Gamma_i / BR_{H\to i}$ where $\Gamma_i$ denotes the partial width and $BR_{H\to i}$ the branching ratio of the Higgs decay into the final state $i$. The $\gamma\gamma$ channel allows a model-independent determination of $\Gamma_{tot}$. Alternatively, the lifetime can be measured in the $WW$ channel. Due to possible anomalous $HWW$ couplings involved in the $WW$ fusion process, the analysis is model-dependent. However, the model dependence will be reduced for small momentum transfer at the $HWW$ vertex. The error of the lifetime extracted from the $WW$ mode is smaller than in the $\gamma\gamma$ channel. Taking into account the uncertainties in the various cross sections the total width can be deduced with an accuracy better than 10% for Higgs bosons with $M_H \lesssim 160$ GeV from the $WW$ mode.

A qualitative discussion has demonstrated that the lifetime of a light MSSM Higgs scalar $h$ can be determined from the $b\bar{b}$ channel. The $b\bar{b}$ branching ratio occurs in the Higgs-strahlung process and the Higgs Yukawa coupling to $b$-quarks is accessible in associated production of $h$ with a $b\bar{b}$ pair.

To complete the profile of the Higgs bosons their self-couplings have to be measured. The knowledge of the Higgs self-interactions allows the reconstruction of the Higgs potential and thus the experimental verification of the Higgs mechanism. In this thesis the theoretical framework has been set up for the measurement of the trilinear Higgs couplings. They are accessible in double and triple Higgs production. The processes for SM Higgs bosons in the intermediate mass range and for MSSM Higgs particles turn out to be small at $e^+e^-$ linear colliders. Although at the LHC the cross sections are larger, the signal is confronted with a large QCD background. The extraction of the Higgs self-couplings will therefore be easier in an $e^+e^-$ environment where the background is significantly smaller. For high luminosities, the trilinear self-coupling of an intermediate mass Higgs boson can already be measured in the first step of a linear collider, *i.e.* at c.m. energies of 500 GeV. High $b$-tagging efficiency provided, the experimental accuracy in $\lambda_{HHH}$ will be $\sim 20\%$.

The MSSM with five physical Higgs states includes six trilinear Higgs couplings among the neutral particles and many more quadrilinear self-couplings. The trilinear couplings are involved in a large number of processes at $e^+e^-$ linear colliders and the LHC. In $e^+e^-$ collisions, the coupling among three light Higgs bosons $h$ can be extracted from continuum production. Apart from the decoupling limit, this coupling differs strongly from the corresponding SM value. The remaining couplings among CP-even Higgs bosons will also be accessible, though in a smaller range of the basic input parameters $M_A$ and $\tan\beta$. The trilinear couplings involving pseudoscalar Higgs states are small in the MSSM and the measurement of double and triple Higgs production processes will impose upper bounds on the size of these couplings. At the LHC, the signal is plagued by an enormous QCD background. Resonant decays $H \to hh$ provide a means of extracting the $Hhh$ coupling. The measurement of the other couplings will be more difficult since they have to be extracted from continuum production.

# Appendix A

# Scalar integrals

The integrals that turn up in the calculation of the virtual corrections to the interference cross section in $b\bar{b}$ production in subsection 3.3.1 are listed in this appendix. With $n = 4-2\epsilon$ and the definitions, given in subsection 3.3.1,

$$C_\epsilon = \Gamma(1+\epsilon)\left(\frac{4\pi\mu^2}{m_b^2}\right)^\epsilon \tag{A.1}$$

and

$$t_1 = t - m_b^2 \tag{A.2}$$

the scalar 2-point integrals read

$$B_1(s) = \frac{1}{i\pi^2}\int \frac{d^nq}{(q^2-m_b^2)((q+p)^2-m_b^2)} = C_\epsilon\left[\frac{1}{\epsilon} + 2 + \beta\ln\left(-\frac{1-\beta}{1+\beta}\right)\right] \tag{A.3}$$

with $p^2 = s$ and $\beta = \sqrt{1-\frac{4m_b^2}{s+i\eta}}$ and

$$B_2(t) = \frac{1}{i\pi^2}\int \frac{d^nq}{(q^2-m_b^2)(q+p)^2} = C_\epsilon\left[\frac{1}{\epsilon} + 2 - \frac{t_1}{t}\ln\left(-\frac{t_1}{m_b^2}\right)\right] \tag{A.4}$$

with $p^2 = t$. The $\epsilon$–poles in the two-point integrals are due to UV singularities. The final result depends on two different combinations of the above 2-point integrals:

$$\tilde{B}(s) = B_1(s) - B_2(m_b^2)\,, \qquad \tilde{B}(t) = B_2(t) - B_2(m_b^2) \tag{A.5}$$

$B_2(m_b^2)$ is given by

$$B_2(t=m_b^2) = C_\epsilon\left(\frac{1}{\epsilon}+2\right) \tag{A.6}$$

so that with (A.3) and (A.4)

$$\tilde{B}(t) = -\frac{t_1}{t}\ln\left(-\frac{t_1}{m_b^2}\right) \tag{A.7}$$

and

$$\tilde{B}(s) = \beta\ln\left(-\frac{1-\beta}{1+\beta}\right) \tag{A.8}$$

Scalar 3-point integrals:

$$\begin{aligned}
C_1(s) &= \frac{1}{i\pi^2}\int \frac{d^n q}{(q^2-m_b^2)((q+p_1)^2-m_b^2)(q+p_1+p_2)^2} \\
&= \frac{C_\epsilon}{\beta s}\left\{\frac{1}{\epsilon}\ln\left(-\frac{1-\beta}{1+\beta}\right)\right. \\
&\quad \left. +Li_2\left(\frac{2}{1+\beta}\right)-Li_2\left(\frac{2}{1-\beta}\right)-2\left[Li_2\left(\frac{1}{\beta}\right)-Li_2\left(-\frac{1}{\beta}\right)\right]\right\} \qquad \text{(A.9)}
\end{aligned}$$

with $p_1+p_2+p_3=0$, $p_1^2=s$, $p_2^2=m_b^2$ and $p_3^2=m_b^2$.

$$\begin{aligned}
C_1(t) &= \frac{1}{i\pi^2}\int \frac{d^n q}{(q^2-m_b^2)(q+p_1)^2((q+p_1+p_2)^2-m_b^2)} \\
&= \frac{1}{t-m_b^2}\left\{\frac{\pi^2}{6}-Li_2\left(\frac{t}{m_b^2}\right)\right\} \qquad \text{(A.10)}
\end{aligned}$$

with $p_1+p_2+p_3=0$, $p_1^2=t$, $p_2^2=m_b^2$ and $p_3^2=0$.

$$\begin{aligned}
C(s) &= \frac{1}{i\pi^2}\int \frac{d^n q}{(q^2-m_b^2)((q+p_1)^2-m_b^2)((q+p_1+p_2)^2-m_b^2)} \\
&= \frac{1}{2s}\ln^2\left(-\frac{1-\beta}{1+\beta}\right) \qquad \text{(A.11)}
\end{aligned}$$

with $p_1+p_2+p_3=0$, $p_1^2=0$, $p_2^2=0$ and $p_3^2=s$.

Scalar 4-point integral:

$$\begin{aligned}
& D(s,t) = \frac{1}{i\pi^2} \\
& \int \frac{d^n q}{(q^2-m_b^2)((q+p_1)^2-m_b^2)(q+p_1+p_2)^2-m_b^2)(q-p_4)^2} \\
& = \frac{2C_\epsilon}{\beta s(m_b^2-t)}\left\{Li_2\left(\frac{1}{\beta}\right)-Li_2\left(-\frac{1}{\beta}\right)\right. \\
& \left. +\ln\left(-\frac{1-\beta}{1+\beta}\right)\left[\ln\left(1-\frac{t}{m_b^2}\right)-\frac{1}{2}\frac{1}{\epsilon}\right]\right\} \qquad \text{(A.12)}
\end{aligned}$$

with $p_1^2=0$, $p_2^2=0$, $p_3^2=m_b^2$ and $p_4^2=m_b^2$. The $\epsilon$–poles in $C_1(s)$ and $D(s,t)$ are IR singularities due to the massless gluon exchange. The integrals $C_1(u)$ and $\tilde{B}(u)$ are given by $C_1(t)$ and $\tilde{B}(t)$ after replacing $t$ with $u$.

# Appendix B

# Double Higgs-strahlung processes

In this appendix the cross sections for the pair production of the heavy MSSM Higgs bosons in the Higgs-strahlung processes, $e^+e^- \to ZH_iH_j$ and $ZAA$ with $H_{i,j} = h, H$, are depicted. The process $e^+e^- \to ZH_iA$ involves only gauge couplings at tree level. The notation is the same as in subsection 5.1.1 and the trilinear couplings have been given in section 2.2. Modifications of the MSSM Higgs-gauge couplings with respect to the SM are determined by the mixing parameters:

$$\begin{array}{lll} VVh\text{: } d_1 = \sin(\beta-\alpha) & VVH\text{: } d_2 = \cos(\beta-\alpha) & VVA\text{ : } d_3 = 0 \\ VAh\text{: } c_1 = \cos(\beta-\alpha) & VAH\text{: } c_2 = -\sin(\beta-\alpha) & WAH\text{: } c_3 = 1 \end{array} \tag{B.1}$$

for $V = Z$ and $W$. Except for $WAH$, the Higgs bosons are neutral.

## B.1 $e^+e^- \to ZH_iH_j$

The double differential cross section of the process $e^+e^- \to ZH_iH_j$ for unpolarized beams can be cast into the form

$$\frac{d\sigma[e^+e^- \to ZH_iH_j]}{dx_1 dx_2} = \frac{\sqrt{2}\, G_F^3\, M_Z^6}{384\,\pi^3 s}\, \frac{v_e^2 + a_e^2}{(1-\mu_Z)^2}\, \mathcal{Z}_{ij} \tag{B.2}$$

Using the variables $y_1, y_2, y_3$ defined in subsection 5.1.1, and the scaled masses $\mu_i = M_{H_i}^2/s$, $\mu_{ij} = \mu_i - \mu_j$, etc., the coefficient $\mathcal{Z}_{ij}$ in the cross sections can be expressed as

$$\begin{aligned} \mathcal{Z}_{ij} = {} & \mathfrak{a}_{ij}^2 f_0 + \frac{\mathfrak{a}_{ij}}{2}\left[\frac{d_i d_j\, f_3}{y_1+\mu_{iZ}} + \frac{c_i c_j\, f_3}{y_1+\mu_{iA}}\right] + \frac{(d_i d_j)^2}{4\mu_Z(y_1+\mu_{iZ})}\left[\frac{f_1}{y_1+\mu_{iZ}} + \frac{f_2}{y_2+\mu_{jZ}}\right] \\ & + \frac{(c_i c_j)^2}{4\mu_Z(y_1+\mu_{iA})}\left[\frac{f_1}{y_1+\mu_{iA}} + \frac{f_2}{y_2+\mu_{jA}}\right] + \frac{d_i d_j c_i c_j}{2\mu_Z(y_1+\mu_{iA})}\left[\frac{f_1}{y_1+\mu_{iZ}} + \frac{f_2}{y_2+\mu_{jZ}}\right] \\ & + \Big\{(y_1,\mu_i) \leftrightarrow (y_2,\mu_j)\Big\} \end{aligned} \tag{B.3}$$

with

$$\mathfrak{a}_{ij} = \left[\frac{d_1 \lambda_{hH_iH_j}}{y_3-\mu_{1Z}} + \frac{d_2 \lambda_{HH_iH_j}}{y_3-\mu_{2Z}}\right] + \frac{2d_i d_j}{y_1+\mu_{iZ}} + \frac{2d_i d_j}{y_2+\mu_{jZ}} + \frac{\delta_{ij}}{\mu_Z} \tag{B.4}$$

The coefficients $f_0$ to $f_3$ are given by

$$\begin{aligned}
f_0 &= \mu_Z[(y_1+y_2)^2+8\mu_Z]/8 \\
f_1 &= (y_1-1)^2(\mu_Z-y_1)^2-4\mu_i y_1(y_1+y_1\mu_Z-4\mu_Z) \\
&\quad +\mu_Z(\mu_Z-4\mu_i)(1-4\mu_i)-\mu_Z^2+(\mu_i-\mu_j)^2[y_1(y_1-2)+1-4\mu_i] \\
&\quad +(\mu_i-\mu_j)[8\mu_i(-y_1-\mu_Z)+2y_1\mu_Z(y_1-2)+2\mu_Z+2y_1(y_1-1)^2] \\
f_2 &= [\mu_Z(1+\mu_Z-y_1-y_2-8\mu_i)-(1+\mu_Z)y_1y_2](2+2\mu_Z-y_1-y_2) \\
&\quad +y_1y_2[y_1y_2+\mu_Z^2+1+4\mu_i(1+\mu_Z)]+4\mu_i\mu_Z(1+\mu_Z+4\mu_i)+\mu_Z^2 \\
&\quad -2(\mu_i-\mu_j)^3-(\mu_i-\mu_j)^2[y_2(y_1-1)+10\mu_Z+4\mu_j+3y_1-1] \\
&\quad +(\mu_i-\mu_j)[\mu_Z(2(-y_1y_2-y_1-8\mu_j)+6(\mu_Z+1-y_2)) \\
&\quad +y_1((y_2-1)^2-y_1(1+y_2))+y_2(y_2-1)-4\mu_j(y_1-y_2)] \\
f_3 &= y_1(y_1-1)(\mu_Z-y_1)-y_2(y_1+1)(y_1+\mu_Z)+2\mu_Z(\mu_Z+1-4\mu_i) \\
&\quad +2(\mu_i-\mu_j)^2-(\mu_i-\mu_j)[y_2+y_1^2-3y_1+y_1y_2-4\mu_Z]
\end{aligned} \tag{B.5}$$

Resonance contributions are accounted for by replacing the propagator products with $\pi_1(\mu_i)\pi_2(\mu_j) \to Re\ \{\pi_1(\mu_i)\pi_2(\mu_j^*)\}$ where $\mu_i \to \mu_i - i\gamma_i$ and $\gamma_i = M_{H_i}\Gamma_{H_i}/s$. For $i=j=1$, the expressions eqs. (5.11–5.13) for the process $e^+e^- \to Zhh$ are obtained.

## B.2 $e^+e^- \to ZAA$

The differential cross section of the process $e^+e^- \to ZAA$ can be obtained from Eq. (B.2) with $\mathcal{Z}_{ij} = \mathcal{Z}_{33}$:

$$\begin{aligned}
\mathcal{Z}_{33} &= \mathfrak{a}_{33}^2\, f_0 + \frac{\mathfrak{a}_{33}}{2}\left[\frac{c_1^2}{y_1-\mu_{1A}}+\frac{c_2^2}{y_1-\mu_{2A}}\right] f_3 \\
&\quad +\frac{1}{4\mu_Z}\left[\frac{c_1^2}{y_1-\mu_{1A}}+\frac{c_2^2}{y_1-\mu_{2A}}\right]\left[\frac{c_1^2}{y_2-\mu_{1A}}+\frac{c_2^2}{y_2-\mu_{2A}}\right] f_2 \\
&\quad +\frac{1}{4\mu_Z}\left[\frac{c_1^2}{y_1-\mu_{1A}}+\frac{c_2^2}{y_1-\mu_{2A}}\right]^2 f_1 + \Big\{ y_1 \leftrightarrow y_2 \Big\}
\end{aligned} \tag{B.6}$$

where

$$\mathfrak{a}_{33} = \left[\frac{d_1\lambda_{hAA}}{y_3-\mu_{1Z}}+\frac{d_2\lambda_{HAA}}{y_3-\mu_{2Z}}\right]+\frac{1}{\mu_Z} \tag{B.7}$$

The coefficients $f_0$ to $f_3$ are given by (B.5) after replacing $\mu_1$, $\mu_2$ with $\mu_A$.

# Appendix C

# Triple Higgs boson production

In this appendix the cross sections for the triple Higgs boson production of MSSM Higgs bosons, $e^+e^- \to AH_iH_j$ and $e^+e^- \to AAA$ with $H_{i,j} = h, H$, are listed . Due to CP-invariance the process $e^+e^- \to H_iAA$ does not occur at tree level.

## C.1 $e^+e^- \to AH_iH_j$

In the same notation as above, the double differential cross section of the process $e^+e^- \to AH_iH_j$ for unpolarized beams can be written as:

$$\frac{d\sigma}{dx_1 dx_2} = \frac{G_F^3 M_Z^6}{768\sqrt{2}\pi^3 s}\,\frac{v_e^2 + a_e^2}{(1-\mu_Z)^2}\,\mathfrak{A}_{ij} \tag{C.1}$$

with the function $\mathfrak{A}_{ij}$

$$\begin{aligned}
\mathfrak{A}_{ij} \;=\; & \left[\frac{\lambda_{hH_iH_j}c_1}{y_3-\mu_{1A}} + \frac{\lambda_{HH_iH_j}c_2}{y_3-\mu_{2A}}\right]^2 g_0 + \frac{\lambda^2_{H_jAA}c_i^2}{(y_1+\mu_{iA})^2}g_1 + \frac{\lambda^2_{H_iAA}c_j^2}{(y_2+\mu_{jA})^2}g_1' \\
& + \frac{c_j^2 d_i^2}{(y_1+\mu_{iZ})^2}g_2 + \frac{c_i^2 d_j^2}{(y_2+\mu_{jZ})^2}g_2' + \left[\frac{\lambda_{hH_iH_j}c_1}{y_3-\mu_{1A}} + \frac{\lambda_{HH_iH_j}c_2}{y_3-\mu_{2A}}\right] \\
& \times \left[\frac{\lambda_{H_jAA}c_i}{y_1+\mu_{iA}}g_3 + \frac{\lambda_{H_iAA}c_j}{y_2+\mu_{jA}}g_3' + \frac{c_j d_i}{y_1+\mu_{iZ}}g_4 + \frac{c_i d_j}{y_2+\mu_{jZ}}g_4'\right] \\
& + \frac{\lambda_{H_iAA}\lambda_{H_jAA}c_ic_j}{(y_1+\mu_{iA})(y_2+\mu_{jA})}g_5 + \frac{c_ic_jd_id_j}{(y_1+\mu_{iZ})(y_2+\mu_{jZ})}g_8 \\
& + \frac{\lambda_{H_jAA}c_ic_jd_i}{(y_1+\mu_{iA})(y_1+\mu_{iZ})}g_6 + \frac{\lambda_{H_iAA}c_ic_jd_j}{(y_2+\mu_{jA})(y_2+\mu_{jZ})}g_6' \\
& + \frac{\lambda_{H_jAA}c_i^2d_j}{(y_1+\mu_{iA})(y_2+\mu_{jZ})}g_7 + \frac{\lambda_{H_iAA}c_j^2d_i}{(y_2+\mu_{jA})(y_1+\mu_{iZ})}g_7'
\end{aligned} \tag{C.2}$$

The coefficients $g_k$ read:

$$\begin{aligned}
g_0 &= \mu_Z[(y_1+y_2)^2 - 4\mu_A] \\
g_1 &= \mu_Z(y_1^2 - 2y_1 - 4\mu_i + 1) \\
g_2 &= \mu_Z(2y_1 + y_1^2 - 4y_2 + 4y_2^2 + 4y_1y_2 + 1 + 4\mu_i - 8\mu_j - 8\mu_A) + (\mu_j - \mu_A)^2 \\
&\quad [8 + (-2y_1 + y_1^2 - 4\mu_i + 1)/\mu_Z] + 2(\mu_j - \mu_A)(2y_1y_2 + y_1^2 + 2y_2 - 1)
\end{aligned}$$

$$\begin{aligned}
g_3 &= 2\mu_Z(y_1^2 + y_1 y_2 - y_1 + y_2 + 2\mu_j - 2\mu_i - 2\mu_A) \\
g_4 &= 2\mu_Z(y_1 - y_2 + y_1^2 + 2y_2^2 + 3y_1 y_2 - 2\mu_j + 2\mu_i - 6\mu_A) \\
&\quad +2(\mu_j - \mu_A)(-y_1 + y_2 + y_1^2 + y_1 y_2 + 2\mu_j - 2\mu_A - 2\mu_i) \\
g_5 &= 2\mu_Z(y_1 + y_2 + y_1 y_2 + 2\mu_j + 2\mu_i - 2\mu_A - 1) \\
g_6 &= 2\mu_Z(y_1^2 + 2y_1 y_2 + 2y_2 + 4\mu_j - 4\mu_A - 1) \\
&\quad +2(\mu_j - \mu_A)(y_1^2 - 2y_1 - 4\mu_i + 1) \\
g_7 &= 2[\mu_Z(2y_1^2 + y_1 y_2 + y_2 - 3y_1 + 2\mu_j - 6\mu_i - 2\mu_A + 1) \\
&\quad +(\mu_i - \mu_A)(y_1 + y_2 + y_1 y_2 + 2\mu_j + 2\mu_i - 2\mu_A - 1)] \\
g_8 &= 2\left\{\mu_Z(y_1 + y_2 + 2y_1^2 + 2y_2^2 + 5y_1 y_2 - 1 + 2\mu_j + 2\mu_i - 10\mu_A)\right. \\
&\quad +2(\mu_i - \mu_A)(\mu_i - 3\mu_j - \mu_A - 2y_2 + 1) + 2(\mu_j - \mu_A)(\mu_j - 3\mu_i - \mu_A - 2y_1 + 1) \\
&\quad +[(\mu_j - \mu_A)((1 + y_1)(y_2 + 2y_1 - 1)\mu_Z + 2\mu_i^2 + 4\mu_A^2 + \mu_A - \mu_i) \\
&\quad +(\mu_i - \mu_A)((1 + y_2)(y_1 + 2y_2 - 1)\mu_Z + 2\mu_j^2 + 4\mu_A^2 + \mu_A - \mu_j) \\
&\quad \left. + 6\mu_A(\mu_A^2 - \mu_i\mu_j) + (\mu_i - \mu_A)(\mu_j - \mu_A)(1 + y_1)(1 + y_2)]/\mu_Z\right\}
\end{aligned} \tag{C.3}$$

and

$$g_k'(y_1, y_2, \mu_i, \mu_j) = g_k(y_2, y_1, \mu_j, \mu_i) \tag{C.4}$$

# Appendix D

# Heavy Higgs production in $W_LW_L$ fusion

The amplitudes and cross sections for pair production of CP–even Higgs bosons in the longitudinal $W$ approximation $W_LW_L \to H_iH_j$, as well as for $W_LW_L \to AA$ are presented in this appendix. The notation is the same as in section 5.1.2.

## D.1 $W_LW_L \to H_iH_j$

The amplitudes for the process $W_LW_L \to H_iH_j$ are given by:

$$\begin{aligned}
\mathcal{M}_{LL} &= \frac{G_F\hat{s}}{\sqrt{2}}\left\{(1+\beta_W^2)\left[\delta_{ij}+\frac{\lambda_{hH_iH_j}d_1}{(\hat{s}-M_h^2)/M_Z^2}+\frac{\lambda_{HH_iH_j}d_2}{(\hat{s}-M_H^2)/M_Z^2}\right]\right.\\
&\quad+\frac{d_id_j}{\beta_W\lambda_{ij}}\left[\frac{r_W+(\beta_W-\lambda_{ij}\cos\theta)^2}{\cos\theta-x_W}-\frac{r_W+(\beta_W+\lambda_{ij}\cos\theta)^2}{\cos\theta+x_W}\right]\\
&\quad\left.+\frac{c_ic_j}{\beta_W\lambda_{ij}}\left[\frac{r_++(\beta_W-\lambda_{ij}\cos\theta)^2}{\cos\theta-x_+}-\frac{r_++(\beta_W+\lambda_{ij}\cos\theta)^2}{\cos\theta+x_+}\right]\right\}
\end{aligned} \tag{D.1}$$

where $\mu_{i,j}=M_{H_{i,j}}^2/\hat{s}$, $\beta_W=(1-4M_W^2/\hat{s})^{1/2}$ and $\lambda_{ij}$ is the usual two–body phase space function, $\lambda_{ij}^2=(1-\mu_i-\mu_j)^2-4\mu_i\mu_j$. Furthermore,

$$\begin{aligned}
&x_W=(1-\mu_i-\mu_j)/(\beta_W\lambda_{ij}) && r_W=1-\beta_W^4-\beta_W^2(\mu_i-\mu_j)^2\\
&x_+=(1-\mu_i-\mu_j+2M_{H^\pm}^2/\hat{s}-2M_W^2/\hat{s})/(\beta_W\lambda_{ij}) && r_+=-\beta_W^2(\mu_i-\mu_j)^2
\end{aligned} \tag{D.2}$$

After integrating over the scattering angle, the total cross section of the subprocess can be cast into the form

$$\begin{aligned}
\sigma_{LL}(H_iH_j) &= \frac{1}{1+\delta_{ij}}\frac{G_F^2M_W^4}{2\pi\hat{s}}\frac{\lambda_{ij}}{\beta_W(1-\beta_W^2)^2}\\
&\quad\left\{(1+\beta_W^2)^2\left[\delta_{ij}+\frac{\lambda_{hH_iH_j}d_1}{(\hat{s}-M_h^2)/M_Z^2}+\frac{\lambda_{HH_iH_j}d_2}{(\hat{s}-M_H^2)/M_Z^2}\right]^2\right.\\
&\quad+\frac{2(1+\beta_W^2)}{\beta_W\lambda_{ij}}\left[\delta_{ij}+\frac{\lambda_{hH_iH_j}d_1}{(\hat{s}-M_h^2)/M_Z^2}+\frac{\lambda_{HH_iH_j}d_2}{(\hat{s}-M_H^2)/M_Z^2}\right]\left[d_id_ja_1^W+c_ic_ja_1^+\right]\\
&\quad\left.+\left(\frac{d_id_j}{\beta_W\lambda_{ij}}\right)^2a_2^W+\left(\frac{c_ic_j}{\beta_W\lambda_{ij}}\right)^2a_2^++4\left(\frac{d_id_jc_ic_j}{\beta_W^2\lambda_{ij}^2}\right)\left[a_3^W+a_3^+\right]\right\}
\end{aligned} \tag{D.3}$$

with

$$
\begin{aligned}
a_1^W &= [(x_W\lambda_{ij}-\beta_W)^2+r_W]\log\frac{x_W-1}{x_W+1}+2\lambda_{ij}(x_W\lambda_{ij}-2\beta_W)\\
a_2^W &= \left[\frac{1}{x_W}\log\frac{x_W-1}{x_W+1}+\frac{2}{x_W^2-1}\right]\biggl[x_W^2\lambda_{ij}^2(3\lambda_{ij}^2x_W^2+2r_W+14\beta_W^2)\\
&\quad -(\beta_W^2+r_W)^2-4\lambda_{ij}\beta_Wx_W(3\lambda_{ij}^2x_W^2+\beta_W^2+r_W)\biggr]\\
&\quad -\frac{4}{x_W^2-1}\left[\lambda_{ij}^2(\lambda_{ij}^2x_W^2+4\beta_W^2-4\lambda_{ij}x_W\beta_W)-(\beta_W^2+r_W)^2\right]\\
a_3^W &= \frac{1}{x_+^2-x_W^2}\,\log\frac{x_W-1}{x_W+1}\biggl[2\beta_W\lambda_{ij}x_W[(\beta_W^2+x_W^2\lambda_{ij}^2)(x_W+x_+)+x_Wr_W+x_+r_+]\\
&\quad -x_+(r_++r_W+\lambda_{ij}^2x_W^2)(\beta_W^2+\lambda_{ij}^2x_W^2)-\beta_W^2(x_+\beta_W^2+4\lambda_{ij}^2x_W^3+x_+x_W^2\lambda_{ij}^2)\\
&\quad -x_+r_Wr_+\biggr]+\lambda_{ij}^2\left[\lambda_{ij}^2x_+x_W-2\beta_W\lambda_{ij}(x_W+x_+)+4\beta_W^2\right]
\end{aligned}
$$

$$
a_i^+\equiv a_i^W\ (x_W\leftrightarrow x_+\ ,\ r_W\leftrightarrow r_+) \tag{D.4}
$$

## D.2 $W_LW_L\to AA$

Since there are only a few diagrams involved in the process $W_LW_L\to AA$ and since the masses of the final state particles are equal, the amplitude and cross section adopt a much simpler form for pseudoscalar Higgs bosons:

$$
\begin{aligned}
\mathcal{M}_{LL} &= \frac{G_F\hat{s}}{\sqrt{2}}\biggl\{(1+\beta_W^2)\left[1+\frac{\lambda_{hAA}d_1}{(\hat{s}-M_h^2)/M_Z^2}+\frac{\lambda_{HAA}d_2}{(\hat{s}-M_H^2)/M_Z^2}\right]\\
&\quad +\frac{1}{\beta_W\beta_A}\left[\frac{(\beta_W-\beta_A\cos\theta)^2}{\cos\theta-x_A}-\frac{(\beta_W+\beta_A\cos\theta)^2}{\cos\theta+x_A}\right]\biggr\}
\end{aligned} \tag{D.5}
$$

with

$$
\beta_A=(1-4M_A^2/\hat{s})^{1/2}\quad\text{and}\quad x_A=(1-2M_A^2/\hat{s}+2M_{H^\pm}^2/\hat{s}-2M_W^2/\hat{s})/(\beta_W\beta_A) \tag{D.6}
$$

The total cross section for the subprocess $W_LW_L\to AA$ may be written as

$$
\begin{aligned}
\sigma_{LL}(AA) &= \frac{G_F^2M_W^4}{4\pi\hat{s}}\frac{\beta_A}{\beta_W(1-\beta_W^2)^2}\biggl\{(1+\beta_W^2)^2\left[1+\frac{\lambda_{hAA}d_1}{(\hat{s}-M_h^2)/M_Z^2}+\frac{\lambda_{HAA}d_2}{(\hat{s}-M_H^2)/M_Z^2}\right]^2\\
&\quad +2(1+\beta_W^2)\left[1+\frac{\lambda_{hAA}d_1}{(\hat{s}-M_h^2)/M_Z^2}\ +\ \frac{\lambda_{HAA}d_2}{(\hat{s}-M_H^2)/M_Z^2}\ \right]\\
&\quad \times\frac{1}{\beta_W\beta_A}\biggl[(x_A\beta_A-\beta_W)^2\log\frac{x_A-1}{x_A+1}+2\beta_A(x_A\beta_A-2\beta_W)\biggr]+\frac{1}{\beta_A^2\beta_W^2}\times\\
&\quad \biggl(\log\frac{x_A-1}{x_A+1}\left[3\beta_A^2x_A(\beta_Ax_A-2\beta_W)^2+\beta_W^2(2\beta_A^2x_A-4\beta_W\beta_A-\beta_W^2/x_A)\right]\\
&\quad +\frac{2}{x_A^2-1}\left[(3x_A^2\beta_A^2-2\beta_A^2+\beta_W^2)(\beta_Ax_A-2\beta_W)^2+\beta_W^2(\beta_A^2x_A^2-3\beta_W^2)\right]\biggr)\biggr\}
\end{aligned} \tag{D.7}
$$

## D.3 Asymptotic energies

In the high-energy limit the leading part of the $WW$ fusion cross sections does not depend on the trilinear couplings $H_iH_jH_k$ or $H_iH_jA$. After convolution with the $W$ luminosities, however, the dominant contribution to the leptonic cross sections $e^+e^- \longrightarrow \bar{\nu}_e\nu_eH_iH_j$ and $AA$ stems from the threshold regions, independent of the $e^+e^-$ energies. These processes are therefore also in the high-energy limit in leading order sensitive to the trilinear couplings.

# Bibliography

[1] J. Goldstone, A. Salam and S. Weinberg, Phys. Rev. **127** (1962) 965; S. Weinberg, Phys. Rev. Lett. **19** (1967) 1264; S.L. Glashow, S. Weinberg, Phys. Rev. Lett. **20** (1968) 224; A. Salam, *Proceedings Of The Nobel Symposium*, Stockholm 1968, ed. N. Svartholm

[2] P.W. Higgs, Phys. Lett. **12** (1964) 132; and Phys. Rev. **145** (1966) 1156; F. Englert and R. Brout, Phys. Rev. Lett. **13** (1964) 321; G.S. Guralnik, C.R. Hagen and T.W. Kibble, Phys. Rev. Lett. **13** (1964) 585.

[3] For a review see: J.F. Gunion, H.E. Haber, G. Kane and S. Dawson, *The Higgs Hunter's Guide*, Addison-Wesley, 1990.

[4] M. Spira and P.M. Zerwas, *Int. Universitätswochen*, Schladming 1997, hep-ph/9803257; C. Quigg, Acta Phys. Polon. **B30** (1999) 2145-2192.

[5] D.V. Volkov and V.P. Alkulov, Phys. Lett. **B46** (1973) 109; J. Wess and B. Zumino, Nucl. Phys. **B70** (1974) 39; H.P. Nilles, Phys. Rep. **110** (1984) 1; H.E. Haber, G.L. Kane, Phys. Rep. **117** (1985) 75; M.F. Sohnius, Phys. Rep. **128** (1985) 39.

[6] J.F. Gunion and H.E. Haber, Nucl. Phys. **B272** (1986) 1 and **B278** (1986) 449.

[7] H. Georgi and S.L. Glashow, Phys. Rev. Lett. **32** (1974) 438; H. Georgi, H.R. Quinn and S. Weinberg, Phys. Rev. Lett. **33** (1974) 451; more recent reviews are, for example, G.G. Ross, *Grand Unified Theories*, Benjamin, New York, 1984; R. Mohapatra, Prog. Part. Nucl. Phys. **26** (1991) 1.

[8] J. Ellis, S. Kelley and D.V. Nanopoulos, Phys. Lett. **B260** (1991) 306; U. Amaldi, W. de Boer and H. Fürstenau, Phys. Lett. **B260** (1991) 447; P. Langacker and M. Luo, Phys. Rev. **D44** (1991) 817; G.G. Ross and R.G. Roberts, Nucl. Phys. **B377** (1992) 571.

[9] ATLAS Collaboration, Technical Design Report CERN-LHCC 99-14; CMS Collaboration, Technical Proposal, Report CERN-LHCC 94-38.

[10] Conceptual Design Report of a 500 GeV $e^+e^-$ Linear Collider, eds. R. Brinkmann et al., DESY/ECFA 1997-048/182; E. Accomando et al., Phys. Rep. **299** (1998) 1; P.M. Zerwas, based on lectures at the Cargèse 1999 Summer Institute, the Moscow 1999 Workshop on *Quantum Field Theory* and the Lund 1999 Workshop on *Future Electron Positron Colliders*, hep-ph/0003221.

[11] I.F. Ginzburg, G.L. Kotkin, V.G. Serbo and V.I. Telnov, Pizma ZhETF **34** (1981) 514; JETP Lett. **34** (1982) 491.

[12] I.F. Ginzburg, G.L. Kotkin, V.G. Serbo and V.I. Telnov: Nucl. Inst. Methods **205** (1993) 47; I.F. Ginzburg, G.L. Kotkin, S.L. Panfil, V.G. Serbo and V.I. Telnov, Nucl. Inst. Methods **219** (1984) 5.

[13] N. Cabibbo, Phys. Rev. Lett. **10** (1963) 531; M. Kobayashi and T.Maskawa, Prog. Theor. Phys. **49** (1973) 652.

[14] J. Wess and B. Zumino, Nucl. Phys. **B78** (1974) 1; S. Ferrara and B. Zumino, Nucl. Phys. **B79** (1974) 413.

[15] P. Fayet and J. Iliopoulos, Phys. Lett. **B51** (1974) 461.

[16] see for example: L. Alvarez-Gaume, J. Polchinski and M.B. Wise, Nucl. Phys. **B221** (1983) 495.

[17] L. Girardello and M.T. Grisaru, Nucl. Phys. **B194** (1982) 65.

[18] L. Hall, J. Lykken and S. Weinberg, Phys. Rev. **D27** (1973) 2359.

[19] H.E. Haber, to appear in *Perspectives on Higgs Physics II*, ed. G.L. Kane, World Scientific, Singapore 1997, hep-ph/9707213.

[20] H.E. Haber and R. Hempfling, Phys. Rev. Lett. **66** (1991) 1815; Y. Okada, M. Yamaguchi and T. Yanagida, Prog. Theor. Phys. **85** (1991) 1; J. Ellis, G. Ridolfi and F. Zwirner, Phys. Lett. **B257** (1991) 83.

[21] J.R. Espinosa and M. Quiros, Phys. Lett. **B266** (1991) 389; R. Hempfling and A. Hoang, Phys. Lett. **B331** (1994) 99; J.A. Casas, J. Espinosa, M. Quiros and A. Riotto, Nucl. Phys. **B436** (1995) 3; (E) **B439** (1995) 466; M. Carena, J.R. Espinosa, M. Quiros and C.E.M. Wagner, Phys. Lett. **B335** (1995) 209; M. Carena, J. Espinosa, M. Quiros and C.E.M. Wagner, Phys. Lett. **B355** (1995) 209; M. Carena, M. Quiros and C.E.M. Wagner, Nucl. Phys. **B461** (1996) 407; H.E. Haber, R. Hempfling and A.H. Hoang, Z. Phys. **C75** (1997) 539; S. Heinemeyer, W. Hollik and G. Weiglein, Eur. Phys. J. **C9** (1999) 343; R.-J. Zhang, Phys. Lett. **B447** (1999) 89.

[22] V. Barger, M.S. Berger, A.L. Stange and R.J.N. Phillips, Phys. Rev. **D45** (1992) 4128; Z. Kunszt and F. Zwirner, Nucl. Phys. **B385** (1992) 3.

[23] A. Djouadi, H.E. Haber and P.M. Zerwas, Phys. Lett. **B375** (1996) 203 and (E) in press.

[24] A. Hasenfratz, K. Jansen, C. Lang, T. Neuhaus and H. Yoneyama, Phys. Lett. **B199** (1987) 531; J. Kuti, L. Liu and Y. Shen, Phys. Rev. Lett. **61** (1988) 678; M. Lüscher and P. Weisz, Nucl. Phys. **B318** (1989) 705.

[25] M. Chanowitz, M. Furman and I. Hinchliffe, Phys. Lett. **B78** (1978) 285; N. Cabibbo, L. Maiani, G. Parisi and R. Petronzio, Nucl. Phys. **B158** (1979) 295; R.A. Flores and M. Sher, Phys. Rev. **D27** (1983) 1679; M. Lindner, Z. Phys. **C31** (1986) 295; M. Sher, Phys. Rep. **179** (1989) 273; Phys. Lett. **B317** (1993) 159 and addendum **B331** (1994) 448; G. Altarelli and G. Isidori, Phys. Lett. **B337** (1994) 141; J. Casas, J. Espinosa and M. Quiros, Phys. Lett. **B342** (1995) 171.

[26] J. Espinosa and M. Quiros, Phys. Lett. **B353** (1995) 257.

[27] ALEPH, DELPHI, L3 and OPAL Collaborations, *Searches for Higgs bosons: Preliminary combined results using LEP data collected at energies up to 202 GeV*, ALEPH 2000-028 CONF 2000-023, DELPHI 2000-050 CONF 365, L3 note 2525, OPAL Technical Note TN546, March 2000.

[28] For a review see: A. Djouadi, Int. Journal of Mod. Phys. **A10** (1995) 1.

[29] For a review see: M. Spira, Fortschr. Phys. **46** (1998) 3.

[30] R. Kinnunen and D. Denegri, CMS-NOTE-1997/057.

[31] R. Kinnunen, talk given at the ECFA/DESY Workshop on *Physics and Detectors for a Linear Collider*, Obernai 16-19 Oct. 1999.

[32] M. Spira, contributed to *Physics at Run II: Workshop on Supersymmetry/Higgs: Summary Meeting*, Batavia, IL, 19-21 Nov 1998, hep-ph/9810289.

[33] M. Carena, H. Haber et al., Proc. workshop *"Physics at RunII - Supersymmetry/Higgs"*, Fermilab 1998 (to appear).

[34] H. Baer et al., Phys. Rev. **D47** (1993) 1062; S.G. Frederiksen, N.P. Johnson, G.L. Kane and J.H. Reid, preprint SSCL-577-mc, Jul 1992; S.G. Frederiksen, N.P. Johnson, G.L. Kane and J.H. Reid, Phys. Rev. **D50** (1994) 4244.

[35] M. Carena, S. Mrenna, C.E.M. Wagner, Phys. Rev. **D60** (1999) 075010.

[36] J. Ellis, M.K. Gaillard and D.V. Nanopoulos, Nucl. Phys. **B106** (1976) 292; B.W. Lee, C. Quigg and H.B. Thacker, Phys. Rev. **D16** (1977) 1519; B.L. Ioffe and V.A. Khoze, Sov. J. Part. Nucl. **9** (1978) 50.

[37] V. Barger, K. Cheung, A. Djouadi, B.A. Kniehl and P.M. Zerwas, Phys. Rev. **D49** (1994) 79.

[38] D.R.T. Jones and S.T. Petvoc, Phys. Lett. **B84** (1979) 440.

[39] R.N. Cahn and S. Dawson, Phys. Lett. **B136** (1984) 196; (E) ibid. **B138** 1984,464.

[40] G.L. Kane, W.W. Repko and W.B. Rolnik, Phys. Lett. **B148** (1984) 367.

[41] G. Altarelli, B. Mele and F. Pitolli, Nucl. Phys. **B287** (1987) 205; W. Kilian, M. Krämer and P.M. Zerwas, Phys. Lett. **B373** (1996) 135.

[42] E. Boos, M. Sachwitz, H.J. Schreiber and S. Shichanin, Z. Phys. **C61** (1994) 675.

[43] P. Gracia-Abia and W. Lohmann, talk given at the ECFA/DESY Workshop on *Physics and Detectors for a Linear Collider*, Sitges 28 Apr-5 May 1999.

[44] A. Djouadi, J. Kalinowski and P.M. Zerwas, Z. Phys. **C57** (1993) 569.

[45] A. Djouadi, J. Kalinowski, P. Ohmann and P.M. Zerwas, Z. Phys. **C74** (1997) 93.

[46] P. Janot, in Proc. *Physics and Experiments with $e^+e^-$ Linear Colliders*, Waikoloa/Hawaii 1993, eds. F. Harris, S. Olsen, S. Pakvasa and X. Tata, World Scientific 1993.

[47] J.F. Gunion and H.E. Haber, Phys. Rev. **D48** (1993) 5109.

[48] D.L. Borden, V.A. Khoze, J. Ohnemus and W.J. Stirling, Phys. Rev. **D50** (1994) 4499; G. Jikia and A. Tkabladze, Nucl. Inst. Meth. **A355** (1995) 81.

[49] G. Jikia and A. Tkabladze, Phys. Rev. **D54** (1996) 2030.

[50] B. Kamal, Z. Merebashvili and A.P. Contogouris, Phys. Rev. **D51** (1995) 4808 and (E) ibid. **D55** (1997) 3229; G. Jikia and A. Tkabladze, hep-ph/0004068.

[51] V.S. Fadin, V.A. Khoze and A.D. Martin, Phys. Rev. **D56** (1997) 484; M. Melles and W.J. Stirling, Phys. Rev. **D59** (1999) 094009; Eur. Phys. J. **C9** (1999) 101.

[52] M. Melles and W.J. Stirling, Nucl. Phys. **B564** (2000) 325.

[53] V.V. Sudakov, Sov. Phys. JETP **3** (1956) 65.

[54] H. Zheng and D. Wu, Phys. Rev. **D42** (1990) 3760; S. Dawson and R.P. Kauffman, Phys. Rev. **D47** (1993) 1264;

[55] A. Djouadi, M. Spira, J. van der Bij and P.M.Zerwas, Phys. Lett. **B257** (1991) 187.

[56] A. Djouadi, M. Spira and P.M. Zerwas, Phys. Lett. **B311** (1993) 255; K. Melnikov and O. Yakovlev, Phys. Lett. **B312** (1993) 179; M. Inoue, R. Najima, T. Oka and J. Saito, Mod. Phys. Lett. **A9** (1994) 1189; M. Spira, A. Djouadi, D. Graudenz and P.M. Zerwas, Nucl. Phys. **B453** (1995) 17.

[57] A. Djouadi, V Driesen, W. Hollik and J.I. Illana, Eur. Phys. J. **C1** (1998) 149.

[58] E. Braaten and J.P. Leveille, Phys. Rev. **D22** (1980) 715; N. Sakai, Phys. Rev. **D22** (1980) 2220; T. Inami and T. Kubota, Nucl. Phys. **B179** (1981) 171; S.G. Gorishny, A.L. Kataev and S.A. Larin, Sov. J. Nucl. Phys. **40** (1984) 329; M. Drees and K. Hikasa, Phys. Rev. **D41** (1990) 1547; Phys. Lett. **B240** (1990) 455 and (E) **B262** (1991) 497; S.G. Gorishny, A.L. Kataev, S.A. Larin and L.R. Surguladze, Mod. Phys. Lett. **A5** (1990) 2703; Phys. Rev. **D43** (1991) 1633; A.L. Kataev and V.T. Kim, Mod. Phys. Lett. **A9** (1994) 1309; L.R. Surguladze, Phys. Lett. **341** (1994) 61; K.G. Chetyrkin, J.H. Kühn and A. Kwiatkowski, Proc. of the Workshop *QCD at LEP* Aachen, 1994; K.G. Chetyrkin, Phys. Lett. **B390** (1997) 309; K.G. Chetyrkin and A. Kwiatkowski, Nucl. Phys. **B461** (1996) 3; S.A. Larin, T. van Ritbergen and J.A.M. Vermaseren, Phys. Lett. **B362** (1995) 134.

[59] A. Djouadi, M. Spira and P.M. Zerwas, Z. Phys. **C70** (1996) 427.

[60] B.A. Kniehl and M. Spira, Z. Phys. **C69** (1995) 77.

[61] S. Dawson, S. Dittmaier and M. Spira, Phys. Rev. **D58** (1998) 115012.

[62] A. Dabelstein, Nucl. Phys. **B456** (1995) 25; R.A. Jiménez and J. Solà, Phys. Lett. **B389** (1996) 53; J.A. Coarasa, R.A. Jiménez and J. Solà, Phys. Lett. **B389** (1996) 312; H. Eberl, K. Hidaka, S. Kraml, W. Majerotto and Y. Yamada, hep-ph/9912463; M. Carena, D. Garcia, U. Nierste and C.E.M. Wagner, hep-ph/9912516; S. Heinemeyer, W. Hollik and G. Weiglein, hep-ph/0003022.

[63] G. 't Hooft and M. Veltman, Nucl. Phys. **B44** (1972) 189.

[64] G. Passarino and M. Veltman, Nucl. Phys. **B160** (1979) 151.

[65] M Melles, W.J. Stirling and V.A. Khoze, Phys. Rev. **D61** (2000) 054015.

[66] J.H. Kühn, E. Mirkes and J. Steegborn, Z. Phys. **C57** (1993) 615.

[67] A. Djouadi, J. Kalinowski and M. Spira, Comput. Phys. Comm. **108** (1998) 56.

[68] J. Fleischer and F. Jegerlehner, Phys. Rev. **D23** (1981) 2001; D.Yu. Bardin, B.M. Vilenskiĭ and P.Kh. Khristova, Sov. J. Nucl. Phys. **53** (1991) 152; A. Dabelstein and W. Hollik, Z. Phys. **C53** (1992) 507; B.A. Kniehl, Nucl. Phys. **B376** (1992) 3; A. Djouadi, D. Haidt, B.A. Kniehl, B. Mele and P.M. Zerwas, Proc. Workshop on *$e^+e^-$ Collisions at 500 GeV: The Physics Potential*, ed. P.M. Zerwas, Report DESY 92-123A; B.A. Kniehl, Phys. Rep. **240** (1994) 211.

[69] T.G. Rizzo, Phys. Rev. **D22** (1980) 389; W.-Y. Keung and W.J. Marciano, Phys. Rev. **D30** (1984) 248; R.N. Cahn, Rep. Prog. Phys. **52** (1989) 389.

[70] A. Djouadi, J. Kalinowski and P.M. Zerwas, Z. Phys. **C70** (1996) 435.

[71] S. Moretti and W.J. Stirling, Phys. Lett. **B347** (1995) 291 and (E) **B366** (1996) 451.

[72] B. Kileng, Z. Phys. **C63** (1994) 87; S. Dawson, A. Djouadi and M. Spira, Phys. Rev. Lett. **77** (1996) 16.

[73] W. Kilian, M. Mühlleitner, M. Spira and P.M. Zerwas, DESY 99-171, in preparation.

[74] M. Melles, W.J. Stirling and V.A. Khoze, Phys. Rev. **D61** (2000) 054015.

[75] J.-C. Brient, talk given at the ECFA/DESY Workshop on *Physics and Detectors for a Linear Collider*, Oxford 20-23 March 1999; D. Reid, ibid.

[76] G. Borisov and F. Richard, talk given at the ECFA/DESY Workshop on *Physics and Detectors for a Linear Collider*, Orsay April 1998; M. Battaglia, G. Borisov and F. Richard, talk given at the ECFA/DESY Workshop on *Physics and Detectors for a Linear Collider*, Sitges 28 Apr-5 May 1999; G. Borisov and F. Richard, hep-ph/9905413; M. Battaglia, hep-ph/9910271.

[77] H.J. Schreiber, talk given at the ECFA/DESY Workshop on *Physics and Detectors for a Linear Collider*, Sitges 28 Apr-5 May 1999.

[78] K. Desch and N. Meyer, talk given at the ECFA/DESY Workshop on *Physics and Detectors for a Linear Collider*, Obernai 16-19 October 1999.

[79] M. Battaglia, private communication.

[80] A, Djouadi, J. Kalinowski and P.M. Zerwas, Mod. Phys. Lett. **A7** (1992) 1765 and Z. Phys. **C54** (1992) 255.

[81] S. Dawson and L. Reina, Phys. Rev. **D60** (1999) 015003.

[82] S. Dittmaier, M. Krämer, Y. Liao, M. Spira, P.M. Zerwas, Phys. Lett. **B478** (2000) 247.

[83] W. Kilian and P.M. Zerwas, Proceedings, *XXIX Int. Conference on High Energy Physics*, Vancouver 1998, hep-ph/9809486; A. Djouadi, W. Kilian, M. Mühlleitner and P.M. Zerwas, Eur. Phys. J. **C10** (1999) 27; A. Djouadi, W. Kilian, M. Mühlleitner and P.M. Zerwas, Eur. Phys. J. **C10** (1999) 45; A. Djouadi, W. Kilian, M. Mühlleitner and P.M. Zerwas, DESY 99-171, PM/99-55, TTP99-48, hep-ph/0001169.

[84] M.N. Dubinin and A.V. Semenov, SNUTP-98-140, hep-ph/9812246.

[85] G. Gounaris, D. Schildknecht and F. Renard, Phys. Lett. **B83** (1979) 191 and (E) **B89** (1980) 437.

[86] V. Barger, T. Han and R.J.N. Phillips, Phys. Rev. **D38** (1988) 2766.

[87] V.A. Ilyin, A.E. Pukhov, Y. Kurihara, Y. Shimizu and T. Kaneko, Phys. Rev. **D54** (1996) 6717.

[88] F. Boudjema and E. Chopin, Z. Phys. **C73** (1996) 85.

[89] V. Barger and T. Han, Mod. Phys. Lett. **A5** (1990) 667.

[90] D.A. Dicus, K.J. Kallianpur and S.S.D. Willenbrock, Phys. Lett. **B200** (1988) 187; A. Abbasabadi, W.W. Repko, D.A. Dicus and R. Vega, Phys. Rev. **D38** (1988) 2770.

[91] A. Abbasabadi, W.W. Repko, D.A. Dicus and R. Vega, Phys. Lett. **B213** (1988) 386.

[92] K.J. Kallianpur, Phys. Lett. **B215** (1988) 392.

[93] A. Dobrovolskaya and V. Novikov, Z. Phys. **C52** (1991) 427.

[94] O.J.P. Eboli, G.C. Marques, S.F. Novaes and A.A. Natale, Phys. Lett. **B197** (1997) 269.

[95] E.W.N. Glover and J.J. van der Bij, Nucl. Phys. **B309** (1988) 282.

[96] T. Plehn, M. Spira and P.M. Zerwas, Nucl. Phys. **B479** (1996) 46; (E) Nucl. Phys. **B531** (1998) 655.

[97] A. Belyaev, M. Drees, O.J.P Eboli, J.K. Mizukoshi and S.F. Novaes, Phys. Rev. **D60** (1999) 075008; A. Belyaev, M. Drees and J.K. Mizukoshi, preprint SLAC-PUB-8249, September 1999, hep-ph/9909386.

[98] G. Jikia, Nucl. Phys. **B412** (1994) 57.

[99] D.J. Miller and S. Moretti, Eur. Phys. J. **C13** (2000) 459 and hep-ph/0001194.

[100] R. Lafaye, D.J. Miller, M. Mühlleitner and S. Moretti, hep-ph/0002238.

[101] A. Djouadi et al., Workshop on *Physics at TeV Colliders*, Les Houches, France, 7-18 Jun 1999, hep-ph/0002258.

[102] P. Lutz, talk given at the ECFA/DESY Workshop on *Physics and Detectors for a Linear Collider*, Oxford 20-23 March 1999; P. Gay, talk given at the ECFA/DESY Workshop on *Physics and Detectors for a Linear Collider*, Obernai 16-19 October 1999.

[103] See [67] and M. Spira, private communication.

[104] P. Osland and P.N. Pandita, Phys. Rev. **D59** (1999) 055013.

[105] S. Dawson, Nucl. Phys. **B249** (1985) 42.

[106] E.E. Boos, M.N. Dubinin, V.A. Ilyin, A.E. Pukhov and V.I. Savrin, Report SNUTP-94-116, hep-ph/9503280; P.A. Baikov et al., *Proceedings of the Workshop QFTHEP-96*, eds. B. Levtchenko and V. Savrin, Moscow 1996, hep-ph/9701412.

[107] P. Lutz, private communication.

[108] A. Martin, R. Roberts and W. Stirling, Phys. Lett. **B354** (1995) 155.

[109] A. Djouadi, M. Spira and P.M. Zerwas, Phys. Lett. **B264** (1991) 440; S. Dawson, Nucl. Phys. **B359** (1991) 283; D. Graudenz, M. Spira and P.M. Zerwas, Phys. Rev. Lett. **70** (1993) 1372; M. Spira, A. Djouadi, D. Graudenz and P.M. Zerwas, Nucl. Phys. **B453** (1995) 17.

[110] E. Richter-Was and D. Froidevaux, Z. Phys. **C76** (1997) 665; E. Richter-Was et al., Int. J. Mod. Phys. **A13** (1998) 1371.

[111] J. Dai, J.F. Gunion and R. Vega, Phys. Lett. **B371** (1996) 71 and *ibid.* **378** (1996) 801.

# Acknowledgements

I would like to thank my advisor P.M. Zerwas for the suggestion of the project, the continuous support of this work, his enthusiasm and encouragement. I have profited from his experience and numerous helpful discussions.

I am grateful to A. Djouadi, W. Kilian and M. Spira for a pleasant collaboration and their patience in answering my questions. I would like to thank W. Kilian for proof-reading parts of the draft. Special thanks go to M. Spira for the careful proof-reading of the draft and for countless clarifying discussions.

I would like to take the opportunity to thank R. Lafaye, D.J. Miller and S. Moretti for an enjoyable working atmosphere. Furthermore, I am indebted to D.J. Miller for advice in the English language.

During the first stage of my work I profited a lot from T. Plehn's experience.

I would like to thank all my friends at DESY, in particular O. Bär, Y. Schröder, M. Spira, A. Brandenburg, D.J. Miller, U. Nierste, B. Plümper, M. Maniatis and M. Weber, for the pleasant working environment.

O. Bär is due specific thanks for supporting me at all stages of the thesis and fortifying me in the realization of my ideas.

My special thanks go to my parents. To my mother who has always believed in me. To my father who had his special great manner in encouraging me to go my way.

Financial support by Deutsches Elektronen-Synchrotron (DESY) is gratefully acknowledged.